1-1-2013

Dual-Phase Mixed Ion and Electron Conducting Co2-Selective Permeation Membranes

Lingling Zhang
University of South Carolina - Columbia

DUAL-PHASE MIXED ION AND ELECTRON CONDUCTING CO_2-SELECTIVE PERMEATION MEMBRANES

by

Lingling Zhang

Bachelor of Engineering
Huaqiao University, 2005

Master of Engineering
Tongji University, 2009

Submitted in Partial Fulfillment of the Requirements

For the Degree of Doctor of Philosophy in

Mechanical Engineering

College of Engineering and Computing

University of South Carolina

2013

Accepted by:

Kevin Huang, Major Professor

Kenneth Reifsnider, Committee Member

Xinyu Huang, Committee Member

Kyle S. Brinkman, Committee Member

Lacy Ford, Vice Provost and Dean of Graduate Studies

ACKNOWLEDGEMENTS

I would like to thank my advisor, Dr. Kevin Huang who brought me to this field and offered his knowledge, experience and his character to guide my study, research and life. These treasures will go with me for the whole life.

I would also like to convey my sincerest appreciation to my thesis committee, Dr. Kenneth Reifsnider, Dr. Xinyu Huang, and Dr. Kyle S. Brinkman, for their invaluable advice and continuous help during my Ph.D study. My special thanks to my current and former group members, Xue Li, Nansheng Xu, Xuan Zhao, Yunhui Gong, Zhengping Mao, Qunwei Tang, Wei Tao and Kevin Rimoto, for their active and valuable contribution and suggestions to my research.

I finally would like to dedicate this dissertation to my husband Siwei Wang, who helps and understands me. His constant love, support and encouragement helped me get through some of the difficult times. My special thanks to my little daughter Nikki. She brings so many joys in my life. I would also like to thank my parents Xuehua Zhang, hongie Jia and parents' in law Zhigang Wang, Yumei Huang to bring us up and provided their endless support without any expectations.

ABSTRACT

Fossil fuels are the dominant energy source powering our modern society. However, burning fossil fuels emits carbon dioxide (CO_2), a greenhouse gas that can cause climate change and ultimately threaten the survival of humanity. Effectively mitigating CO_2 emissions from the use of fossil fuels has become an intense subject of scientific research as well as political debate in recent years. The current mainstream technical approach to achieving that goal is to curb the emission of CO_2 by capturing CO_2 at point-sources and geologically storing it. The CO_2 separation and capture process, the first step toward the ultimate storage of CO_2, can be applied to various stages of the combustion of fossil fuels: post-combustion, pre-combustion and oxy-combustion Significant technical progress in materials development and engineering design of carbon capture systems has been made over the past decades, but the major challenge to the commercial deployment of these technologies remains to be the energy penalty associated with CO_2 capture, compression and storage (CCS) that considerably lowers the overall plant efficiency and ultimately increases the cost-of-electricity produced.

The state-of-the-art technologies for CO_2-capture are principally based on reversible chemical/physical sorption processes using liquid solvents and solid sorbents as a CO_2 scrubber and on size-exclusion permeation using membranes as a CO_2 molecular filter. However, as aforementioned, the solvents and sorbents based technology is costive, cumbersome and inefficient, and the membrane technology is susceptible to

poor selectivity and incompatibility to high temperatures. As of today, only a few of these technologies are considered commercially viable for large-scale application.

In this research, a new type of electrochemical CO_2 separation membranes that are in theory exclusively permeable and can continuously separate CO_2 from either a pre-combustion or post-combustion industrial stream have been investigated. This category of membranes functions as a mixed conductor, through the surface electrochemical reactions of which CO_2 molecules can be electrochemically transported from the targeted stream to an isolated and concentrated stream that can be readily pressurized, transported and stored. Since these membranes only allow the electrochemically active species to transport through the membrane under a gradient of electrochemical potential, its selectivity is exclusive. Furthermore, this type of membrane normally operates at elevated temperatures in a continuous fashion, presenting excellent compatibility with high-temperature process streams.

There are two types of mixed conductors envisioned for CO_2 separation: 1) mixed carbonate-ion and oxide-ion conductor (MOCC); 2) mixed carbonate-ion and electron conductor (MECC). The former is more suited for pre-combustion CO_2 separation while the latter is more applicable to post-combustion CO_2 separation. These CO_2 separation membranes should also be technically and economically more attractive than conventional electrically driven, molten carbonate fuel cell based CO_2 concentrator since no external electronics are needed.

The objective of this proposed research is to systematically study the chemical and physical properties of both MOCC and MECC membranes for selective electrochemical CO_2 separations. First, a combined "co-precipitation" and "sacrificial

template" technique has been demonstrated to produce a highly efficient porous ceramic matrix containing a vast number of three-dimensional intra- and interconnected pathways as revealed by 3D XCT for fast-ion transport. The performance of thus synthesized MOCC membrane is remarkable, showing a permeation CO_2 flux density from a simulated fuel gas stream two orders of magnitude higher than ceramic-carbonate systems fabricated with other methods. In addition, the CO_2 flux density measured was found to increase with the partial pressure of hydrogen in the feedstock, further verifying the CO_2 transport mechanism understood.

Second, a surface-modified dense silver-MC dual-phase MECC membrane for CO_2 separation from flue gas has been also demonstrated with improved stability. Two pore formers were investigated to make the porous silver matrix: microcrystalline methylcellulose and carbon black. The surface modifier is Al_2O_3, which was prepared by coating Al_2O_3 colloidal onto the exposed surfaces of a porous silver matrix. The results show that the use of 5% Al_2O_3 colloidal gives MECC the best flux density and stability compared to the unmodified sample. Approximately 90% of the original flux values can still be maintained after 130-hour testing for the modified membrane with microcrystalline methylcellulose pore former, whereas only one-third of the original flux values can be retained even after 60 hours for the unmodified membrane. For the surface modified MECC membrane with carbon black pore former, the CO_2 flux was found to increase with time for the first 160 hours by 200%, followed by decreasing for the next 90 hours. At the 250-hour marker, the flux is still 160% of the original value. Overall, silver-molten carbonate MECC with carbon black as a pore former and Al_2O_3 as a surface modifier demonstrates great potential to separate CO_2 from flue gas.

With the stabilized MECC membranes, we also demonstrate that the CO_2 flux follow a linear relationship with reciprocal thickness in a thickness greater than 0.84 mm, suggesting a bulk diffusion controlling mechanism. Below 0.84 mm, the flux remains flat, suggesting that the rate-limiting step has shifted to the surface exchange kinetics of CO_2 and O_2. We also found that the CO_2 flux is proportional to the linear chemical gradient of CO_2 and O_2, implying that the conductivity of CO_3^{2-} is dependent of P_{CO2} and P_{O2} with a unity reaction order.

Establishing CO_2 transport models and developing flux theory for MOCC and MECC membranes is another task of this thesis project. Multifunctional CO_2 transport models encompassing 3PBs and 2PBs pathways are proposed for the first time. The CO_2 flux equations suitable for dual-phase mixed conductors are developed from classical flux theory and verified by experimental results.

Finally, we have discovered for the first time the existence of pyrocarbonate $C_2O_5^{2-}$ species on the surface of a eutectic Li_2CO_3 and Na_2CO_3 melt subject to CO_2 atmosphere through a combined "DFT" and "Raman Spectroscopy" methodology. This discovery lays the foundation for the CO_2 transport models established.

TABLE OF CONTENTS

LIST OF TABLES

LIST OF FIGURES

CHAPTER 1 GENERAL INTRODUCTION: MATERIALS FOR CARBON DIOXIDE SEPARATION FROM FUEL AND FLUE GASES

1.1 INTRODUCTION

Fossil fuels are the dominant energy source powering our modern society, largely due to their competitive cost and wide accessibility. However, burning fossil fuels emits carbon dioxide (CO_2), a greenhouse gas that can cause climate change and ultimately threaten the survival of humanity. An alarming statistic shows that nearly 40% of 5.8 billion metric tons of the total US anthropogenic CO_2 emissions in 2008 was resulted from burning fossil fuels for 71% of the total U. S. electricity generation.[1, 2] From Annual Energy Outlook of 2012 (shown in Fig.1. 1), fossil fuel full consumption is still 78% of total US energy use in 2035. Effectively mitigating CO_2 emissions from the use of fossil fuels has, therefore, become an intense subject of scientific research as well as political debate in recent years.

There are four general strategies currently being considered for the abatement of CO_2 emissions: demand-side conservation, supply-side efficiency improvement, potential increase in nuclear and renewable energy supplies, and implementation of carbon capture and storage (CCS) technology into existing fossil-fueled power plants[3, 4]. Of all the options, CCS is regarded as the sole practical near-term solution to effectively stabilize atmospheric CO_2 concentration[3].

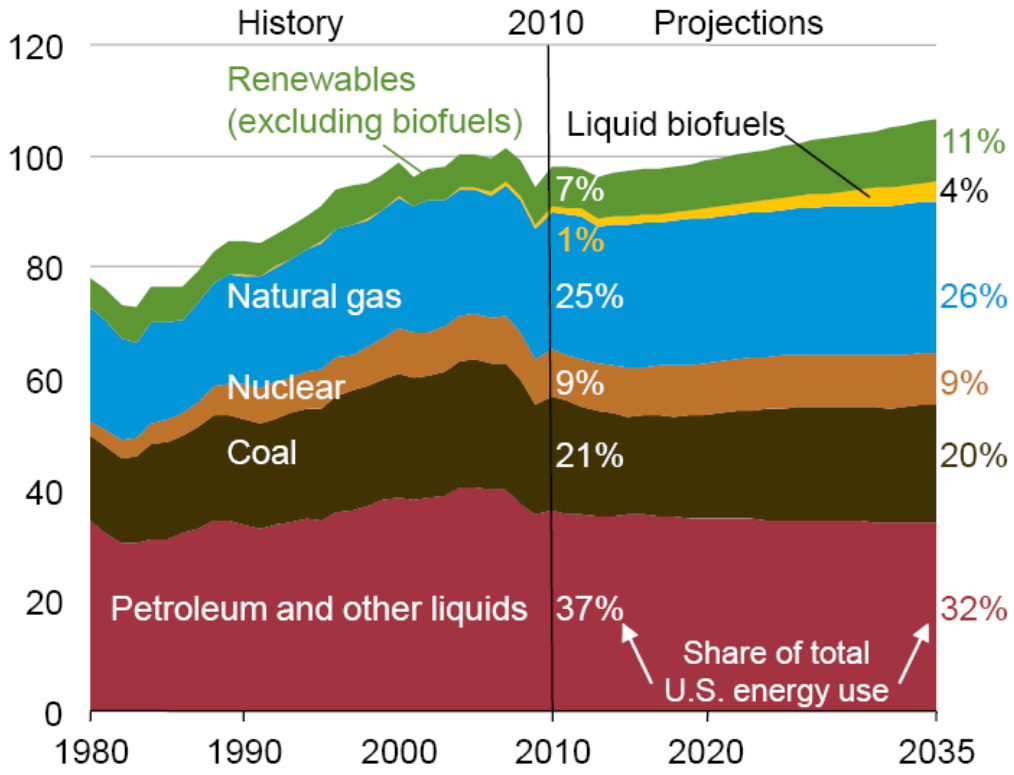

Figure 1.1 Image and date from US Energy Information Agency, Annual Energy Outlook, 2011.[5]

To realize the ultimate CCS, separation and capture of CO_2 from a CO_2-containing industrial process stream is the first step. The CO_2 capture technologies currently being developed and demonstrated for existing fossil-fueled power plants are primarily targeting three different emission sources: post-combustion, oxyfuel combustion and pre-combustion[6-8, 3] (see Fig. 1.2). The pre-combustion CO_2 capture/separation is more suited for integrated gasification combined cycle (IGCC) or natural gas combined cycle (NGCC) power plants where CO_2 is separated from a mixture of CO_2 and H_2 to allow final combustion to take place in pure H_2.[9, 10] The significant advantages of pre-combustion capture are that the higher component concentrations and elevated pressures can reduce the energy penalty of the capture process to 10–16%, roughly half that for post-combustion CO_2 capture.[11] A further advantage is that pre-combustion technology generates a hydrogen-rich fuel, which can be used as a chemical feedstock for fuel cell power generation, and/or for the development of a hydrogen economy.[12] The post-combustion and oxy-combustion CO_2 captures are more applicable to conventional pulverized coal-fired (PC) and natural gas-fired power plants where CO_2 is separated from N_2-concentrated flue gas after fossil fuels are combusted in air[4]. Post-combustion CO_2 separation is realized at relatively low temperature from a gaseous stream at atmospheric pressure and with low CO_2 concentration. SO_2, NO_2 and O_2 may also be present in small amounts. In oxy-combustion process, fossil fuels are combusted

in pure oxygen separated from are, producing a stream of CO_2 and H_2O mixture for easy CO_2 capture. [13]

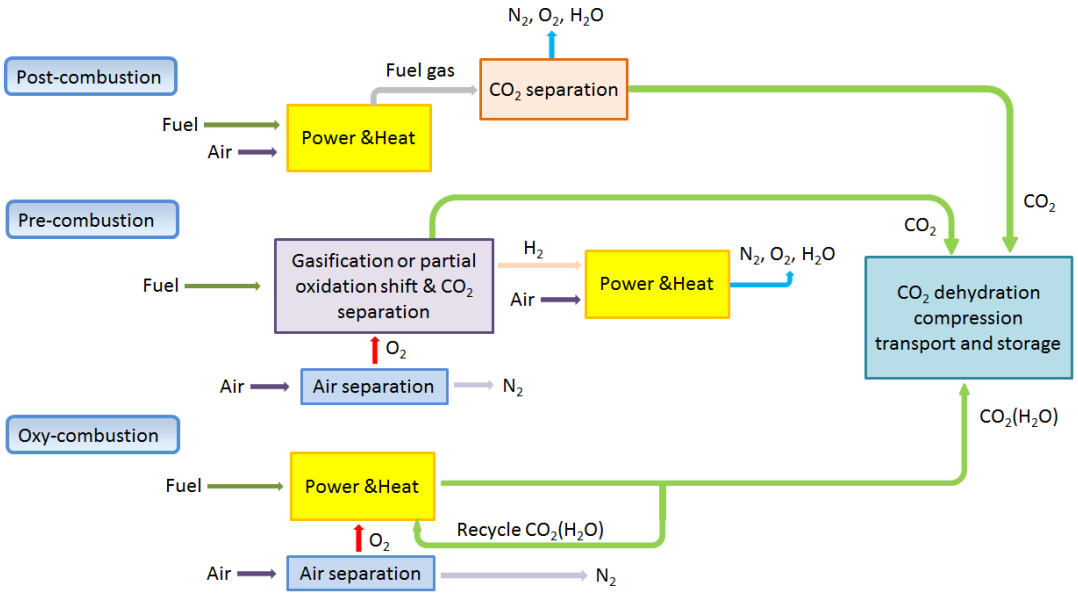

Figure 1.2 Post-combustion, pre-combustion and oxyfuel combustion processes.

1.2 SOLVENT-BASED SYSTEMS

1.2.1 Amine absorption process

The solvent-based absorption processusing amine solutions such as monoethanolamine (MEA) to capture CO_2 is a commercialized technology used in natural gas industry. It is a nonselective solvent to remove acidic gas impurities (such as H_2S, CO_2) from natural gas stream developed over 60 years ago.[14] MEA reacts with CO_2 in the gas stream to form MEA carbonate, which is a water soluble compound. The

aqueous phase chemical reactions involved in the MEA-water-CO_2 system can be expressed by:

$$2H_2O = H_3O^+ + OH^- \quad (1\text{-}1)$$

$$CO_2 + 2H_2O = H_3O^+ + HCO_3^- \quad (1\text{-}2)$$

$$HCO_3^- + H_2O = H_3O^+ + CO_3^{2-} \quad (1\text{-}3)$$

$$MEA^+ + H_2O = H_3O^+ + MEA \quad (1\text{-}4)$$

Because of these reactions, amines are able to capture CO_2 from streams with low CO_2 partial pressure. The CO_2-rich MEA solution is then set to a stripper where it is reheated to release almost pure CO_2. The MEA technology is commercially mature and can be easily retrofitted into existing power plants. But it still suffers some drawbacks: high energy penalty required for solvent regeneration and necessary use of inhibitors to control corrosion and oxidative degradation due to residual oxygen in the flue stream.[9]

Improvements to amine-based systems for CO_2 capture are currently being pursued by a number of process developers. Fluor's Econamine FG Plus is a proprietary acid gas removal system that has demonstrated greater than 95% availability with natural gas fired power plants, specifically on a 350 ton/day CO_2 capture plant in Bellingham, MA. It is currently the state-of-the-art commercial technology baseline used for comparing other CO_2 capture technologies. Mitsubishi Heavy Industries (MHI) has developed a new absorption process, referred to as KS-1. A key factor in this development is the utilization of a new amine-type solvent for the capture of CO_2 from

flue gas.[15] R&D pathways to improved amine-based systems include modified tower packing to reduce pressure drop and increase contacting, increased heat integration to reduce energy requirements, additives to reduce corrosion and allow higher amine concentrations, and improved regeneration procedures.

1.2.2 Ionic liquid

Ionic liquids are organic salts, a class of physical solvents which are known to be selective for CO_2 absorption.[16] They comprise of combinations of large organic cations and smaller inorganic anions and are typically viscous liquids at near room temperature. The CO_2 solubility and selectivity can be tuned by choice of cation, anion and substituents. The advantages for ionic liquids of CO_2 capture is the minimal energy required for solvent regeneration. The capacity is directly proportional to the partial pressure of CO_2 and improves at pressures above 1–2 bar. For this reason, ionic liquids were initially proposed for pre-combustion applications. Due to some ionic liquids react with CO_2 as well as SO_2 in a chemisorption mechanism, the other advantage is that liquids can simultaneously serve to remove CO_2 and SO_2. A second step to separate CO_2 from SO_2 is needed. Take alkylimidazolium-based ionic liquids as an example, CO_2 organizes strongly about the $[PF_6]$ anion in a "tangent-like" configuration that maximizes favorable interactions, but is more diffusely distributed about the imidazolium ring (see Fig. 1.3).[17]

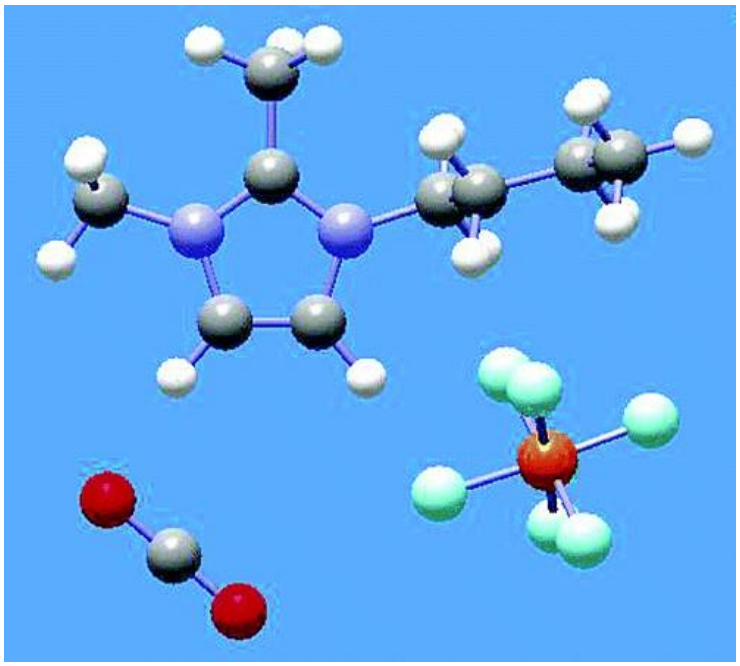

Figure 1.3 The crystal structure of imidazolium ring.[17]

1.2.3 Alkaline Salt (Carbonate-based system)

Alkaline salts such as sodium and potassium salts of carbonate, phosphate, borate arsenite and phenolate have been developed for CO_2 separation. The most common salt used in the industry has been sodium carbonate and potassium carbonate.[18] The sodium carbonate absorbs CO_2 via following chemical reactions:

$$Na_2CO_3(s) + CO_2(g) + H_2O = 2NaHCO_3(s) \quad (1\text{-}5)$$

The primary advantages of these materials are low cost and minimal degradation. Potassium carbonate promoted by piperazine or other promoters has been considered for

CO_2 separation. Vacuum stripping for solvent regeneration has been used, and vapor recompression may be required. A major advantage of carbonates over amine-based systems is the significantly lowered energy required for regeneration. However, sodium and potassium carbonate aqueous solutions have a number of problems in practice. The solutions tend to react only relatively slowly with CO_2 and the heat requirements for regeneration of the solution is large compared to the various alkanolamine based processes. Solution concentrations are limited by the precipitation of bicarbonate salts and solution temperatures are high. Foaming is also reported to be a concern. Corrosion problems may be severe depending on input gas composition, but various corrosion inhibitors have been employed effectively in some circumstances.[19]

1.3 SORBENT-BASED SYSTEMS

1.3.1Activated carbons

Activated carbons are solid sorbents with high porosity, especially micro- and mesopores, which are used in a wide range of household, medical, industrial, military and scientific applications, including gas-phase and liquid-phase processes. The principle of activated carbons adsorbing CO_2 is schematically illustrated in Figure 1.4. The activation process together with the intrinsic nature of the precursors strongly determines the adsorption characteristics of the resulting activated carbons.[20] Anthracites are a kind of activated carbon that has drawn great attention due to their inherent chemical properties,

fine structure and relatively low cost, making them excellent raw materials for the production of activated carbons with high microporosity.[21]

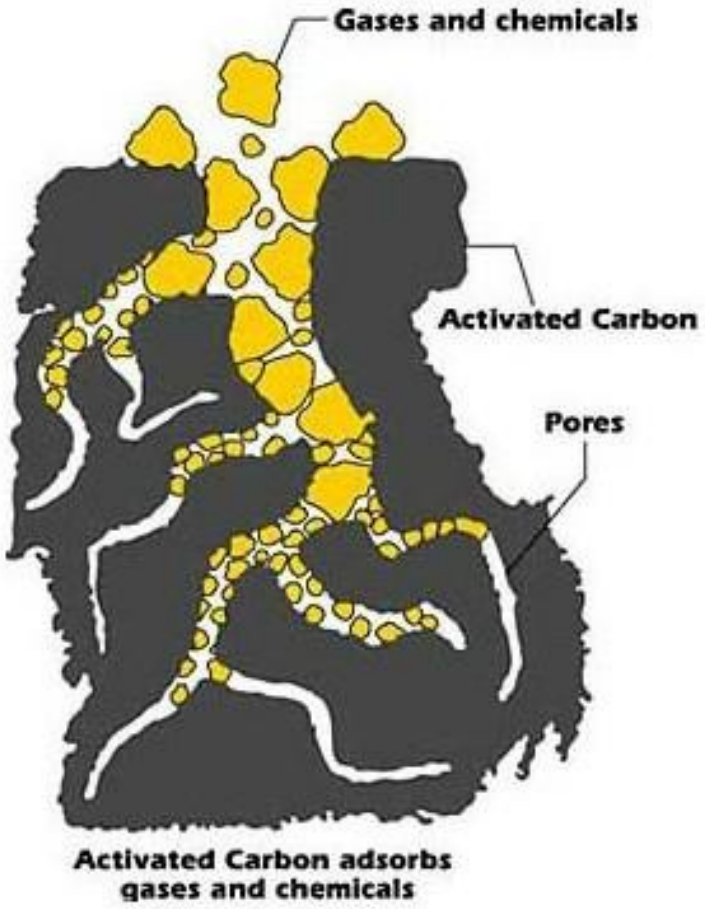

Figure 1.4 The schematic process of activated carbon adsorbing CO_2[22]

According to the results from Maroto-Valer group[20], CO_2 capture does not show a linear relationship with the surface area. The highest CO_2 adsorption capacity was 65.7 mg CO_2/g adsorbent for the anthracite activated at 800 ℃ for 2 h with a surface area of

540 m^2/g. The anthracite with the highest surface area of 1,071 m^2/g only had a CO_2 adsorption capacity of 40 mg CO_2/g adsorbent. This could be explained by certain size pores being effective for CO_2 adsorption. Also, the NH_3 treatment and polyethylenimine (PEI) impregnation increased the CO_2 capture capacity of the activated anthracites at higher temperatures, due to the introduction of alkaline nitrogen groups on the surface.

1.3.2 Carbon molecular sieves and molecular baskets

Molecular sieves are a range of specially designed sieves that separate molecules based on their molecular weight or molecular size. This technology is believed to be cost-effective and can be adapted to a variety of carbon sequestration schemes[23]. There were many research activities aiming to improve the CO_2 adsorption by chemically treat the molecular sieve surface. Adsorbents based on high surface area inorganic supports that incorporate basic organic groups, usually amines, are of particular interest. The interaction between the basic surface and acidic CO_2 molecules is thought to result in the formation of surface ammonium carbonate under anhydrous conditions and in the form of ammonium bicarbonate and carbonate species in the presence of water.[24]

"Molecular basket" was first explored as a new concept by Xu *et. al.*[25]. It is a high capacity, highly selective CO_2 adsorbent. This adsorbent is based on mesoporous molecular sieve of MCM-41 impregnated with polyethylenimine (PEI) (see Fig. 1.5). The use of MCM-41 shows a synergetic effect on the adsorption of CO_2 by PEI. With the

increase in PEI loading, the surface area, pore size and pore volume of the loaded MCM-41 decrease. When the loading is higher than 30 wt%, the mesoporous pores began to be filled with PEI and the adsorbent shows a synergetic effect on the adsorption of CO_2 by PEI. At PEI loading of 50 wt%, the highest CO_2 adsorption capacity of 246 mg/g PEI is obtained, which is 30 times higher than that of MCM-41 and is about 2.3 times that of the pure PEI.[26] This molecular basket can selectively capture CO_2 for the separation of CO_2 from simulated, natural gas-fired and coal-fired flue gases

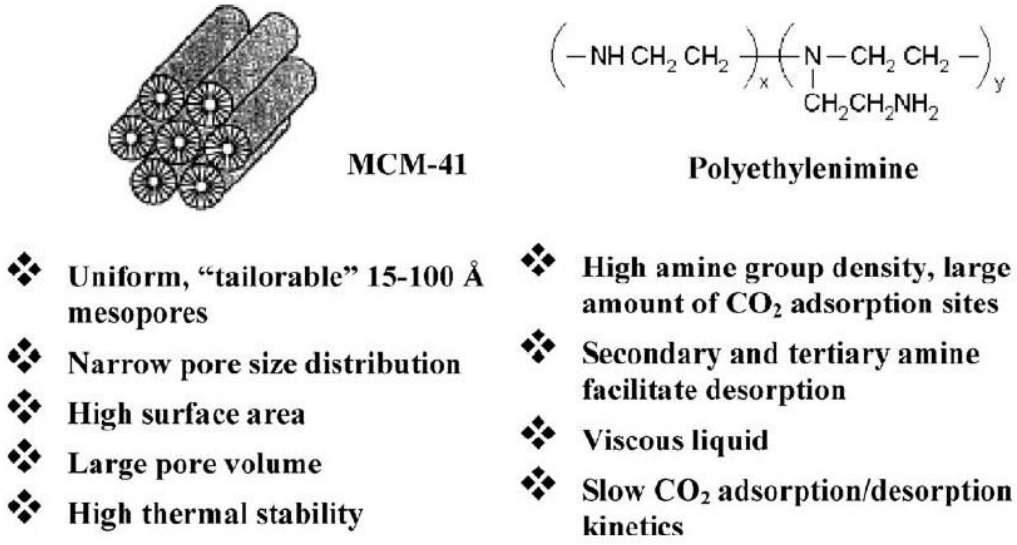

Figure 1.5 Formulation of MCM41-PEI as CO_2 "molecular baskets"[26]

1.3.3 Zeolites

Zeolites are crystalline aluminosilicates with uniform pore structure and a minimum channel diameter range of 0.3-1.0 nm as shown in Figure 1.6. The presence of molecular-sized cavities and pores make the zeolites effective as shape-selective materials for a wide range of separation applications. Separation occurs in zeolite membranes by both molecular sieving and surface diffusion mechanisms. Zeolites are typically employed at elevated pressures (above 2 bar), and their adsorption capacity has been shown to be greatly reduced by the presence of moisture in the gas, thereby necessitating very high regeneration temperatures (often in excess of 300^{o}C).[27, 28] These additional recovery costs for their regeneration pose a significant disadvantage.

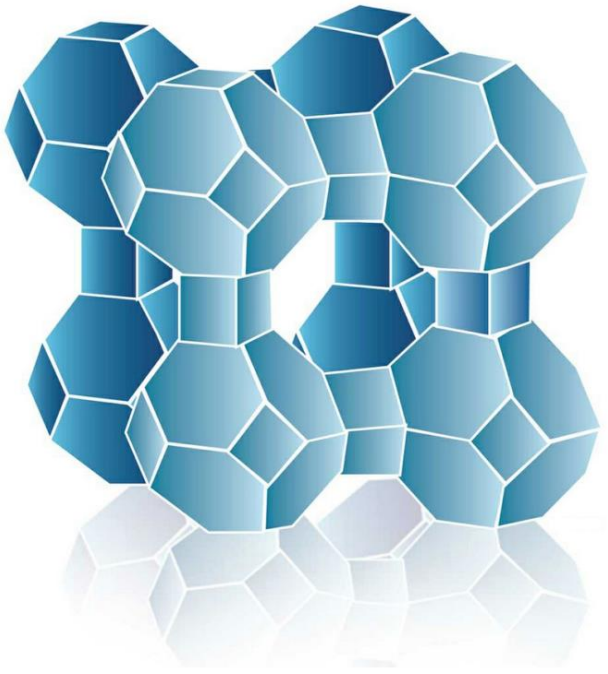

Figure 1.6 Schematic of crystal structure of Zeolite.[29]

1.3.4 Metal oxides

$CaO/CaCO_3$ solid sorbents can be used for CO_2 separation. The basic separation principle in these systems is depicted in Figure 1.7.[30] One of the advantages of this type of looping cycle is that it uses a very cheap and widely available regeneratable sorbent that allows high makeup flows of fresh sorbent at a reasonable cost.[31] A synergy could exist for a cement plant and a power plant in these conditions. However, it is obvious that lower makeup flows will be more attractive for most applications. This requires higher circulation rates of solids between carbonator and calciner and the sorbent to operate a larger number of cycles.

Shimizu et al.[32] proposed the calcination of the sorbent by burning a fraction of the fuel in the calciner with O_2/CO_2. Other calcination options are under development to avoid the use of an air separation unit. For example, it has been proposed by Abanades et al.[33] to use heat carriers, such as sintered CaO (particle density higher than 3,000 kg/m^3) circulating between a high-temperature combustion chamber and the calciner, where they are also separated from the sorbent (particle density below 1,800 kg/m^3) by segregation. Other indirect calcination options have been proposed by Ziock et al.[34]. In all these options virtually pure CO_2 can be obtained in the calciner, since no gas other than CO_2 can be produced from the calcination reaction.

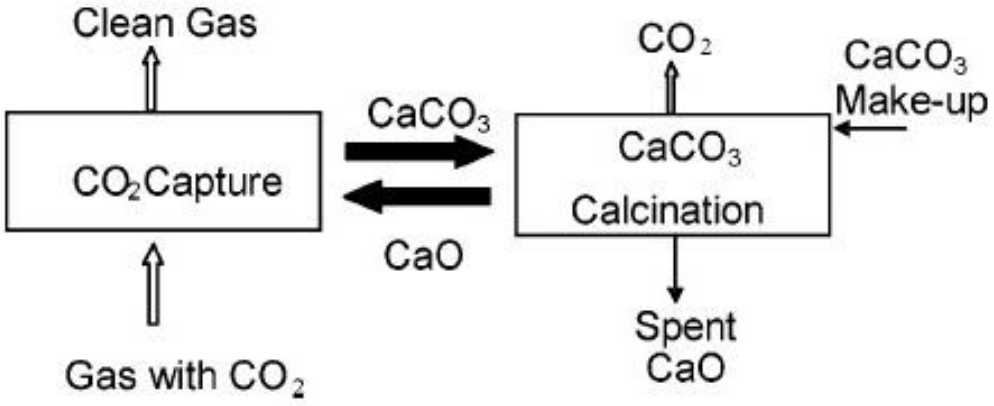

Figure 1.7 Diagram of the proposed calcination/carbonation loop.[30]

1.3.5 Metal organic frameworks

Metal organic frameworks (MOFs) are a new class of hybrid material built from metal ions with well-defined coordination geometry and organic bridging ligands. They are extended structures with carefully sized cavities that can adsorb CO_2. MOFs have received considerable attention during the past couple of years. This may be due to the high mass flux, thermal stability, adjustable chemical functionalities, extra high porosity, and availability of hundreds of well characterized materials reminiscent to zeolites.[35] Over 600 chemically and structurally diverse MOFs have been developed over the past several years. Fig. 1.8 shows a range of the most common crystal structure of MOFs. Yaghi and co-workers have shown that MOF-177 exhibits a CO_2 sorption capacity of 1.4 g of CO_2 per gram of sorbent material.[36] They also reported that a MOF replete with open

magnesium sites, Mg-MOF-74 [Mg_2(DOT); DOT: 2,5-dioxidoterephthalate], has excellent selectivity, facile regeneration, and among the highest dynamic capacities reported for retaining CO_2 in porous materials. Specifically, when Mg-MOF-74 is subjected to a gas stream containing 20% CO_2 in CH_4, a percentage in the range relevant to industrial separations, it captures only CO_2 and not CH_4.[37] S. Couck *et.al.* have demonstrated that metal-organic frameworks can be effectively functionalized with amino groups. The presence of such functional groups together with OH groups of the MIL-53 drastically enhances the affinity for CO_2, resulting in a very large selectivity in CO_2/CH_4 separations.[38]

1.3.6 Lithium Zirconate

Lithium zirconate (Li_2ZrO_3) has attracted attention as a promising sorbent for CO_2 adsorption at high temperatures (in the range of 400 ℃ to 800 ℃) due to its highly stable adsorption reactivity and thermal stability. Carbonation and calcination are expressed by the reversible equilibrium reaction as follows:

$$Li_2ZrO_3(s) + CO_2(g) = Li_2CO_3(s) + ZrO_2(s) \quad (1\text{-}6)$$

The CO_2 capture mechanism is schematically shown in Figure 1.9. Lithium zirconate has a high capture capacity (~4.5 mmol/g) and good stability over many regeneration cycles. Moreover, it has high selectivity for CO_2 and low affinity for N_2.[39] At atmospheric pressure, the forward reaction (carbonation) is thermodynamically

favorable up to 800 ℃. Calcination dominates at temperatures above 800 ℃. The XRD pattern for structure modification during sorption and desorption indicates that CO_2 carbonation using Li_2ZrO_3 is reversible.[40] The limitation of Li_2ZrO_3 is that it can only absorb CO_2 up to 28.7% of its own weight.[41]

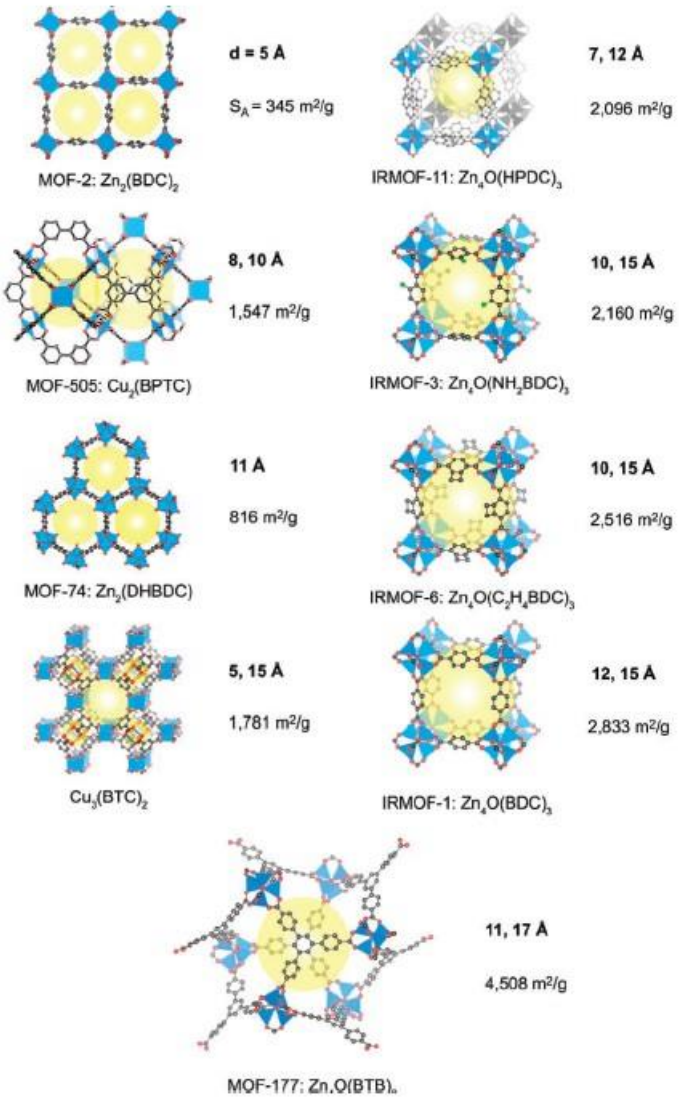

Figure 1.8 Crystal structure of MOFs examined for CO_2 storage capacity at room temperature. [36]

1.3.7 Organic/Inorganic Hybrid Materials

Recently, new organic/inorganic hybrid materials have shown great potential for CO_2 capture, resulting from an increase in the accessible number of sorption sites per mass of sorbent. Sorbents in this category include covalently amine-impregnated silica supports such as amine-modified silane and polymerized reactive amine on silica. The common synthesis methods for covalently amine-impregnated adsorbents are saline chemistry and polymerization. The schematic structures of various amines found on amine-impregnated mesoporous silica (SBA-15) created by surface reaction and surface polymerization, as shown in Figure 1.10[42].

The grafting process of the hybrid aminosilica is achieved by accumulating alkoxy groups from using silane chemistry on the surface silanols to create covalent bonds to the silica surface through the breaking of Si-O-Si bonds, including organic functionalities through substitution on the silane. These silane-modified samples can be reformed to make large amine-loaded dendritic structures that are tethered mainly in the pore space.

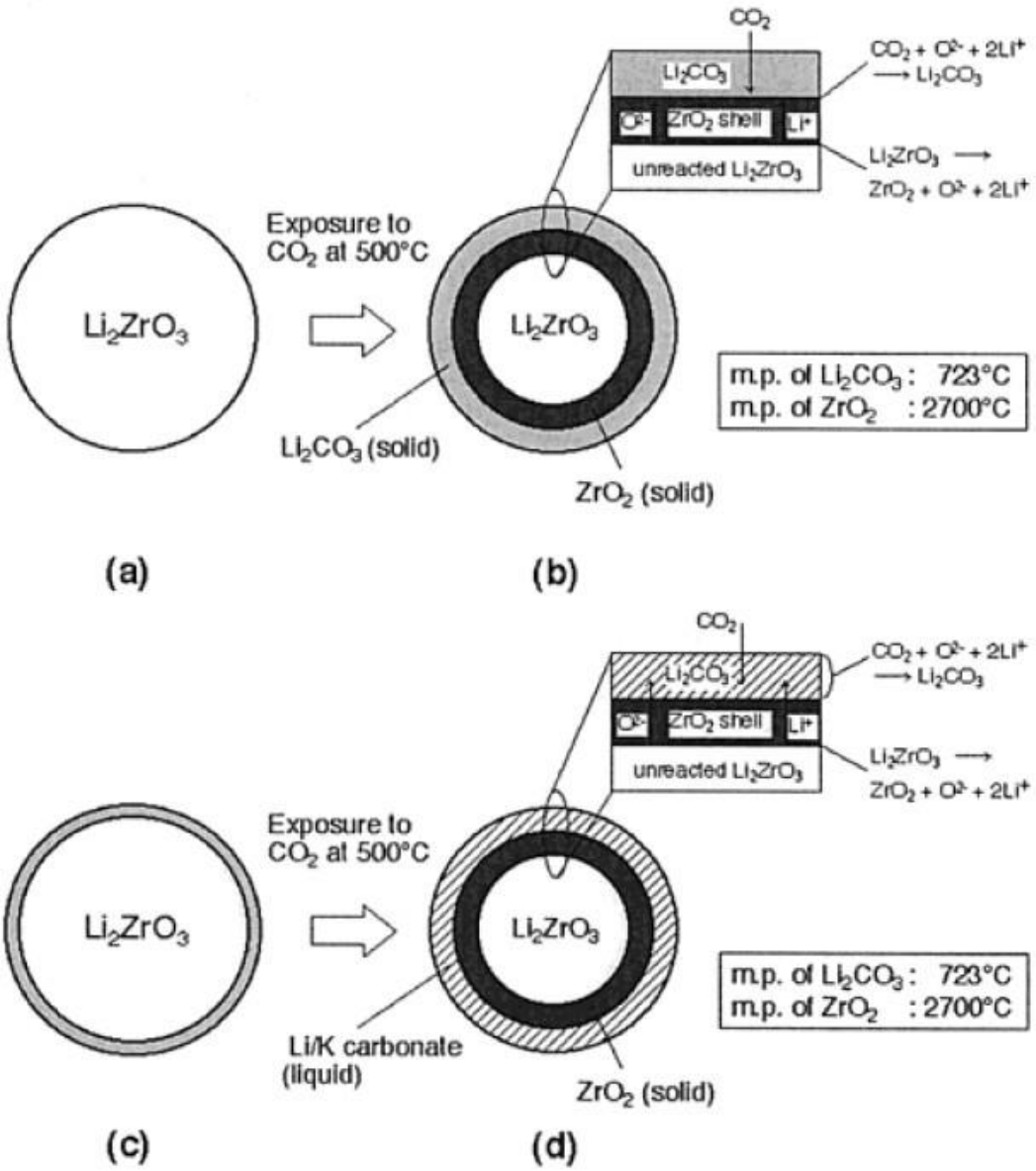

Figure 1.9 Schematic illustration of carbonation mechanism on pure and modified Li_2ZrO_3.

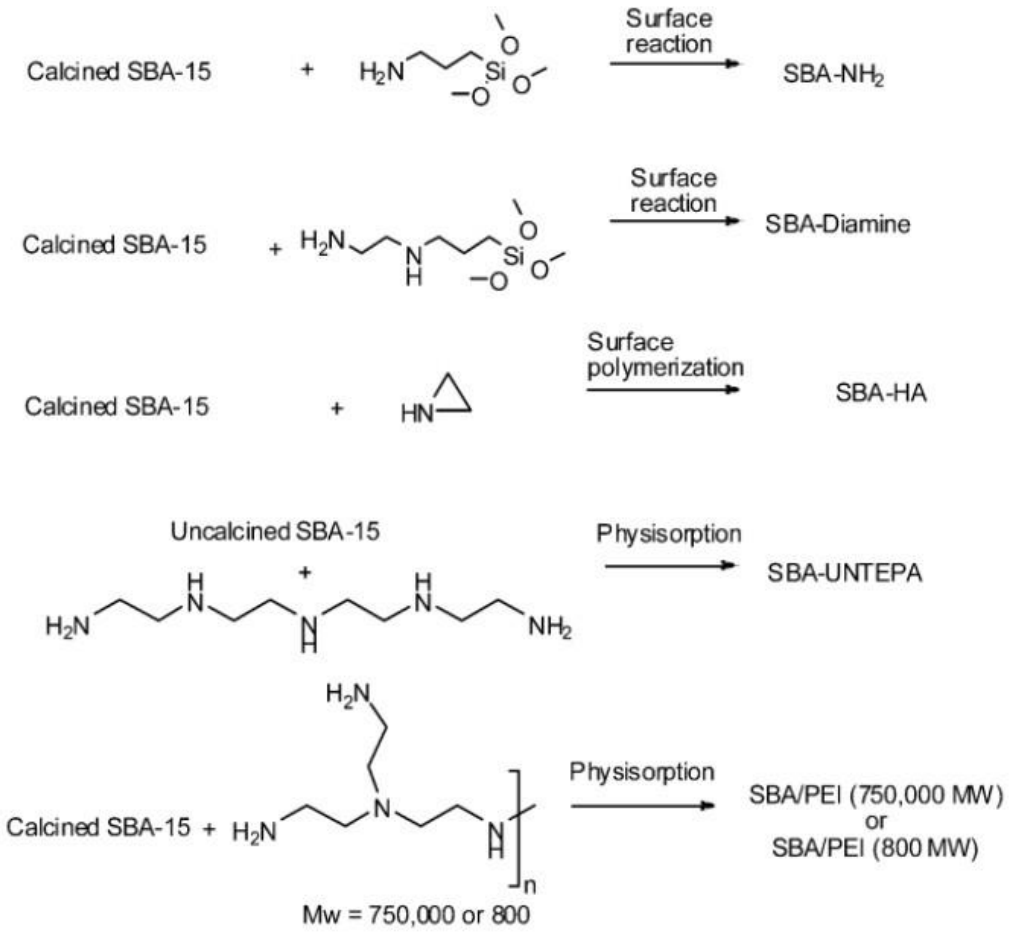

Figure 1.10 Schematic structure of various amines modified SBA-15. [42]

1.4 MEMBRANE-BASED SYSTEMS

The development of a membrane separator for the selective removal of CO_2 in the presence of CO, H_2, H_2O, and H_2S (fuel gas) or N_2, O_2, H_2O, SO_2, NO, and HCl (flue gas) would be of tremendous economic advantages. Membrane separation processes provide several advantages over other conventional separation techniques[43]. First, the membrane process is a viable energy-saving alternative for CO_2 separation, since it does

not require any phase transformation. Second, the necessary process equipment is very simple with no moving parts, compact, relatively easy to operate and control, and also easy to scale-up.

1.4.1 Inorganic membranes

The advantages of inorganic membranes are that it is highly stable at high temperatures and can be resistant to harsh conditions. Inorganic membranes can be classified into two categories based on their microstructure: porous and dense[44]. In porous inorganic membranes, a porous thin top layer is supported on a porous metal or ceramic support, which provides mechanical strength but offers minimum mass-transfer resistance. Alumina, carbon, glass, silicon carbide, titania, zeolite, and zirconia membranes are mainly used as porous inorganic membranes supported on different substrates, such as α-alumina, γ-alumina, zirconia, zeolite, or porous stainless steel. The porous inorganic membrane can be further classified, based on their pore size (microporous (<2 nm) or mesoporous (2 nm to 50 nm) or macroporous (>50 nm)), or symmetry (symmetric, homogeneous structure throughout the membrane, or asymmetric, gradual change in structure throughout the membrane).

The dense inorganic membranes (nonporous material) consist of a thin layer of metal, such as palladium and its alloys (metallic membrane), or solid electrolytes, such as zirconia. These membranes are highly selective for hydrogen or oxygen separation:

transport occurs via solution diffusion method or changed particles in dense membranes. The low permeability across the dense inorganic membranes limits its intended applications, compared to porous inorganic membranes.[45]

Another form of inorganic membrane is the liquid-immobilized membrane, where the pores of the membrane are completely filled with a liquid, which is permselective for certain compounds. The liquid reacts with the permeating component on the feed side to form a complex. The complex diffuses across the membrane and then release the permeate on the product side, and at the same time coverts the liquid back to the feed side.

There are five main transport mechanisms (shown in Fig. 1.11) by which gas separation using porous inorganic membranes can be described. The basis of these transport mechanism are (1) viscous flow, (2) the molecular weight (Knudsen diffusion), (3) surface interactions (surface diffusion), (4) multilayer adsorption (capillary condensation), and (5) the size of molecules (molecular sieving) to be separated.[46]

1.4.1.1 Alumina membranes

The generally mesoporous structure of alumina dictates that transport within membranes fabricated from it will take place by a Knudsen diffusion mechanisms. Since selectivity in this regime is limited, and the rate of diffusion is controlled by molecular weight, alumina membranes are of limited use in the separation of gases.

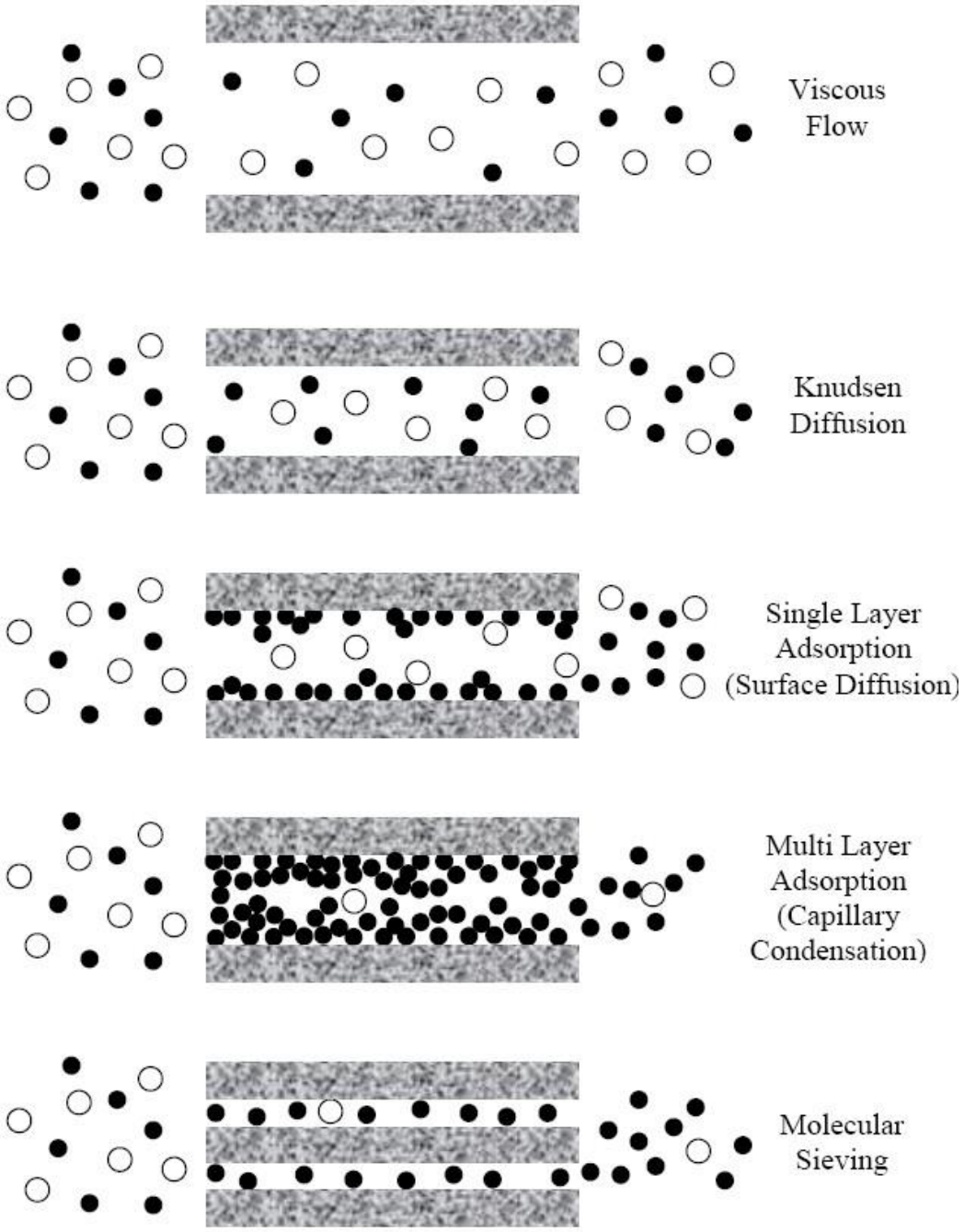

Figure1.11 Transport mechanisms through macro-, meso- and microporous membranes. A) Viscous diffusion, B) Knudsen diffusion, C) Single layer adsorption, D) Multilayer adsorption & E) Molecular sieving [46]

With mixtures such as CO_2/N_2, where the gases have similar mass, and CO_2/H_2, where selectivity toward the heavier component is required, alumina is undesirable as a membrane material.

Alumina finds its use in the separation of gases mainly as a support, where its sound structural properties, and chemical and hydrothermal stabilities beyond 1,000 ^oC make it very desirable.[45] Carreon *et. al.* reported that alumina-supported SAPO-34 membranes as shown in Figure 1.12 had CO_2/CH_4 separation selectivity higher than 170, with CO_2 permeances as high as 2.0 $\times 10^{-6}$ mol/m^2 s Ṕa at 295 K and a feed pressure of 224 kPa. The membranes effectively separated CO_2/CH_4 mixtures up to 1.7 MPa.[47]

1.4.1.2 Zeolite membranes

Zeolites are inorganic crystalline aluminosilicate structures with pores of uniform molecular dimensions. Examples of representative zeolite frameworks are shown in Fig. 1.13 The presence of molecular-sized cavities and pores make the zeolites effective as shape-selective materials for a wide range of separation applications.

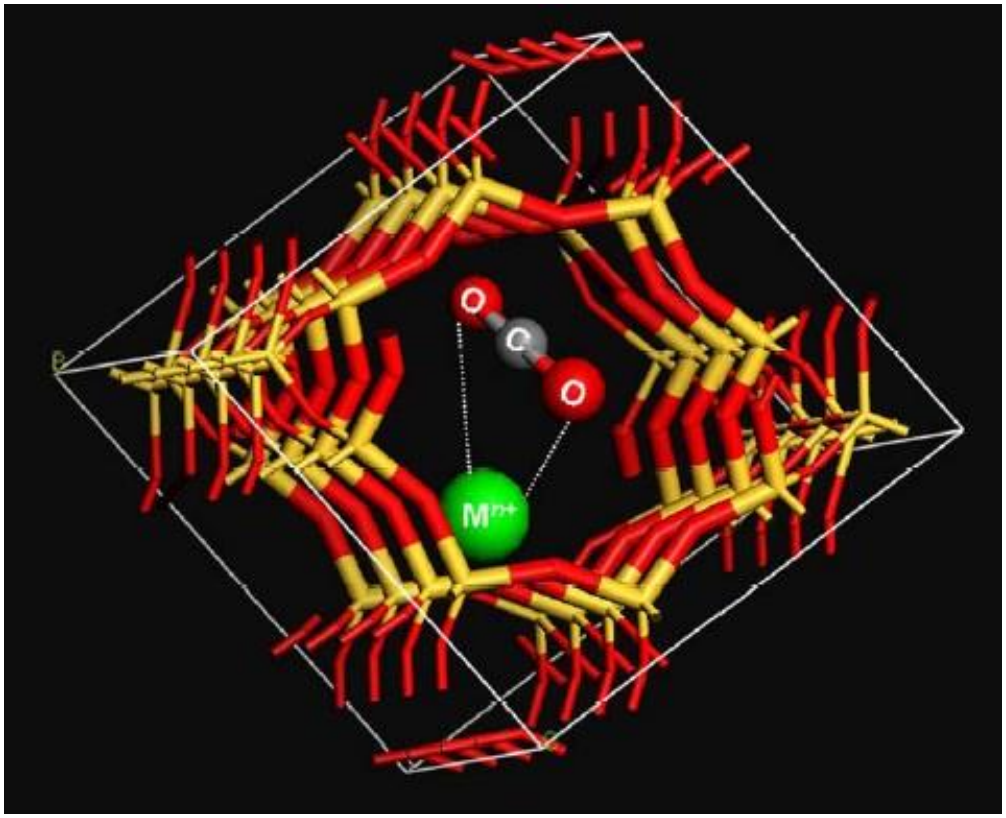

Figure 1.12 Schematic representation of the adsorption of CO_2 on the surface of SAPO-34 pore channel[48]

These cavities are interconnected by pore openings through which molecules can pass. The electrical charge or polarity of the zeolites also functions to attract or sort molecules. This ability to selectively adsorb molecules by size and polarity is the key to the unusual efficiency of synthetic zeolites as the basis for separation. By tailoring the chemistry and structure of the materials used to prepare them, synthetic zeolites can be modified to provide a wide range of desired adsorption characteristics or selectivities, and can be used as a membrane for gas separation applications.[49]

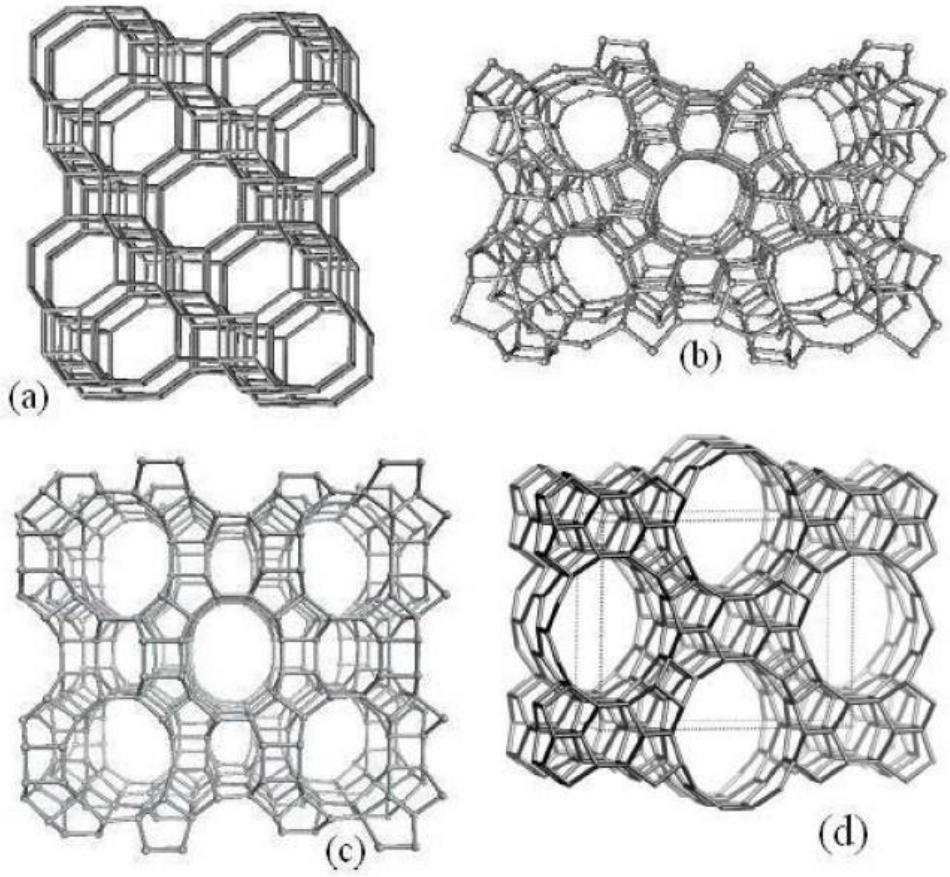

Figure 1.13 Atomic stick representations for the frameworks of zeolite structures. (a) CHA; (b) MFI: (c) MOR; (d)DON.[50]

For those reasons, zeolite membranes were prepared with large pores (FAU, MOR)[51, 52], medium pores (MFI, MEL, FER) [53, 54], and small pores (LTA, CHA, DDR)[55, 56]. Most studies of CO_2 separation have examined medium-pore zeolites such as MFI-type and FAU-type zeolites. Their respective selectivities would be low, because the pores of these zeolites are too large to separate CO_2 from CH_4 with high selectivity. Numerous eight-membered-ring zeolites with small pores have been examined as

candidates for adsorbents that are useful for the separation of small molecules. Small-pore zeolites, such as zeolite T, SAPO-34, and DDR, have pores that have a size that is similar to that of the CH_4 molecule, but which are larger than the CO_2 molecule. For that reason, they are suitable for CO_2/CH_4 separation. High-silica types offer the advantage of hydrophobicity, i. e., they retain their adsorption capacity in water.[57] Other types of zeolites suffer performance degradation from moisture attack.

1.4.1.3 Carbon membranes

Carbon membranes for gas separations are typically produced by the pyrolysis of thermosetting polymers. The pyrolysis temperature, typically in the range of 500 to 1000 ℃, depends upon the type of precursor material and dictates the separation performance of the carbon membranes[45]. Pyrolysis of polymeric compounds leads to carbon material with a narrow pore size distribution below molecular dimensions (< 1 nm), which makes it possible to separate gases with very similar molecular sizes. The predominant transport mechanism of most carbon membranes is molecular sieving. The selection of precursor polymer, the membrane preparation method, and the carbonization process determine the performance of carbon molecular sieve membranes. The mechanical stability can be improved by supporting a thin carbon membrane on a porous support material, such as α-alumina. The high thermal and chemical stability promise these membranes to find

applications in gas separation applications, such as separation of CO_2 in flue gas emissions from power plants.

1.4.1.4 Silica membranes

Silica is a viable starting material for the fabrication of CO_2 selective membranes, primarily because of its innate stability and easy modification of its structures. Unlike alumina, which tends to undergo phase transition at relatively low temperature, or carbon, which can exhibit substantial changes in pore size in oxidizing environments, silica shows exceptional thermal, chemical, and structural stability in both oxidizing and reducing environment. Sol-gel method and chemical vapor deposition (CVD) technique are the most traditional ways used to prepare silica membranes.[45]

1.4.1.5 Perovskite oxide-type membranes

Typically, perovskites are of the form ABO_3, the structure of which is shown in Figure 1.14, where the A component and/or the B component may be doped with other materials to enhance the stability and properties of perovskite oxide-type materials. These ion-conductive perovskite-type oxide membranes have been extensively studied for O_2 separations at elevated temperatures. The stability of perovskite type materials at very high temperatures should attract one's attention towards CO_2 selective membranes at elevated temperatures. S. Morooka *et. al.* reported that $BaTiO_3$ membrane that was

prepared by the sol-gel method can be used to separate CO_2. The separation factor of CO_2 and N_2 through the membrane was 1.12-1.2, which was higher than the value of the Knudsen diffusion mechanism (0.8).[58]

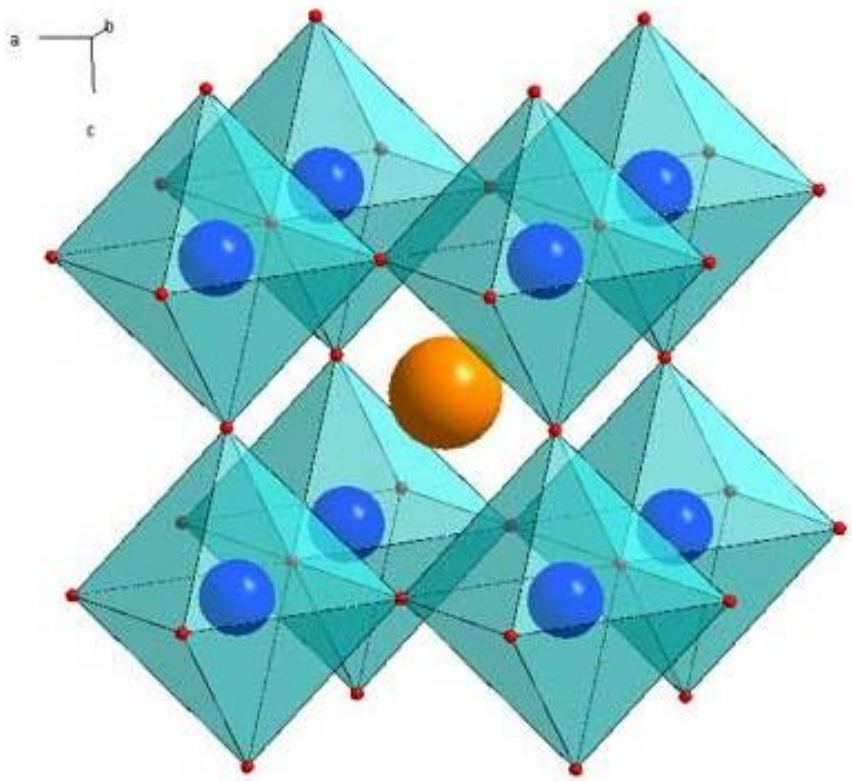

Figure 1.14 Crystal structure of ABO_3; the yellow ball represents A, the blue balls represent B and the red balls represent O.

1.4.1.5 Hydrotalcite membranes

Hydrotalcite (HT) compounds consist of layers of octahedrally coordinated bivalent cations (e.g., Mg^{2+}, Ni^{2+}, Co^{2+}, Zn^{2+}, Cu^{2+}) and trivalent cations (e.g., Al^{3+}, Fe^{3+}, Cr^{3+}), as well as interlayer anions (e.g., CO_3^{2-}, SO_4^{2-}, NO_3^-, Cl^-, OH^-, $[Fe(CN)_6]^{4-}$) and

water[59]. The crystal structure of Hydrotalcites is shown in Figure 1.15. Hydrotalcites show a spinel phase ($MgAl_2O_4$ in addition to γ-Al_2O_3 phase and MgO phase). After calcination at higher temperatures, these compounds lose interlayer anions and water to form mixed oxides that can be used as solid base catalysts (e.g., Mg-Al-O) as well as catalyst supports[60]. Mixed oxides, Mg-Al-O, have also been shown to have high surface area and good stability toward heat treatment, making them viable candidates as ceramic membranes.

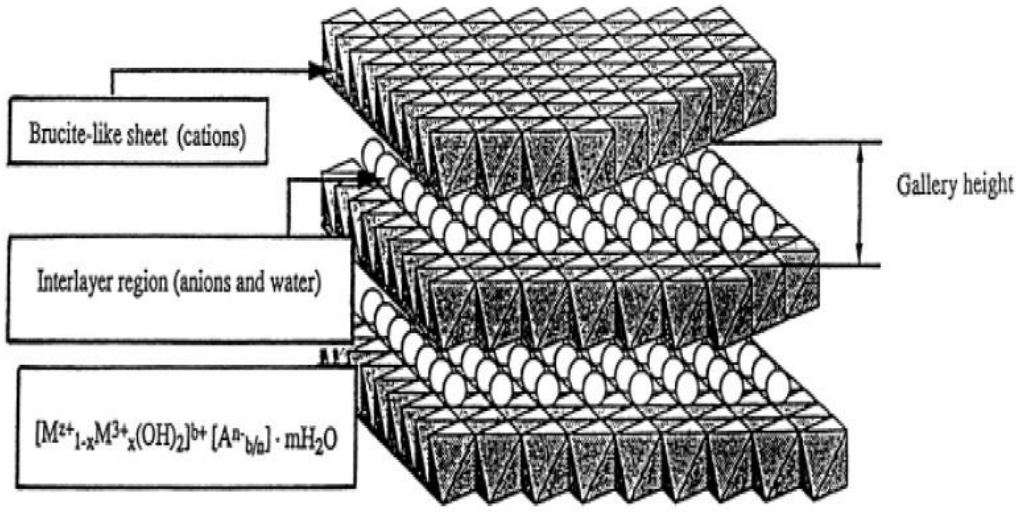

Figure 1.15 Schematic representation of the hydrotalcite-type anionic clay structure.[61]

1.4.2 Polymeric membranes

Polymer membranes have been successfully applied for the separation of carbon dioxide from natural gas streams. The harsh chemically reactive and high temperature flue and fuel gases make the use of polymer membranes unlikely for these applications. Generally, gas molecules transport through a polymeric membrane by a solution-diffusion mechanism. For example, the CO_2 permeate through hydrates tetramethylammonium fluorid tetrhydrate membrane, $[(CH_3)_4N]F\ 4H_2O$,[62] as a kind of facilitated transport membrane, by a solution-diffusion mechanism. Other mechanisms include a molecular sieve effect and Knudsen diffusion[63].

The terms permeability and selectivity are used to describe the performance of a gas separation membrane. There appears to be a trade-off between selectivity and permeability. Gas molecules tend to move through free volumes – the gaps between polymeric structures. Because of the movement of the polymer chains, a channel between gaps can be formed allowing gas molecules to move from one gap to another and thus gas molecules can effectively diffuse through the membrane structure. Selective transport of gases can be achieved by use of a polymer which forms channels of a certain size. Large channels will allow faster diffusion of gases through a membrane at the cost of less selectivity.

Membranes are a low cost means of separating gases when high purity is not vital. There are a number of issues associated with the capture of carbon dioxide from flue gas

which limits the use of membranes. The concentration of carbon dioxide in flue gases is low, which means that large quantities of gases will need to be processed. The high temperature of flue gases will rapidly destroy a membrane, so the gases need to be cooled to below 100 ℃ prior to membrane separation. The membranes need to be chemically resistant to the harsh chemicals contained within flue gases, or these chemicals need to be removed prior to the membrane separation. Additionally, creating a pressure difference across the membrane will require significant amounts of energy.

1.4.3 Facilitated transport membranes

Facilitated transport membranes (FTM) have received a great deal of attentions in gas separations because they offer higher selectivity and larger flux permeability.[64] Higher selectivity in FTM is achieved by incorporating a carrier agent into membrane, which reacts reversibly with the penetrating species. In addition to the solution diffusion mechanism of the polymeric membranes, FTMs also involve a reversible complexing reaction. The permeating species dissolves in the upstream portion of the membrane and reacts with the carrier agent inside the membrane to form a complex. This complex diffuses across the membrane, and then releases the permeants on the downstream side of the membrane, while the agent is simultaneously recovered and diffuses back to the feed side. FTMs can be in a form of fixed carrier membranes, solvent-swollen polymer membrane, and mobile carrier membranes.[38] In the FTMs, thinner membranes are

desirable for faster permeation rate. However, too thin membranes lack mechanical strength and stability. It was also reported that the thinner the FTMs, the lower the selectivity due to shorter diffusion time relative to chemical reaction time in the membrane.[65]

Nakabayashi et al.[66] applied hydrogel, prepared from a vinyl alcohol/acrylic acid-salt copolymer, on a hydrophilic PVdF porous membrane by a spin coating method, followed by heating to get cross-linkage. The cross-linked layer was immersed into a CO_2 carrier solution (2 mol/l of K_2CO_3) to form a water-swollen-gel membrane. The gel membrane was coated on a polydimethylsiloxane support. The authors discovered that K_2CO_3 had the highest permeation and separation factor and was most effective as a CO_2 carrier among several carbonate salts of alkali metals studied. They reported that the water-swollen-gel membrane was stable over 30 days. A much higher permeability and selectivity was observed after adding crown ether, EDTA, or analogous compounds to the K_2CO_3 solution.

1.5 ENZYME-BASED SYSTEM

Biologically based capture systems are another potential way of improving CO_2 capture efficiency. These systems are based upon naturally occurring reactions of CO_2 in living organisms. One of these possibilities is the use of enzymes. An enzyme-based system, which achieves CO_2 capture and release by mimicking the mechanism of the

mammalian respiratory system, is under development by Carbozyme (see Fig. 1.16). The process, utilizing carbonic anhydrase (CA) in a hollow fiber contained liquid membrane, has demonstrated at laboratory-scale the potential for 90% CO_2 capture followed by regeneration at ambient conditions. This is a significant technical improvement over the MEA temperature swing absorption process. The CA process has been shown to have a very low heat of absorption that reduces the energy penalty typically associated with absorption processes. The rate of CO_2 dissolution in water is limited by the rate of aqueous CO_2 hydration, and the CO_2-carrying capacity is limited by buffering capacity. Adding the enzyme CA to the solution speeds up the rate of carbonic acid formation; CA has the ability to catalyze the hydration of 600,000 molecules of carbon dioxide per molecule of CA per second compared to a theoretical maximum rate of 1,400,000[67]. This fast turnover rate minimizes the amount of enzyme required. Coupled with a low make-up rate, due to a potential CA life of 6 months based on laboratory testing, this biomimetic membrane approach has the potential for a step change improvement in performance and cost for large scale CO_2 capture in the power generation sector[68].

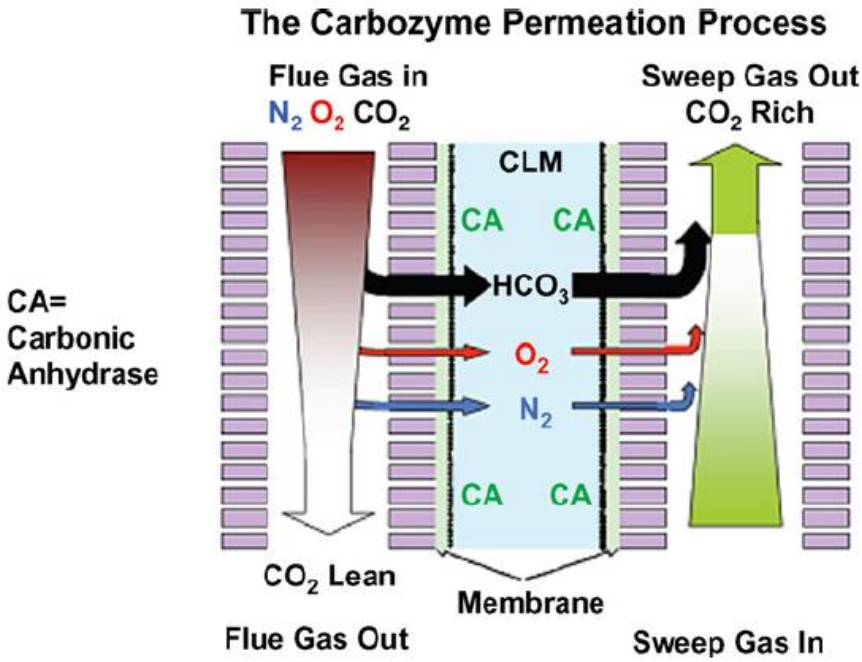

Figure 1.16 Schematic of the Carbozyme permeation process for CO_2 capture.[9]

CHAPTER 2 FUNDAMENTALS OF MIXED CONDUCTING CO_2 SEPARATION MEMBRANES

2.1 WORKING PRINCIPLE OF DUAL-PAHSE MIXED CONDUCTING MEMBRANES

In this dissertation work, two types of mixed conductors have been systematically studied for CO_2 separation from fuel and flue gases: 1) mixed carbonate-ion and oxide-ion conductor (MOCC); 2) mixed carbonate-ion and electron conductor (MECC). The former is deemed more suited for pre-combustion CO_2 separation while the latter is more applicable for post-combustion CO_2 separation. Schematic of such mixed conducting membranes are shown in Fig. 2.1 for (a) MOCC and (b) MECC. These mixed conducting electrochemical CO_2 separation membranes are technically and economically more attractive than conventional electrically driven, molten carbonate fuel cell based CO_2 concentrator since no external electronics are needed.

The working principle of MOCC membranes can be described as follows. At the feed side, oxygen ions (O^{2-}) of the oxide-ion conductor react with CO_2 to form CO_3^{2-} under the chemical gradient of CO_2:

$$CO_2 + O^{2-} = CO_3^{2=} \qquad (2\text{-}1)$$

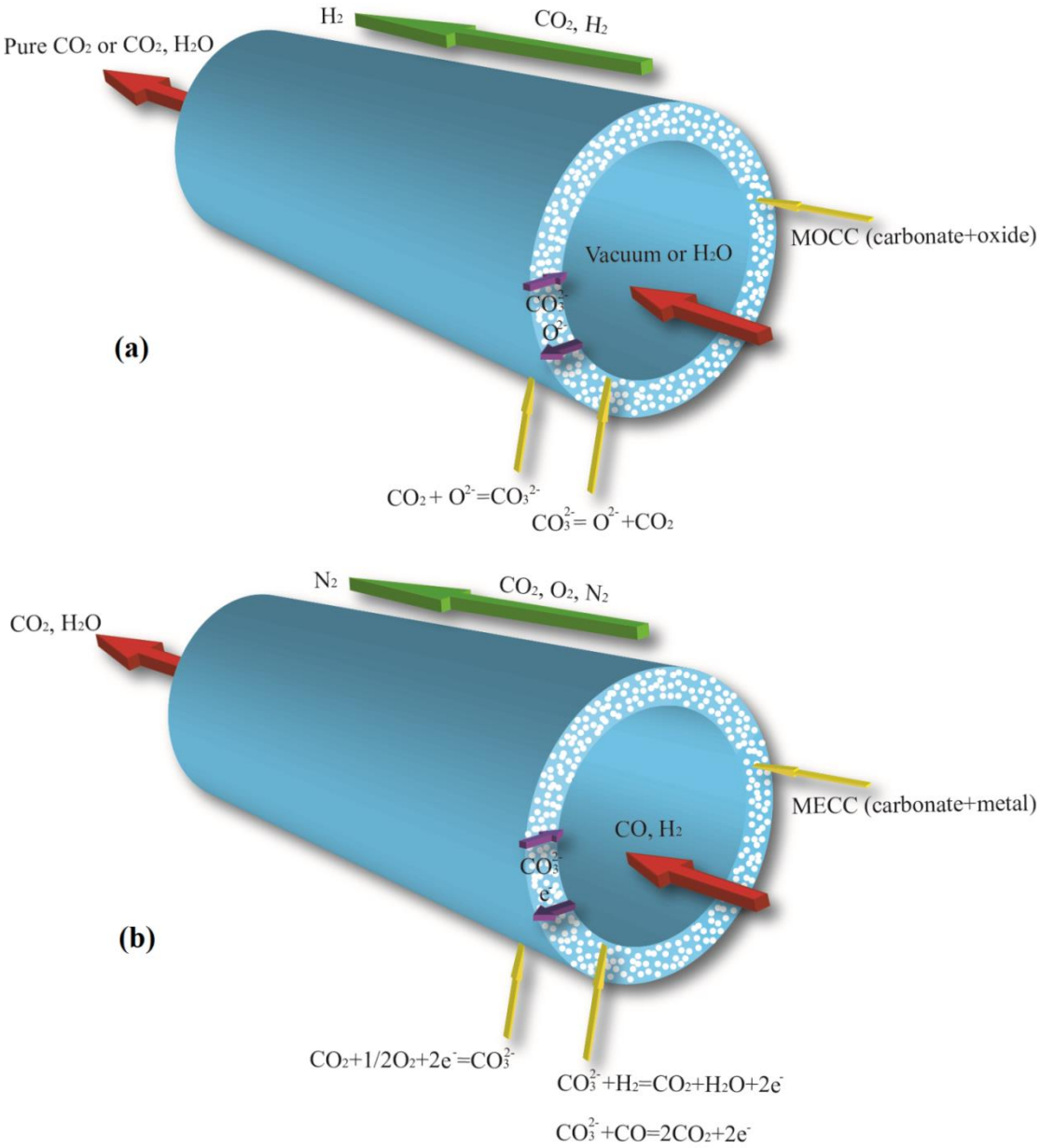

Figure 2.1 Schematic and working principles of the mixed conducting electrochemical CO_2 separation membranes: (a) MOCC; (b) MECC

The formed CO_3^{2-} migrate through the membrane accompanied by charge-balancing opposite flow of O^{2-}. At the permeate side, CO_3^{2-} dissociate into CO_2 and O^{2-} via the following reaction:

$$CO_3^{2=} = CO_2 + O^{2-} \quad (2\text{-}2)$$

Overall reaction can then be expressed by:

$$CO_2\,(\text{feed}) = CO_2\,(\text{permeate}) \quad (2\text{-}3)$$

The driving forces of the transport are partial pressure gradients of CO_2 and O_2 across the membrane

The working principle of MECC can be described as follows. At the feed side, CO_2 and O_2 are reduced into CO_3^{2-} by combining with electrons e^- from the membrane:

$$CO_2 + \frac{1}{2}O_2 + 2e^- = CO_3^{2-} \quad (2\text{-}4)$$

The formed CO_3^{2-} migrates through the membrane accompanied by the charge-balancing opposite flow of e^-. At the permeate side, the transported CO_3^{2-} react with H_2 and CO to form CO_2 and H_2O and give off large amount of recoverable heat (Δ):

$$CO_3^{2-} + H_2 = CO_2 + H_2O + 2e^- + \Delta \quad (2\text{-}5)$$

$$CO_3^{2-} + CO = 2CO_2 + 2e^- + \Delta \quad (2\text{-}6)$$

Overall reaction can then be written by

$$CO_2(\text{feed}) + H_2(\text{permeate}) + \frac{1}{2}O_2(\text{feed}) = H_2O(\text{permeate}) + CO_2(\text{permeate}) + \Delta \quad (2\text{-}7)$$

$$CO_2(\text{feed}) + CO(\text{permeat e}) + \frac{1}{2}O_2(\text{feed}) = 2CO_2(\text{permeate}) + \Delta \quad (2\text{-}8)$$

The driving forces for the transport are partial pressure gradients of CO_2 and O_2 across the membrane.

2.2 FLUX THEORY OF DUAL-PHASE MIXED CONDUCTING CO_2 SEPARATION MEMBRANES

2.2.1 Background

The development of flux theory for dual-phase mixed conducting CO_2 separation membranes has followed the conventional transport theory – Wagner equation[69], i. e., the flux density is proportional to the chemical gradient of the active species. Lin et al[70] derived the flux density of CO_2, J_{CO2}, of a$La_{0.6}Sr_{0.4}Co_{0.8}Fe_{0.2}O_{3-\delta}$ (LSCF)–carbonate dual phase membrane (similar to MOCC) in the following form

$$J_{CO_2} = -\frac{\varepsilon}{\tau}\left(\frac{RT\phi\sigma_i}{4(P_{CO_2}^{'} - P_{CO_2}^{''})F^2L}\right)\ln\frac{P_{CO_2}^{''}}{P_{CO_2}^{'}} \quad (2\text{-}9)$$

where ε is the porosity and τ is the tortuosity factor for the LSCF matrix. Since pores in the LSCF matrix are filled with carbonate, these two parameters determine the transport properties of carbonate-ions. Furthermore, the geometric correction factor ϕ is also considered as the fraction of the porous LSCF matrix. Physically, it represents the ratio of the relative cross-sectional area for solid phase to the solid tortuosity for oxygen ion transport in the solid skeleton of the porous LSCF matrix; $P_{CO_2}^{'}$ and $P_{CO_2}^{''}$ are carbon

dioxide partial pressures (Pa) in the feed and permeate streams, respectively; L is the membrane thickness (m). R is the gas constant, F is Faraday's constant, T is absolute temperature.

A similar analytical model was also derived for the flux of CO_2, J_{CO2} (mol cm^{-2} s^{-1}) through a dual-ionic system (similar to MOCC) by Zhu *et. al.*.[71] For a purely ionic transport, the carbon dioxide flux can be written as:

$$J_{CO_2} = -\frac{RT}{4F^2L}\frac{\varphi\sigma_c(1-\varphi)\sigma_o}{\varphi\sigma_c+(1-\varphi)\sigma_o}\ln\frac{P_{CO_2}^{''}}{P_{CO_2}^{'}} \tag{2-10}$$

where L is the membrane thickness, σ_c and σ_o are the conductivities of the CO_3^{2-} and vacancy charge carriers (O^{2-}), respectively; φ is the volume fraction of the carbonate phase.

The flux density of CO_2 for a MECC dual-phase membrane has been proposed as [72]:

$$J_{CO_2} = -\frac{3RT}{8F^2L}\int_{P_{CO_2}^{'}}^{P_{CO_2}^{''}}\frac{\sigma_{ion}\sigma_{el}}{\sigma_{ion}+\sigma_{el}}d(\ln P) \tag{2-11}$$

where P is the total pressure of the CO_2 and O_2 mixture. At the permeation temperature, the ionic conductivity of CO_3^{2-} in the molten carbonate phase is much smaller than the electronic conductivity for the stainless-steel phase. Therefore, the conductivity contribution term in Eq. (2-11) can be reduced to ionic conductivity only. Considering the porosity (ε) and tortuosity (τ) of the metal support, and assuming CO_2 pressure independent ionic conductivity, integration of Eq. (2-11) gives CO_2 permeance:

$$J_{CO_2} = -\frac{9RT}{16F^2L}\sigma_{ion}\ln\left(\frac{P_{CO_2}^{''}}{P_{CO_2}^{'}}\right)\frac{\varepsilon}{\tau}\frac{1}{P_{CO_2}^{'} - P_{CO_2}^{''}} \quad (2\text{-}12)$$

2.2.2 CO_2 flux density of MOCC membrane developed in this thesis

Based on the classical transport theory, we have also derived flux equations for MOCC and MECC dual-phase membranes from a general and generic perspective. For bulk-diffusion controlled charge transport in homogeneous mixed conductors, the flux density J_i of the active species I is given by:

$$J_i = -\frac{D_i C_i}{RT}\nabla\eta_i = -\frac{\sigma_i}{(z_i F)^2}\nabla\eta_i = -\frac{\sigma_i}{(z_i F)^2}(\nabla\mu_i + z_i F\nabla\phi) \quad (2\text{-}13)$$

where D_i, C_i, σ_i and z_i represent the self-diffusivity, concentration, conductivity and charge of species i, respectively; η_i and μ_i are electrochemical and chemical potentials of species i; R, F and T have their usual meanings. Applying eq. (2-13) to a homogeneous mixed CO_3^{2-} (CO_3^{2-}=1) and O^{2-} (O^{2-}=2) conductor, we can arrive at the following flux expression

$$J_1 = -\frac{\sigma_1\sigma_2}{z_1^2F^2}\left(\frac{\nabla\mu_1 - z_1/z_2\nabla\mu_2}{\sigma_1+\sigma_2}\right) \quad (2\text{-}14)$$

Considering the local chemical equilibrium $CO_2 + O^{2-} = CO_3^{2-}$, one has

$$J_1 = J_{CO_3^{2-}} = -\frac{1}{4F^2}\left(\frac{\sigma_{CO_3^{2-}}\sigma_{O^{2-}}}{\sigma_{CO_3^{2-}}+\sigma_{O^{2-}}}\right)\nabla\mu_{CO_2} = -\frac{RT}{4F^2}\left(\frac{\sigma_{CO_3^{2-}}\sigma_{O^{2-}}}{\sigma_{CO_3^{2-}}+\sigma_{O^{2-}}}\right)\nabla\ln P_{CO_2} \quad (2\text{-}15)$$

Assuming that $\sigma_{CO_3^{2-}}$ and $\sigma_{O^{2-}}$ are both P_{CO2} independent, the steady-state flux $J_{CO_2} = J_{CO_3^{2-}}$ can be integrated across the thickness L of the membrane exposed to a gradient of high P_{CO2}' and low P_{CO2}"

$$J_{CO_2} = J_{CO_3^{2-}} = -\frac{RT}{4F^2}\left(\frac{\sigma_{CO_3^{2-}}\sigma_{O^{2-}}}{\sigma_{CO_3^{2-}} + \sigma_{O^{2-}}}\right)\ln\frac{P''_{CO_2}}{P'_{CO_2}} \tag{2-16}$$

For dual-phase ceramic-carbonate mixed-ion conductors, the microstructural and concentration effects have to be considered in the flux equation. The microstructural factors such as porosity ε and tortuosity τ would have a direct impact on the diffusivity of each migrating ion. The effective diffusivity of species i, D_i^{eff}, can be expressed by

$$D_i^{eff} = \frac{\varepsilon}{\tau} D_i \tag{2-17}$$

On the other hand, the concentration of each species would also be changed by the phase volume ratio. The effective concentration C_i^{eff} (volume basis) can be corrected by

$$C_i^{eff} = \varphi_i C_i \tag{2-18}$$

where φ is the volume fraction of carbonate phase. Substituting eqs. (2-17) and (2-18) into eqs. (2-13 to 2-16) leads to the modified flux equation for dual-phase mixed carbonate-ion and oxide-ion conducting membranes

$$J_{CO_2} = -\frac{RT}{4F^2 \mathrm{L}}\frac{\varepsilon}{\tau}\left(\frac{\varphi\sigma_{CO_3^{2-}}(1-\varphi)\sigma_{O^{2-}}}{\varphi\sigma_{CO_3^{2-}} + (1-\varphi)\sigma_{O^{2-}}}\right)\ln\frac{P''_{CO_2}}{P'_{CO_2}} \tag{2-19}$$

2.2.3 CO_2 flux density of MECC membrane developed in this thesis

Similarly, use of eq. (2-13) but with a substitution of O_2-=1 by e^-=2 leads to the following CO_2 flux density for MECC membranes:

$$J_1 = -\frac{\sigma_1\sigma_2}{z_1^2 F^2}\left(\frac{\nabla\mu_1 - z_1/z_2\nabla\mu_2}{\sigma_1+\sigma_2}\right) \tag{2-20}$$

Considering the local chemical equilibrium $CO_2 + 1/2O_2+2e^- = CO_3^{2-}$, one has

$$J_1 = J_{CO_3^{2-}} = -\frac{3}{8F^2}\left(\frac{\sigma_{CO_3^{2-}}\sigma_{e^-}}{\sigma_{CO_3^{2-}}+\sigma_{e^-}}\right)\left(\nabla \ln P_{CO_2} + \frac{1}{2}\nabla \ln P_{O_2}\right) \tag{2-21}$$

Assuming that $\sigma_{CO_3^{2-}}$ and σ_{e^-} are both P_{CO2} and P_{O2} independent, the steady-state flux $J_{CO_2} = J_{CO_3^{2-}}$ can be integrated across the thickness L of the membrane exposed to a gradient of high P_{CO2}', P_{CO2}' and low P_{CO2}", P_{CO2}"

$$J_{CO_2} = J_{CO_3^{2-}} = -\frac{3RT}{8F^2}\left(\frac{\sigma_{CO_3^{2-}}\sigma_{e^-}}{\sigma_{CO_3^{2-}}+\sigma_{e^-}}\right)\ln\frac{P''_{CO_2}P''^{1/2}_{O_2}}{P'_{CO_2}P'^{1/2}_{O_2}} \tag{2-22}$$

Considering the microstructural volumetric effects aforementioned, the final CO_2 flux density for MECC membranes can be written by:

$$J_{CO_2} = -\left(\frac{\varepsilon}{\tau}\right)\frac{3RT}{8F^2L}\frac{\varphi\sigma_{CO_3^{2-}}(1-\varphi)\sigma_{e^-}}{\varphi\sigma_{CO_3^{2-}}+(1-\varphi)\sigma_{e^-}}\ln\frac{P''_{CO_2}P''^{1/2}_{O_2}}{P'_{CO_2}P'^{1/2}_{O_2}} \tag{2-23}$$

2.2.4 Dependence of CO_2 flux densities on variables

From the flux equations (2-19) and (2-23), there are several ways to improve CO_2 flux densities of the MOCC and MECC membranes：reducing membranes thickness L, increasing the ratio of porosity to tortuosity, improving oxygen-ion conductivity of the oxide phase in MOCC membranes or carbonate-ion conductivity of the carbonate phase in MECC membranes.

According to the basic electrochemical reaction (2-4), on the other hand, it seems to be reasonable to assume that $\sigma_{CO_3^{2-}}$ is both P_{O2} and P_{CO2} dependent and follows:

$$\sigma_{CO_3^{2-}} = \sigma^{o} P_{CO_2} P_{O_2}^{1/2} \tag{2-24}$$

Substituting eq. (2-24) into eq. (2-11) and integrating over the range of chemical gradient and thickness with the assumption of $\sigma_e >> \sigma_{CO_3^{2-}}$ yield the following flux equation:

$$J_{CO_2} = -\left(\frac{\varepsilon}{\tau}\right)\frac{3RT}{8F^2L}\varphi\sigma_{CO_3^{2-}}\left(P_{CO_2}^{''}P_{O_2}^{''1/2} - P_{CO_2}^{'}P_{O_2}^{'1/2}\right) \tag{2-25}$$

2.3 MODELS FOR MECHANISTIC CHARGE TRANSPORT

2.3.1 Mechanism for charge transport in MOCC membranes

Two parallel ionic pathways are proposed in Fig. 2.2. The ionic **Pathway-1** is a conventional route that considers surface ionization of CO_2 solely at three-phase

boundaries (3PBs), where CO_2, O^{2-} and CO_3^{2-} are simultaneously available, and subsequent transport of CO_3^{2-} through the MC phase and deionization of CO_3^{2-} on the opposite surface. The CO_2-transport enabling reactions are summarized in the second column of Table 2.1. During the CO_2 transport, the flow of O^{2-} acts as the charge compensating flux to that of CO_3^{2-}. The CO_2 ionization reaction (2-24) has been broadly suggested in the literature as the global mechanism for CO_2 transport in dual-phase MOCC, but proceeding with a relatively slower rate. The ionic **Pathway-2** is a hypothesized ionic transport route parallel to the **Pathway-1**. It encompasses surface ionization of CO_2 at 2PBs of CO_2/MC interface (reaction (2-28) in Table 2-1) and internal ionic transfer at 2PBs of SDC/MC interface (reaction (2-39) in Table 2-1).

The species $C_2O_5^{2-}$ (dicarbonate or pyrocarbonate anion) possesses a $(CO_2)_n$ chainlike structure and is deemed as an intermediate product of CO_2 chemisorption on the surface of an alkali carbonate melt. Once formed, $C_2O_5^{2-}$ can be immediately reduced by O^{2-} available at the SDC/MC interface, dissociating into two CO_3^{2-} to migrate to 3PBs on the permeate surface, where much faster CO_3^{2-} deionization reaction (2-26) takes place. The CO_2-transport enabling reactions via the ionic **Pathway-2** are summarized in the third column of Table 2.1.

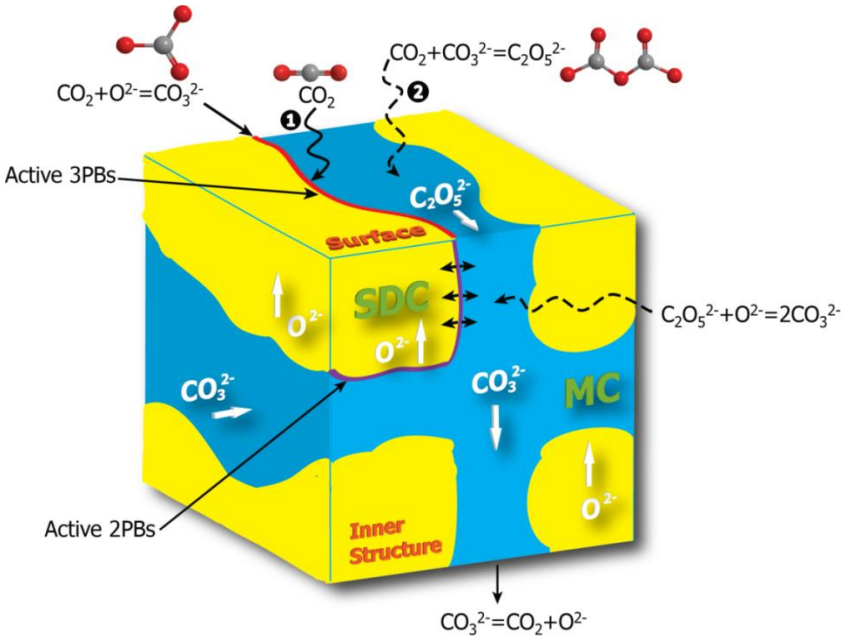

Figure 2.2 A 3D schematic illustrating electrochemical reaction occurring at 3PBs to 2PBs in dual-phase MOCC membranes; SDC=Sm_2O_3-doped CeO_2; MC=molten carbonate

Table 2.1 Two parallel ionic pathways proposed for the CO_2 transport through MOCC membranes

	Pathway 1	**Pathway 2**
	via 3PBs at CO_2 / MC / SDC	**via 2PBs at** CO_2 / MC **and** SDC / MC
Feed side	$CO_2 + O^{2-}_{(SDC)} = CO^{2-}_{3(MC)}$ (2-24)	$CO_2 + CO^{2-}_{3(MC)} = C_2O^{2-}_{5(MC)}$ (2-28)
In bulk	$CO^{2-}_{3(MC)}(\text{feed}) = CO^{2-}_{3(MC)}(\text{permeate})$ (2-25)	$C_2O^{2-}_{5(MC)} + O^{2-}_{(SDC)} = 2CO^{2-}_{3(MC)}$ $CO^{2-}_{3(MC)}(\text{feed}) = CO^{2-}_{3(MC)}(\text{permeate})$ (2-29)
Permeate side	$CO^{2-}_{3(MC)} = CO_2 + O^{2-}_{(SDC)}$ (2-26)	$CO^{2-}_{3(MC)} = CO_2 + O^{2-}_{(SDC)}$ (2-30)
Overall reaction	CO_2 (feed) = CO_2 (permeate) (2-27)	CO_2 (feed) = CO_2 (permeate) (2-31)
Gas product	CO_2	CO_2

2.3.2 Mechanism for charge transport in MECC membranes

Similar to MOCC membranes, two parallel charge transport pathways are also proposed in Fig. 2-3. The **Pathway-1** represents conventional route for CO_3^{2-} and e^- transport via 3PBs. A parallel route to **Pathway-1** proposed as a new CO_2 transport pathway is labeled as **Pathway-2** in Figure 2-3 and Table 2.2. This pathway involves the formations of two intermediate surface species, $C_2O_5^{2-}$ and CO_4^{2-} at 2PBs (MC/CO_2-O_2) (eq. (2-40)-(2-41)), and their subsequent reduction by electrons into CO_3^{2-} at 2PBs (Ag/MC) (eq. (2-42)). The formed CO_3^{2-} is then transported toward and deionized at the permeate side, releasing CO_2 and O_2 to the surrounding environment and electrons to charge-balance CO_3^{2-} flux (eq. (2-45)).

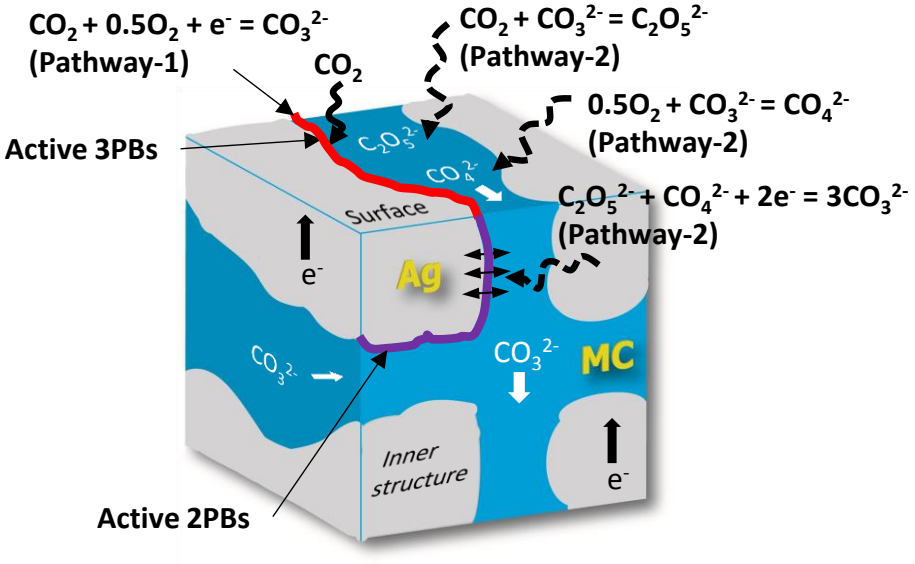

Figure 2.3 Schematic illustrations of two parallel ionic/electronic pathways for electrochemical CO_2 transport taking place at 3PBs and 2PBs in MECC exposed to CO_2-O_2 atmosphere.

Table 2.2 Two parallel pathways proposed for the CO_2 transport through the MECC membranes

	Pathway 1	**Pathway 2**
Feed side	**via 3PBs at** $CO_2 - O_2 / MC / Ag$	**via 2PBs at** $CO_2 - O_2 / MC$ **and** Ag / MC
	Peroxide mechanism: $O_2 + 2e^-_{(Ag)} = O^{2-}_{2(MC)}$ (2-32) $O^{2-}_{2(MC)} + 2CO_2 + 2e^- = 2CO^{2-}_3$ (2-33)	$CO_2 + CO^{2-}_{3(MC)} = C_2O^{2-}_{5(MC)}$ (2-40) $0.5O_2 + CO^{2-}_{3(MC)} = CO^{2-}_{4(MC)}$ (2-41)
	Superoxide mechanism: $O_2 + e^-_{(Ag)} = O^-_{2(MC)}$ (2-34) $O^-_{2(MC)} + 2CO_2 + 3e^- = 2CO^{2-}_3$ (2-35)	$C_2O^{2-}_{5(MC)} + CO^{2-}_{4(MC)} + 2e^-_{(Ag)} = 3CO^{2-}_{3(MC)}$ (2-42)
Overall at feed side	$CO_2 + 0.5O_2 + 2e^-_{(Ag)} = CO^{2-}_{3(MC)}$ (2-36)	$CO_2 + 0.5O_2 + 2e^-_{(Ag)} = CO^{2-}_{3(MC)}$ (2-43)
In bulk	$CO^{2-}_{3(MC)}(feed) = CO^{2-}_{3(MC)}(permeate)$ (2-37)	$CO^{2-}_{3(MC)}(feed) = CO^{2-}_{3(MC)}(permeate)$ (2-44)
Overall Permeate side	$CO^{2-}_{3(MC)} = CO_2 + 0.5O_2 + 2e^-_{(Ag)}$ (2-38)	$CO^{2-}_{3(MC)} = CO_2 + 0.5O_2 + 2e^-_{(Ag)}$ (2-45)
Overall reaction	CO_2 (feed) = CO_2 (permeate) (2-39)	CO_2 (feed) = CO_2 (permeate) (2-46)

One of the focuses of this thesis is to verify experimentally the existence of intermediate species hypothesized using in situ Raman spectroscopy.

CHAPTER 3 SYNTHESIS AND CHARACTERIZATION OF MEMBRANES

3.1 SYNTHESIS OF POROUS MATRIX AND MEBRANES

Porous ceramics have a variety of applications in filters, sorbents, catalysis, gas separation membranes and fuel cells.[73-77] By virtually controlling the composition and microstructure (porosity, pore morphology, pore size and distribution), a porous ceramic can exhibit very different physical and chemical properties to meet specific applications. To produce these application-specific porous ceramics, adequate fabrication techniques are required.[76] A traditional way to make a porous ceramic is to mix the functional ceramic material with a fugitive pore former. When such a mixture is fired at elevated temperatures, the pore former is thermally decomposed into vapor phase, leaving behind pores within the original structure.[74] This method, however, often results in non-uniform pore distribution due to uncontrollable grain growth in the course of sintering. In addition, uneven shrinkage caused by inhomogeneous distribution of pore formers lead to dimensional instability. It is particularly detrimental to multilayer ceramic structures such as solid oxide fuel cells when thin-films of large aspect ratio are present. To meet the increasing demand for porous ceramics with a controllable microstructure, numerous

novel processes have been developed,[76] representatives of which include methods of replica[78], direct foaming[79] and sacrificial template[80]. The "replica" technique is a relatively easy and well-established process; but it often produces products with degrading mechanical strength due to the cracked struts formed during the process. Since the pore sizes in the final ceramic parts are not directly related to the "pore formers" in the simple manner, the "direct foaming" method has the difficulty to control porosity.[76] In contrast, the sacrificial template method involves sintering the matrix material with the sacrificial material at elevated temperatures and chemically removing the sacrificial material at low temperature (often at room temperature). Since the creation of porosity takes place at low temperature, the dimensional stability of the matrix can be ensured. More importantly, the porosity can be controlled by the volume fraction of the sacrificial template while the pore size and distribution can be tailored by the grain size and distribution of the sacrificial template material. However, one important requirement for this method is that the functional matrix material does not react with the sacrificial material at elevated temperatures.

While the porosity of the matrix can be easily controlled by the volume fraction of the sacrificial material, a homogeneous distribution of pores as well as pore size also requires special preparation methods. Wet-chemical routes are well known to produce fine particles with homogenous distribution. Methods such as modified Pechini[80],

combustion[81], hydrothermal[82], and co-precipitation[83] are the most commonly practiced ones.

In this thesis work, we chose to use "sacrificial template" method to fabricate the porous solid-oxide structure because this method can create a tight and homogeneous distribution of micro/nano-pores across the solid-oxide matrix. NiO is the sacrificial template material of choice to go along with SDC because NiO has a very limited solubility in and confined chemical reactivity with SDC even at elevated temperatures. This allows the use of high temperatures to attain a stronger NiO-SDC ceramic. After the reduction of NiO in reducing atmospheres, the resultant elemental Ni in the composite is then removed by dissolving into a HNO_3, leaving behind a porous SDC matrix for subsequent melt-infiltration of carbonates. The SDC-NiO composite were prepared by a modified Pechini method and co-precipitation method as the precursor of the final porous matrix. The overall synthesis steps are schematically illustrated in Fig. 3.1.

Conventional mixing-pressing technique is the method widely used to make dual phase membrane.[84-86] The critical challenge to this conventional fabrication route is the low sintering temperature limited by the low melting temperature of the carbonate phase (usually around 300-500 ^{o}C). Low sintering temperature leads to low strength and inferior oxide-ion or electron conductivities as a result of insufficient grain growth and coalescence, significantly limiting the potential applications of MOCCs and MECCs in CO_2 separations. A simple but effective approach to solve this issue is to prefabricate a

stronger porous matrix at high temperatures, into which a molten carbonate phase is subsequently infiltrated. The sacrificial template method adopted in this research can produce a strong porous oxide matrix.

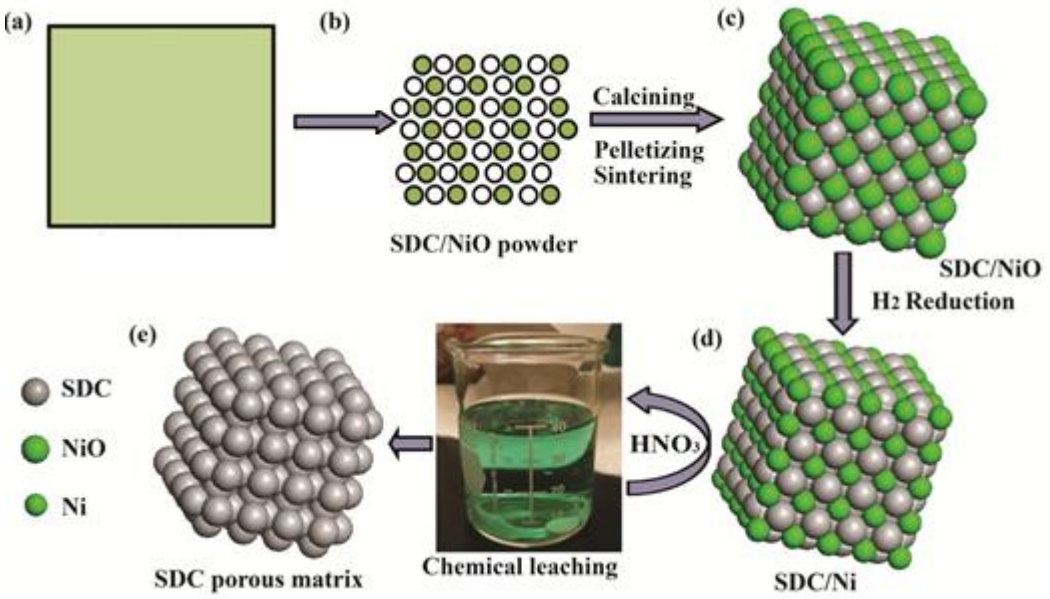

Figure 3.1 Schematic illustrating individual steps for making porous SDC solid oxide matrix via sacrificial template method. (a) SDC-NiO composite; (b) SDC-NiO composite powder; (c) sintered SDC-NiO composite ceramic; (d) reduced SDC-Ni ceramic; (e) SDC porous ceramic after chemical removal of elemental Ni phase.

Anderson *et. al* [87] used $La_{0.6}Sr_{0.4}Co_{0.8}Fe_{0.2}O_3$ (LSCF) as the porous solid phase. The LSCF powder was synthesized via the liquid citrate method. The LSCF powder was ground and mixed with 1mL of 3 wt% polyvinyl alcohol (PVA) solution to bind the powder during pressing. The green disks were sintered in air for 24 h at 900 and 1200 ˚C

to produce porous LSCF support. Sintered LSCF supports were infiltrated with molten carbonate to obtain the dual-phase membrane. Lithium (Li), sodium (Na), and potassium (K) carbonates were mixed in a 42.5/32.5/25 mole percent ratio and heated to 520 °C in a vertical tube furnace. The supports were preheated above the molten carbonate mixture in the furnace for 20 min. The support was then lowered into the molten carbonate, such that only the bottom of the support was in contact with the molten liquid. The support was held in place for 20 min to allow for the molten carbonate to soak into the membrane via capillary action. The membrane was slowly removed from the furnace to avoid thermal shock of the support. After the dual-phase membrane had cooled, residual carbonates were removed from the contact surface with Struers 500-grit SiC polishing paper by lightly polishing the contact surface between the support and molten carbonate.

S. J. Chung *et. al.* [72] used similar procedures to fabricate the MECC membrane, which stainless-steel as solid phase and Li-Na-K carbonate salt as liquid phase. Porous stainless-steel disks 1.58 mm in thickness and 19.5 mm in diameter (from Mott Co.) were used as the support (metal phase). These metal supports were made of spherical stainless steel particles. The carbonate mixture was prepared by mixing and grinding Li_2CO_3, Na_2CO_3, and K_2CO_3 powders. The ground Li/Na/K carbonate mixture was transferred to a crucible and was heated in a furnace at temperatures over the eutectic melting point (397 ℃). A metal support disk was preheated in the same furnace, and then the bottom surface of the preheated metal support disk was brought into contact with the molten

carbonate. Dual-phase membranes were prepared at dip-coating temperatures of 500 and 600 ℃. Support preheating time and the contact time with the molten carbonate were varied to identify the optimum synthesis conditions. The amount of molten carbonate infiltrated into the metal support was estimated by measuring the weight of the support before and after dip coating, with respect to the contact time. As-synthesized dual-phase membranes were kept in a desiccator to avoid undesired reaction with water vapor.

Unlike the first two studies, in-situ method had been used by Wade *et. al.* [69] to fabricate MOCC dual-phase membrane. Porous ceramic discs were fabricated from YSZ and CGO using tape casting techniques. The pore structure was created by adding graphite flake (325 mesh, Alfa Aesar) to the tape casting slurry, which acted as a pore forming agent upon burn out in the sintering process. The porous discs were attached to alumina support tubes using a ceramic sealant (Ceramabond, Aremco). Once the porous solid oxide ceramic was sealed to an alumina support tube, a measured amount of a carbonate mixture was placed evenly on top of the feed surface of the membrane. Excess carbonate was added to ensure the majority of the pores were filled, including any porous voids in the ceramic seal. The molar ratio of carbonate to oxide was roughly 2:1 in all membrane experiments. The powder melted and filled the pore volume of the solid oxide disk upon heating up within the testing reactor.

In this research, the prefabricated sacrificial template derived porous SDC matrix and Ag matrix were infiltrated with molten carbonate to form dense MOCC and MECC membranes.

3.1.1 Synthesis of porous oxide matrix

The $Ce_{0.8}Sm_{0.2}O_{1.9}$ and NiO composite powders were first prepared by a modified Pechini method. Starting materials $Ce(NO_3)_3\ 6H_2O$ (Alfa Aesar, 99.95%),, $Sm(NO_3)_3\ 6H_2O$ (Alfa Aesar, 99%) and $Ni(NO_3)_2\ 6H_2O$ (Alfa Aesar, 99.5%) in a stoichimetric ratio were first mixed with deionized water, followed by heating/stirring on a hot plate at 80°C. Once the nitrates are completely dissolved, citric acid monohydrate was then added into it. After approximately 10 minutes, the ethylene glycol was added as chelating and complexing agents. The solution was kept stirring/heating until it became a resin-like substance and eventually ignited into ashes. The dried ashes were subsequently calcined at 1000°C for 4 h in air to ensure the formation of SDC/NiO composite and removal of any organic residues. It was then pressed into ϕ13 mm pellets with a thickness of 1 mm and sintered at 1500°C in air for 10 h. The well-sintered pellets were then reduced in pure H_2 at 800°C for 10 h to convert nickel oxide to nickel metal. The Ni in the reduced composite was removed by dissolving it into a 2.2M HNO_3 at 80°C for 24 h.

The $Ce_{0.8}Sm_{0.2}O_{1.9}$ and NiO composite powders have also been synthesized by a co-precipitation method. Starting materials $Ce(NO_3)_3\ 6H_2O$ (Alfa Aesar, 99.95%),

$Ni(NO_3)_2\ 6H_2O$ (Alfa Aesar, 99%), and $Sm(NO_3)_3\ 6H_2O$ (Alfa Aesar, 99.5%) in a stiochiometric ratio were mixed with deionized water as the precursors and $(NH_4)_2CO_3$ (Fisher Scientific, 95%) as the mineralizer. The volume fractions of NiO in SDC-NiO composite varied among 35, 40 and 50 vol%. After precipitation, the co-precipitate was first washed with DI-water for multiple times, and then filtered, dried and subsequently calcined at 600^{o}C for 4h in air to ensure the formation of SDC-NiO composite and removal of any residues. The obtained powders were then pressed into ϕ13 mm pellets in a thickness of 1 mm, followed by sintering at 1200-1550^{o}C in air for 10 h. The following steps were the same as modified Pechini method.

3.1.2 Synthesis of porous metal matrix

The porous silver matrix was first fabricated by intimately mixing silver powders (99.9%, Alfa Asear) with microcrystalline methylcellulose pore former (Alfa Asear) in a ratio of 30:70 (vol%). The power was then ball-milled (Mix/Mill 8000M, Spex Sample Prep) and uniaxially pressed at 200 MPa into pellets using a static mold press (18 mm in diameter), followed by firing at 650^{o}C for 2h. After that, the sample was placed in a vacuum impregnation chamber (CitoVac, Struers). Al_2O_3 colloidal solutions (0.05 μm, Alfa Asear) with 5 and 10 wt% concentrations were infiltrated into the porous silver scaffold for one time under a vacuum condition.

Similarly, silver porous matrix was also synthesized by using carbon black as the pore former. The volume fractions of pore former in the composite was 40 vol% to yield corresponding porosity. Then, Al_2O_3 colloidal solutions (0.05 μm, Alfa Asear) with 5 wt% concentrations was infiltrated into the porous silver scaffold for one time under a vacuum condition.

3.1.3 Synthesis of MOCC and MECC membranes

The dual-phase MOCC membrane was fabricated by filling pores in the SDC matrix with a carbonate melt consisting of Li_2CO_3 and Na_2CO_3 (52:48 in mol %). The procedure can be briefly described as follows. The porous SDC pellet suspended in a silver wire is slowly immersed into the carbonate melt at 700^{o}C. After soaking for 4-hour, the temperature is ramped down. At 500^{o}C, a temperature slightly higher than solidification temperature for MC (~495^{o}C), the MC-saturated SDC is then slowly pulled out from the MC melt and hung above the melt as the furnace is continually cooled down to 100^{o}C when the sample is removed. The dual-phase membrane is finally polished using sandpaper with ethanol alcohol as a media to remove the residual molten carbonate on the surfaces, followed by gas tightness check using a homemade leakage check device before it is assembled into a permeation cell.

The dual-phase MECC membrane was fabricated by filling pores in the Ag matrix with a eutectic mixture of Li_2CO_3 (≥99%, Alfa Asear) and K_2CO_3 (≥99%, Alfa Asear) in 62:38 (mol%). The procedure can be briefly described as follows. The porous Ag pellet suspended in a silver wire is slowly immersed into the carbonate melt at 650^{o}C. After soaking for 2-hour, the temperature is ramped down. At 500^{o}C, the MC-saturated Ag is then slowly pulled out from the MC melt and hung above the melt as the furnace is continually cooled down to 100^{o}C when the sample is removed. The fabricated membrane is finally polished using ethanol alcohol as media to remove the residual molten carbonate.

3.2 CHARACTERIZATION TECHNIQUES FOR POUROUS MATRIX AND MEMBRANES

3.2.1 XRD

The phase composition of the fabricated porous matrices and membranes were examined by X-ray diffraction (XRD) by a X-ray diffractometer (Rigaku, Japan) equipped with graphite-monochromatized CuKa radiation (λ=1.5418 Å) using a scanning rate of 5^{o} min^{-1} in the 2θ range from 20 to 80^{o}. The obtained XRD patterns were then analyzed with JADE software to identify phases.

3.2.2 SEM/EDS and TEM

The microstructures of obtained porous oxide and metal matrices were examined by a field emission scanning electron microscopy (FESEM, Zeiss Ultra) equipped with an energy dispersive X-ray spectroscopy (EDS) analyzer. For nonconductive samples, a thin layer of Au was coated on the surface by a gold sputtering coater.

The morphology of synthesized powders was visualized by a transmission electron microscopy (TEM, Hitachi H-800, 200 kV).

3.2.3 Mercury porosimetry

The pore size distributions, median pore sizes and porosities of fabricated porous matrix were quantified by a mercury porosimetry (Autopore IV, Micromeritics) at pressures ranging from 0.5-30000 psi. Micromeritics' AutoPore characterizes a material's porosity by applying various levels of pressure to a sample immersed in mercury. The material's "porosity" includes the measurements of pore size, volume, distribution, density, and other porosity-related characteristics of a material. The mercury porosimetry analysis technique is based on the intrusion of mercury into a porous structure under stringently controlled pressures. Besides offering speed, accuracy, and a wide measurement range, sample properties such as pore size distributions, total pore volume, total pore surface area, median pore diameter, and sample densities can be calculated based on mercury porosimetry.

3.2.4 Particle size analysis

The particle sizes of synthesized composite powders were analyzed by a particle size analyzer (Horiba, LA950). The LA-950 is capable of measuring wet and dry samples in the range of 10 nanometers to 3 millimeters. The central idea in laser diffraction is that a particle will scatter light at an angle determined by that particle's size. Larger particles will scatter at small angles and smaller particles scatter at wide angles. A collection of particles will produce a pattern of scattered light defined by intensity and angle that can be transformed into a particle size distribution result.

3.2.5 Three-dimensional Micro-XCT and Nano-XCT

To obtain a 3-D image of the internal structure, a Micro X-ray computed tomography (XCT-400, Xradia insight in 3D) was first employed. The MicroXCT-400 is an all-purpose, high resolution, non-destructive 3D X-ray imaging system uniquely designed for imaging various sample sizes as well as imaging during in-situ experiments. Specially designed high resolution lens detectors allow for high resolution and high contrast imaging of larger samples. Additional travel of the source and detector stages, and input baffles for the spacious enclosure allow for unprecedented ability to image samples during in-situ experiments involving test fixtures. The benefits of the 3D X-ray imaging system are non-destructive 3D imaging, imaging during in-situ experiments,

heavy load sample stage and extended source and detector stage travel, high spatial resolution down to 1 μm and 0.56 μm pixel size and Continuous operation through automated multiple point tomography and repetitive scanning.

However, due to a limited resolution (>1 μm), Micro-XCT is unable to discern pore sizes of the fabricated SDC porous matrix that contains a median pore size less than 1 μm. A new synchrotron based Nano-XCT technique was employed to reveal the 3D microstructure of a SDC porous matrix at nanometer scale.

The nano-XCT is a revolutionary x-ray microscope system offering unprecedented resolution and 3D imaging for non-destructive, non-invasive investigations in a wide range of industrial and scientific applications at nanometer scale. The key features of Nano-XCT are non-destructive 3D imaging at sub-50 nm resolution using Fresnel zone plates as objective lenses, variable field of view and magnification and fast and artifact- free detect localization. The sample suitable for use in synchrotron nanotomography measurements was first created using a FIB-SEM milling technique[88]. A cylinder approximately 10 microns in diameter and 20 microns in length was extracted from the bulk material and attached vertically on the tip of a pin. The sample was then mounted in the transmission x-ray microscope at the National Synchrotron Light Source beamline X8C. X-ray nanotomography was performed at 8365 eV by rotating the sample between -90^{o} and $+90^{o}$ in 0.5^{o} increments, which produces

images with a resolution of roughly 47 nm. Images of the sample were taken at each angular position with an exposure time of 10 seconds per image and a spatial resolution of 30 nm as dictated by the zone plate characteristics[89]. The tomography data set was reconstructed using a filtered back projection algorithm to obtain a 3D volumetric representation of the sample. The important microstructural features such as phase volume fraction, phase size distribution (PSD), contiguity, and interfacial contact area per unit volume can be obtained from the analysis.

3.2.6 Electrochemical impedance spectroscopy

The effective ionic conductivity of the fabricated membrane was measured by electrochemical impedance spectroscopy with a Zahner IM6 Electrochemical Workstation (ZAHNER-Electrik GmbH & Co., Kronach, Germany). Equipped with a programmable potentiostat, a pair of high precision amplifiers for current and potential, a flexible frequency generator/analyzer and four slots for additional input and output modules the IM6 is designed for nearly all measurement situations in the electrochemistry lab. Specially designed for spectrum analysis in the electrochemical field, the modular hardware concept of the IM6 allows you to configure the IM6 for applications far beyond impedance spectroscopy. With the appropriate hardware and software modules you can perform nearly all important data acquisition and analysis

techniques which are required by electrochemical applications. The measurements for this thesis work were performed with a symmetrical cell configuration and Ag electrode in the frequency range of 0.1 Hz-8 MHz, 10 mV AC stimulus voltage and in a temperature range of 400-650^{o}C and atmospheres of flowing air, CO_2/O_2 (1:1) and H_2+3%H_2O, respectively.

3.3 PROPERTIES OF POROUS MATRIX AND MEMBRANES

3.3.1 Properties of porous oxide matrix

The phase evolution of an SDC/NiO ceramic (65:35 in vol%, SDC65NiO35) with the starting material synthesized by modified Pechini method with varying processing conditions is shown in Fig. 3.2 (a). First, there are no detectable new phases formed between SDC and NiO after sintering at 1500^{o}C for 10 hours. Second, the reduction of NiO to Ni (SDC65Ni35) and removal of Ni from the SDC structure (SDC65) are also evident from comparisons with the standard peaks of NiO and Ni (JCPDS 65-5745 and 04-0850). In particular, no nickel can be found in the final SDC matrix. In agreement with XRD analysis, visual inspection of the sample at these three distinct stages also indicates a change in color from green (Fig. 3.2 (b)) to gray (Fig. 3.2 (c)) and to white (Fig. 3.2 (d)). Other compositions, e.g., 60:40 and 70:30 in vol%, of the SDC/NiO ceramics also show similar results of XRD patterns and color changes.

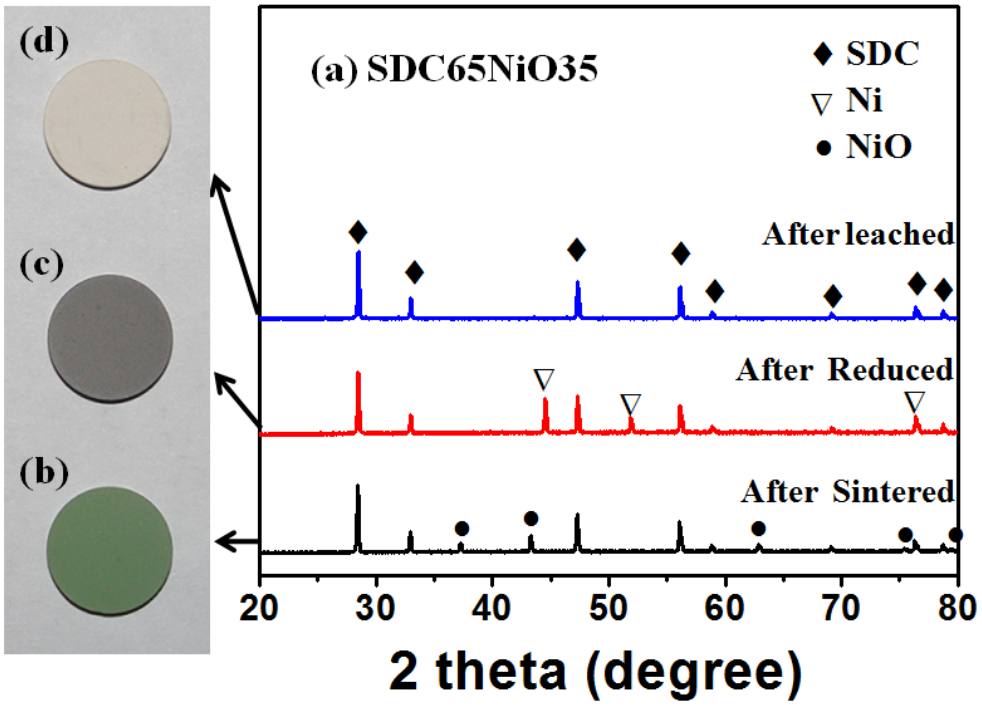

Figure 3.2 (a) Evolution of X-ray diffraction patterns of SDC/NiO ceramic (SDC65NiO35) with processing conditions. Physical appearances of SDC65NiO35 (b) after sintering; (c) after reduction; (d) after leaching in HNO_3.

Microstructural analysis of the SDC porous matrix series were carried out with FESEM. Figure 3.3 (a) shows the fracture morphology of an SDC65 porous matrix. The average pore size is 2-3 μm. The porosity is 41.8% as measured by Archimedes' method. In order to take a close look into the detailed internal structure of the SDC matrix, a 3D X-ray computed tomography imaging technique was used. The results are shown in Fig. 3.3 (b), where the cube with sides having a dimension of 200 μm was selected. The 3D

X-ray tomography evidently confirms a uniform distribution of homogeneous micro-pores throughout the SDC matrix, even though the resolution needs further improvement.

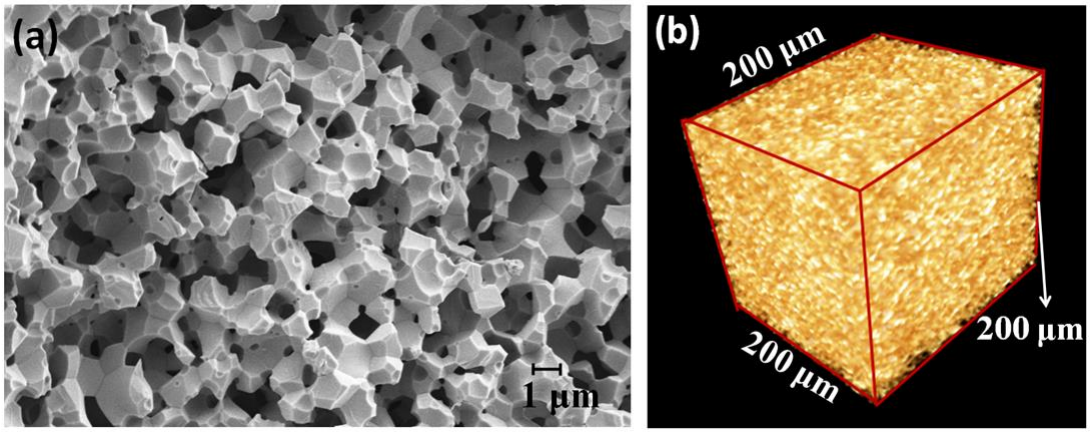

Figure 3.3 (a) cross sectional view of SDC65 porous structure by FESEM; (b) 3D X-ray computed tomographical view of SDC65 internal porous structure;

The XRD patterns of SDC60/NiO40 (40 vol% NiO) powder synthesized by co-precipitation method after calcining at 600^{o}C are shown in Fig. 3.4 (a), where only peaks relevant to NiO and SDC are present, suggesting that no chemical reaction took place between SDC and NiO during the low-temperature calcination. Particle size analysis of the same powder, Fig. 3.4 (b), reveals a bimodal distribution, one at ~0.1 µm and another at ~3 µm.

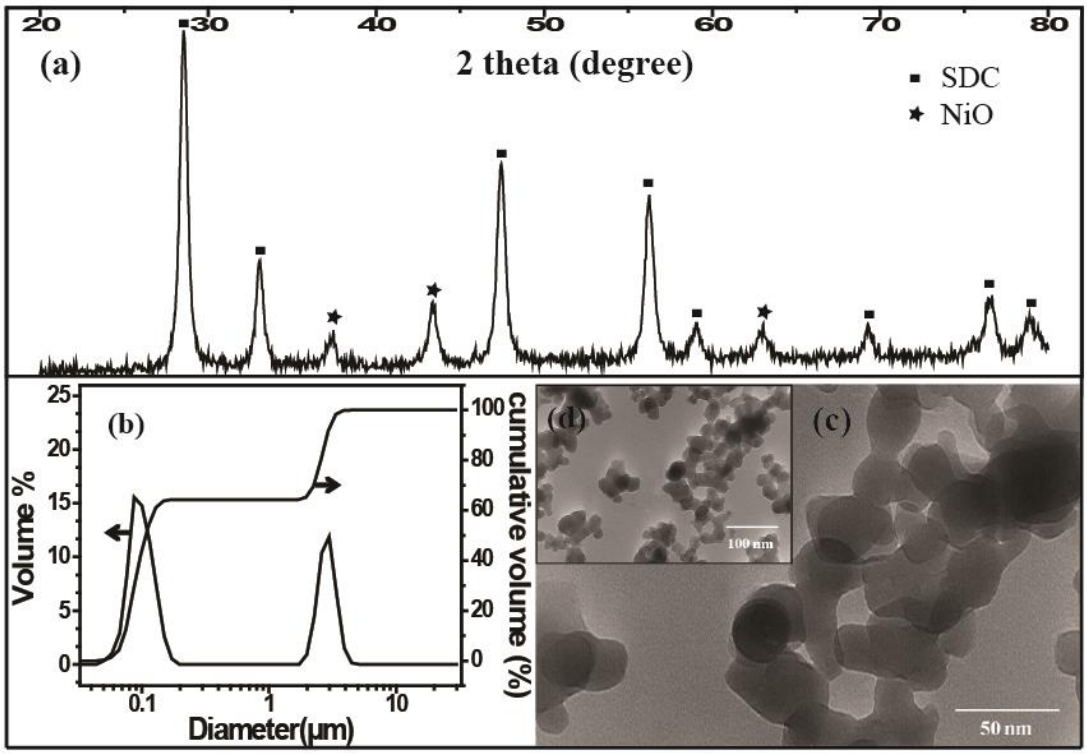

Figure 3.4 (a) XRD pattern, (b) pore size distribution, (c) higher magnification and (d) lower magnification of TEM images of SDC60/NiO40 calcined at 600^{o}C for 4 h.

This is likely caused by the agglomeration formed during calcination and inefficient particle dispersion during particle size analysis. However, the high and low magnifications of TEM images, Fig. 3.4 (c) and (d), indicate spherical and uniform nano-sized grains of SDC-NiO composite. The 10-nm individual grain size is much smaller than that measured by particle size analysis and prepared by Pechini method.[77]

The chemical homogeneity of the formed composite is examined by EDX elemental mapping. The surface morphology of a SDC50/NiO50 (50 vol% NiO) sintered at 1400^{o}C for 10 h is shown in Fig. 3.5 (a). It exhibits a dense and uniform microstructure

with grain size < 1 μm. The corresponding Ce-, Sm- and Ni-elemental mappings are shown in Fig. 3.5 (b), (c) and (d), respectively, revealing a very uniform elemental distribution. This study further confirms the high degree of compositional homogeneity created by molecular level mixing enabled by the co-precipitation method.

The phase evolution of SDC50/NiO50 ceramic in the course of synthesis is shown in Fig. 3.6 (a), (b) and (c). After sintering at 1400^{o}C for 10 h, Fig. 3.6 (a), XRD patterns indicate the composite containing independent phases of SDC (JCPDS 97-002-8792) and NiO (JCPDS 65-5745). The reduction of NiO to Ni in the SDC matrix, Fig. 3.6 (b), is also evident from comparisons with the standard peaks of Ni (JCPDS 04-0850).

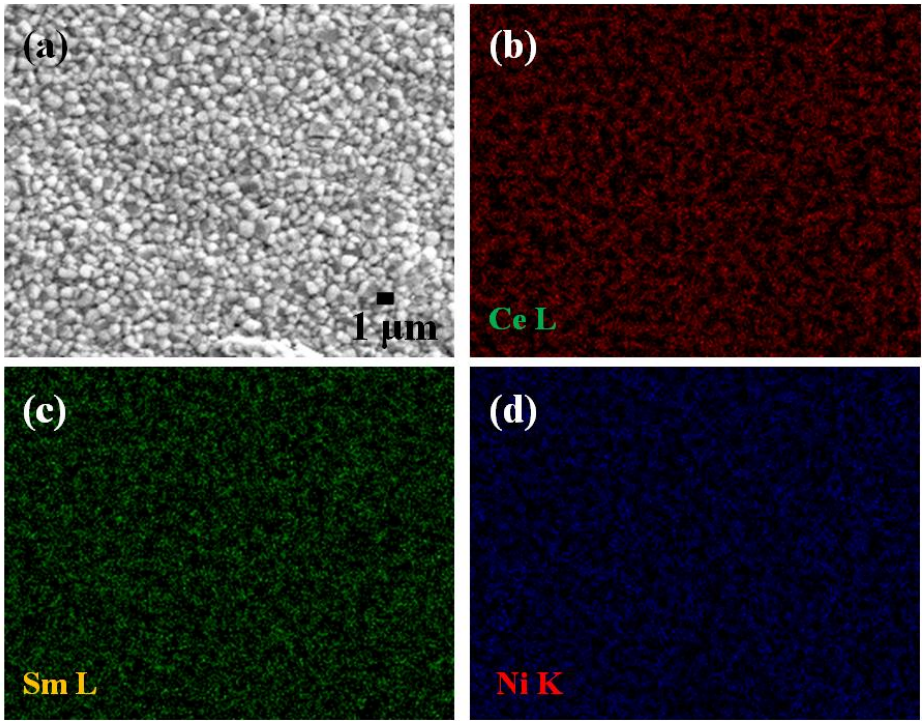

Figure 3.5 (a) FESEM image of SDC50/NiO50 sintered at 1400^{o}C for 10 h; the corresponding elemental mappings: (b) Ce ; (c) Sm; (d) Ni.

Finally, Fig. 3.6 (c) shows that no nickel peak can be found in the matrix after chemical leaching. Based on the limitation of XRD technique, the content of nickel should be lower than 2 wt%. In agreement with XRD results, visual inspection of the samples at these three distinct stages also indicates changes in color from dark green (Fig. 3.6 (d), SDC+NiO) to dark grey (Fig. 3.6 (e), SDC+Ni) and finally yellowish white (Fig. 3.6 (f), SDC).

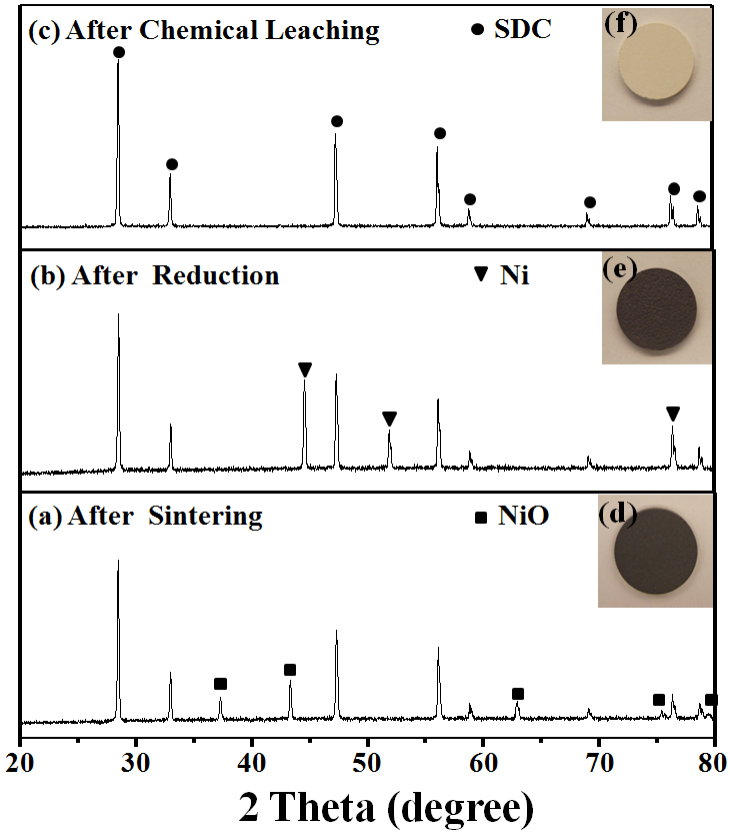

Figure 3.6 Evolution of X-ray diffraction patterns of SDC50/NiO50 with processing steps. Physical appearances of SDC50/NiO50: (c) after sintering; (d) after reduction; (e) after chemical leaching.

The internal microstructure of a 1500^{o}C-sintered SDC50/NiO50 porous matrix revealed by a 3-D Micro X-ray computed tomography imaging technique is shown in Fig. 3.7 (a); a representative cube size of 200 μm^3 is selected. The overall microstructural feature is sponge-like, porous, homogeneous and interconnected. The interconnectivity is clearly resulted from chemical removal of interconnected network of the sacrificial phase NiO. However, more detail of the microstructure is limited by the 1-μm resolution of the X-ray microscope. In order to reveal more detailed internal structure, a traditional 2-D FESEM is used. The low and high magnifications of FESEM images of the SDC50/NiO50 sample are shown in Fig. 3.7 (b) and (c). Again, a very homogeneous and submicron-scale porous structure is observed. The median pore size of 901 nm of a mono-distribution and the porosity of 50.2%, both measured by mercury porosimetry as shown in Fig. 3.7 (d), have an excellent agreement with the microstructural features revealed by the FESEM and the designed porosity.

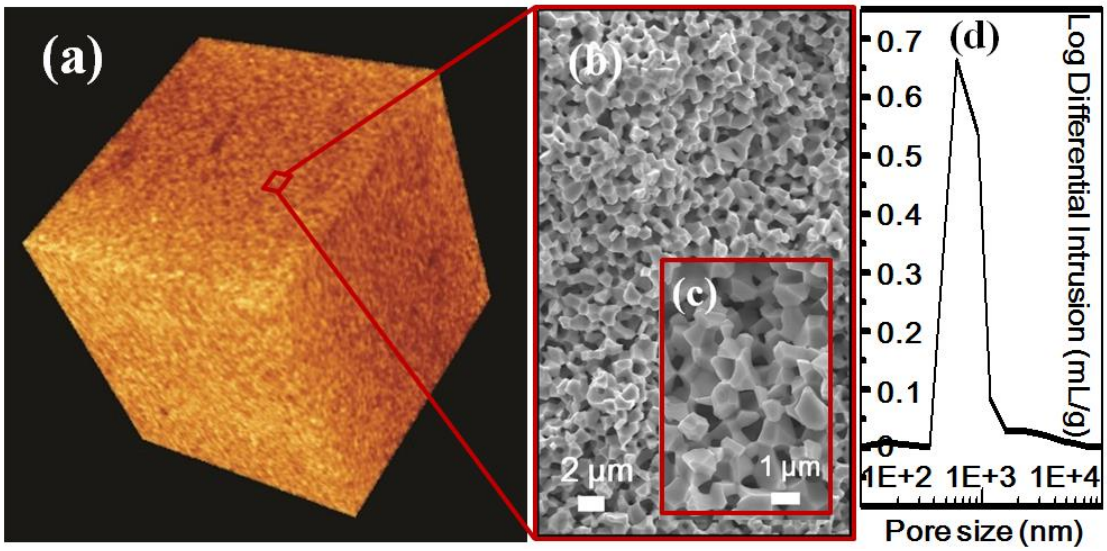

Figure 3.7 (a) 3-D X-ray tomographical view and 2-D cross-sectional views at (b) low magnification and (c) high magnification; (d) Pore size distribution of SDC50/NiO50 porous matrix sintered at 1500^{o}C.

To have a more clear view of the structure, a 3-D nano-computed tomography instead of 3-D micro-computed tomography is employed to measure the microstructure. The reconstructed 3D microstructure of a SDC50 (50vol%SDC) porous matrix shown in Fig. 3.8 (a) can be generally characterized as a sponge-like framework with excellent intra- and interconnectivity between SDC matrix and pores.

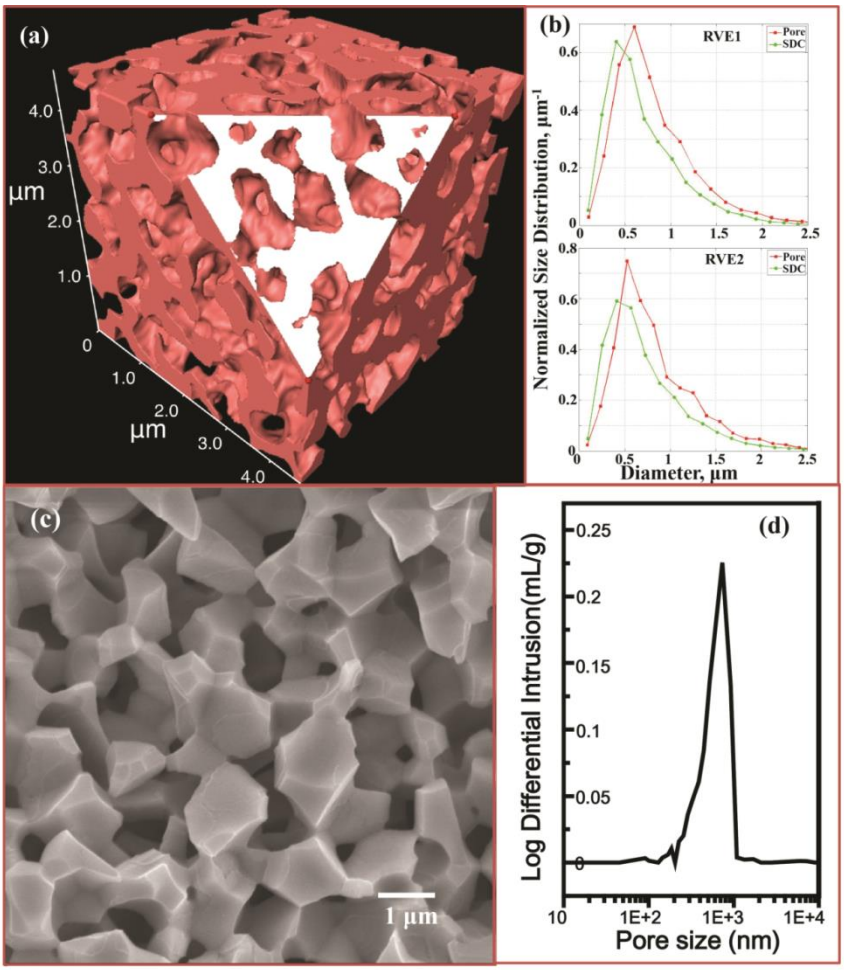

Figure 3.8 Microstructural features of a SDC50 (50 vol% SDC). (a) Reconstructed 3D microstructure from x-ray tomography; (b) phase size distributions of two RVEs (Representative Volume Elements); (c) SEM 2D microstructure; (d) pore size distribution by mercury porosimetry.

Table 3.1Summary of microstructural parameters of SDC50 (50 vol% SDC) obtained from x-ray nano-CT, FESEM and mercury porosimetry.

	X-ray Nano-CT	FESEM	Mercury Porosimetry
Volume Fraction			
Pore	54%	--	50.2%
SDC	46%	--	49.8%
Median Pore Size (nm)	505	550	600
Contiguity			
Pore	100%	--	--
SDC	100%	--	--
Interface Contact Area per Unit Volume ($\mu m^2/\mu m^3$)	5.75	--	--

Subsequent image analysis of two Representative Volume Elements (RVEs) reveals a 100% contiguity of each individual phase and 54% pore volume fraction. The median pore size and interfacial contact area per unit volume are 505 nm and 5.7 $\mu m^2/\mu m^3$, respectively, see Fig. 3.8 (b). These microstructural parameters suggest a highly and efficiently interconnected porous network. Regular FESEM image shown in Fig. 3.8 (c) illustrates a similar microstructural feature in 2D fashion: uniform distributions of pore and SDC. The pore size is estimated to be ~550 nm, fairly close to that determined from x-ray nano-CT. The mercury porosimetry data shown in Fig. 3.8 (d) indicate a median

pore size of 600 nm and the porosity of 50.2%, both of them are also in reasonably good agreement with those obtained from 3D x-ray nano-CT and 2D SEM. A summary of all the microstructural features of the porous SDC obtained by the three techniques is given in Table 3.1.

The pore size of porous SDC matrix is expected to increase with sintering temperature as the grain size of sacrificial material NiO increases with sintering temperature[90-93]. This assertion is evidently confirmed by Fig. 3.9 (a)-(h), where the cross-sectional views of an SDC65/NiO35 sample sintered from 1200 to 1550^{o}C in a step of 50^{o}C show incremental increase in pore size with increasing temperature. The red line shown in Fig. 3.9 (a)-(h) represents the measured (using mercury porosimetry) median pore size of the sample sintered at the lowest temperature 1200^{o}C. With increasing sintering temperature, the distribution peaks systematically shift away from the red line towards larger pore size. The quantified pore size is further plotted as a function of sintering temperature in Fig. 3.9.

The median pore-size of SDC65/NiO35 porous matrix increases from 87.4 to 368.5 nm from 1200 to 1550^{o}C, consistent with the FESEM results. Since the pores are uniformly distributed across the sample, all the FESEM images were taken from randomly selected areas of the samples, and as such, these are representative of the overall porous SDC matrix. The uniformity of pores is also supported by the mono (or

nearly mono-)-mode distribution of pore size revealed by mercury porosimetry and shown in Fig. 3.9 (A)-(H).

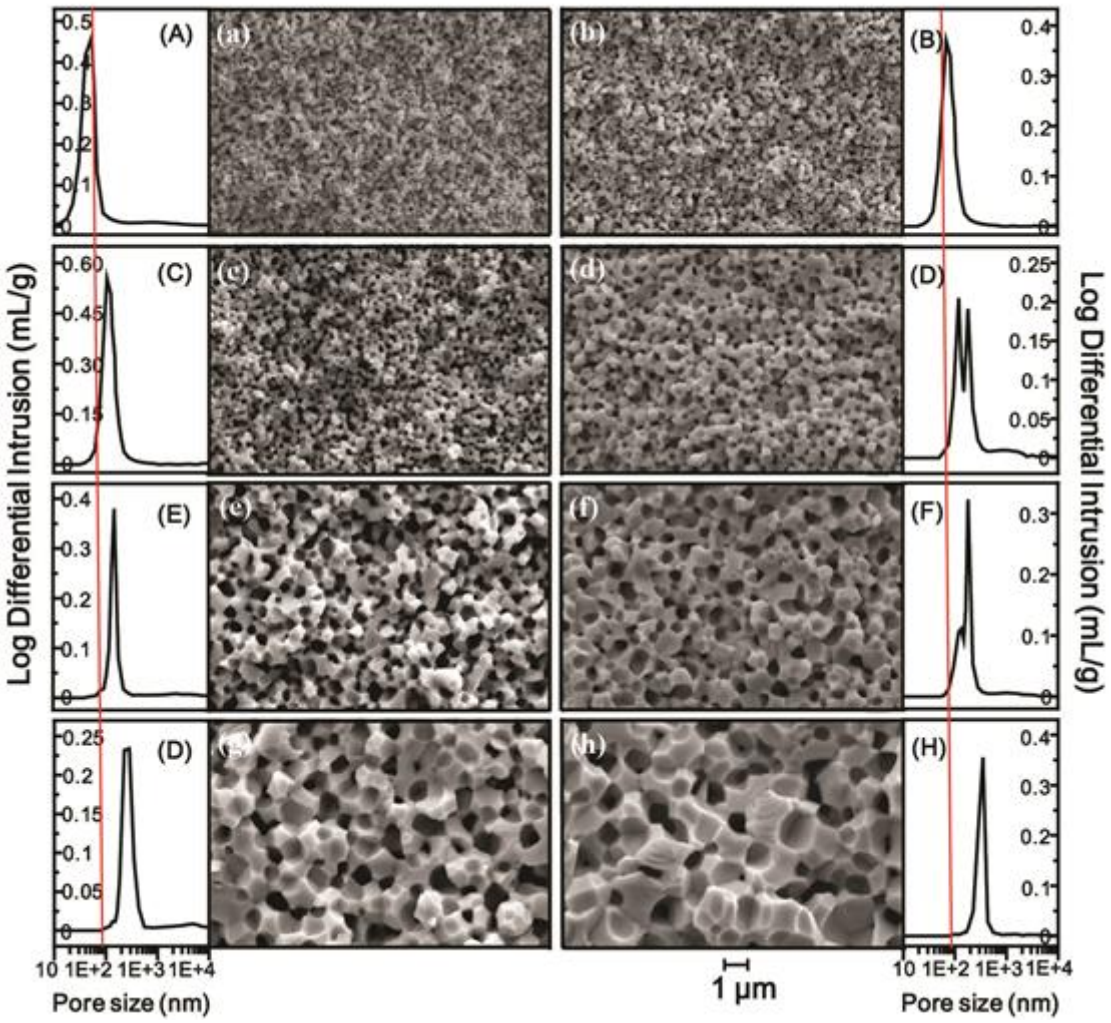

Figure 3.9 FESEM images of SDC65/NiO35 ceramics sintered at (a)1200; (b)1250; (c) 1300; (d)1350; (e)1400; (f)1450; (g)1500; and (h) 1550^{o}C. Plots of pore size distribution are shown in (A)-(H), corresponding to (a)-(h).

Theoretically speaking, the porosity of a porous material made from a sacrificial template method is controlled largely by the volume fraction of the sacrificial material.

This premise has been indirectly verified in Fig. 3.10, where the porosity is shown to be insensitive to the sintering temperature. To directly confirm the hypothesis, the measured porosities of three samples all sintered at 1400^{o}C are plotted as a function of NiO volume fraction in Fig. 3.11. The best-fit line almost passes the origin (the slope of the fitted line is 1.053), suggesting that the porosity is directly related to the volume fraction of NiO.

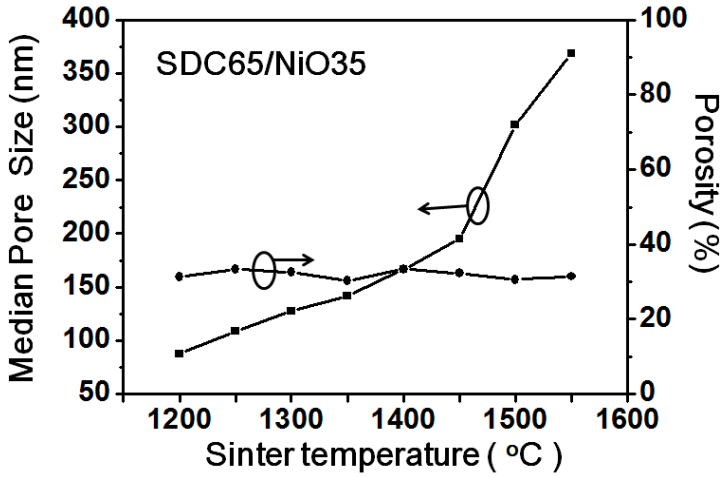

Figure 3.10 Plot of porosity and median pore size of SDC65/NiO35 as a function of sintering temperature.

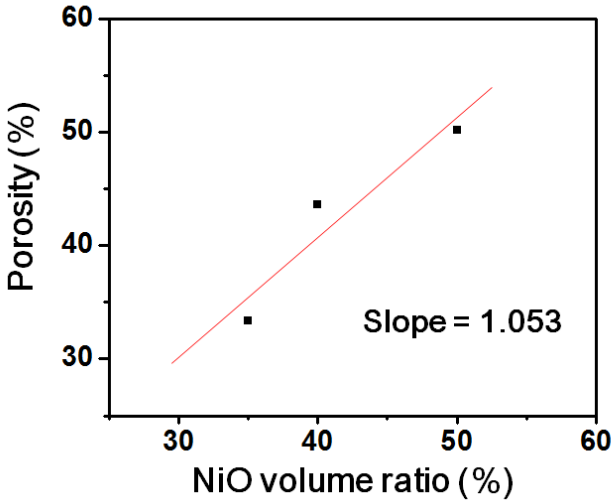

Figure 3.11 Plot of porosity as a function of volume fraction of NiO in SDC-NiO composite sintered at 1400°C.

So far, we have demonstrated that with NiO as the sacrificial material, the pore size and porosity of the resultant porous SDC matrix can be, respectively, controlled by sintering temperature and volume fraction of NiO. Figure 3.12 shows a composite layout of FESEM images, illustrating the temperature and compositional effects. At the horizontal direction, the effect of temperature on microstructure is shown for SDC60/NiO40. The pore size increases from 135.1 nm at 1300°C, to 259.8 nm at 1400°C and 723.2 nm at 1500°C. On the other hand, the porosity remains relatively flat with temperature: 43.5% for 1300°C, 43.6% for 1400°C and 43.9 % for 1500°C. At the vertical direction, the compositional effect on microstructure is shown for a given temperature

1400°C. In this case, the porosity increases from 32% for 35 vol%NiO, 43% for 40% vol%NiO and 50% for 50 vol%NiO while the pore size also increases from 167 nm for 35 vol%NiO, 260 nm for 40% vol%NiO and 629 nm for 50 vol%NiO. For a specific application where particular porosity and pore size are required, a porous ceramic matrix can then be readily fabricated based on the mapped processing conditions presented in this study.

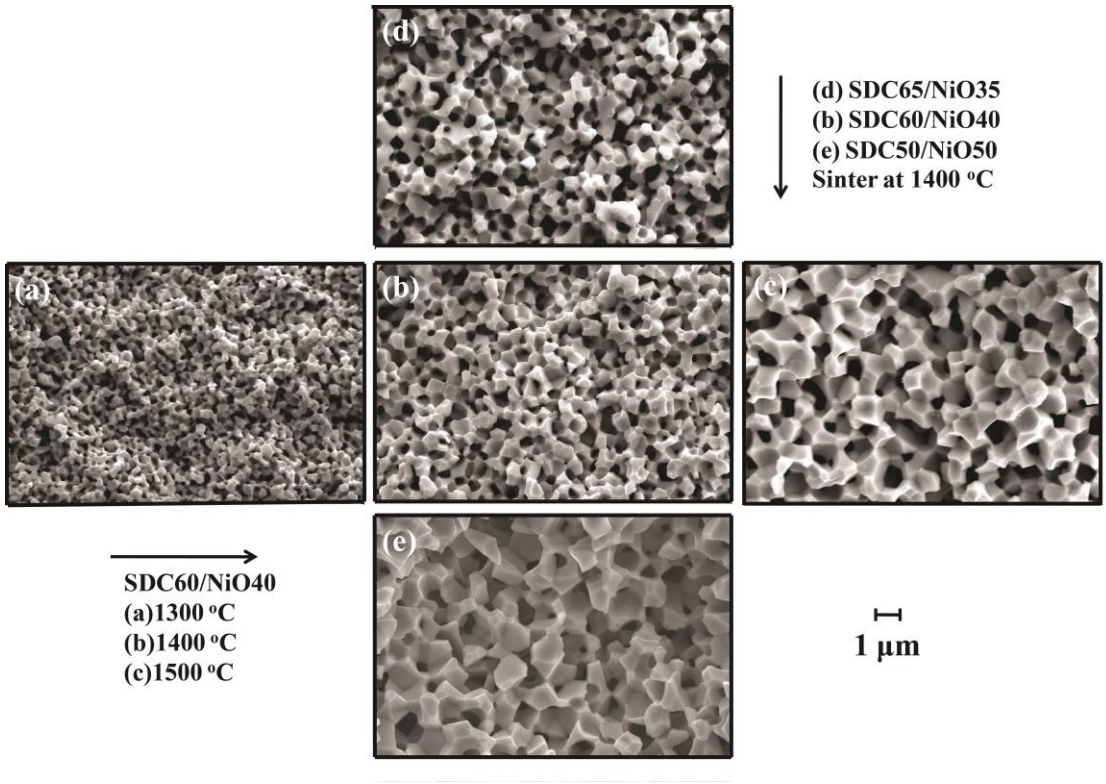

Figure 3.12 Microstructures of fabricated porous SDC ceramics at various conditions. (a)1300°C, (b)1400°C, (c)1500°C of sample SDC60NiO40; (d) SDC65, (b) SDC60, (e) SDC50, all sintered at 1400°C.

3.3.2 Properties of metal matrix

The microstructures of the fractures from a porous silver matrix fabricated by silver and microcrystalline methylcellulose are shown in Fig.3.13 (b). It is evident that the matrix exhibits a porous structure with the pore size around 15-20 μm. The mercury porosimetry data shown in Fig. 3.13 (a) indicate a median pore size of 13.3 μm and the porosity of ~40%, both of which are in excellent agreement with those obtain from SEM. Fig. 3.13 (c) shows a porous silver matrix decorated by an Al_2O_3 layer. The morphology of the matrix is not affected by the Al_2O_3 coating, but the pore size decreases to ~10 μm. The EDS analysis shown in Fig. 3.13 (d) further confirms the presence of Al_2O_3 in the matrix.

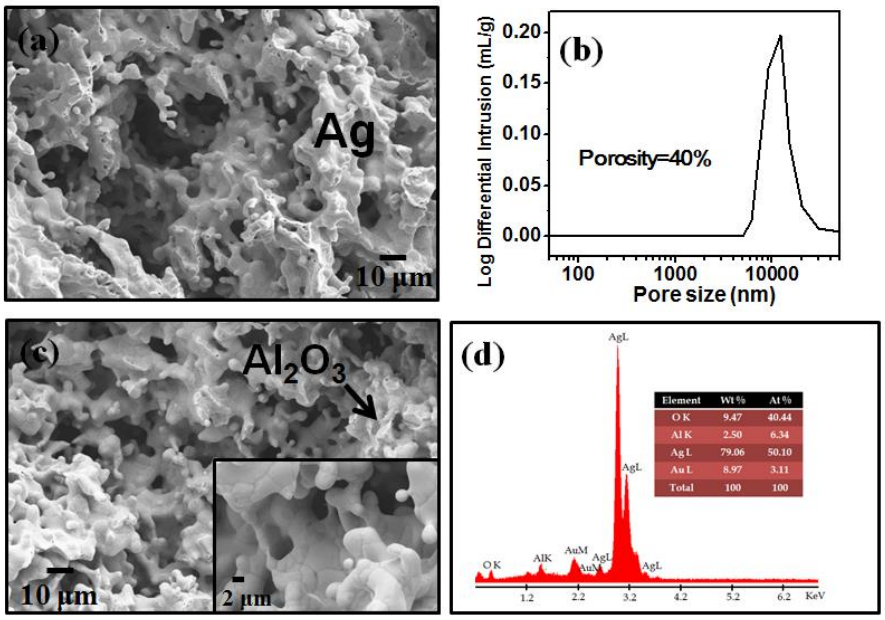

Figure 3.13 (a) Microstructure and (b) pore size distribution of a porous Ag matrix; (c) microstructure and (d) EDS compositions of a porous Ag matrix coated with 5% Al_2O_3 colloidal.

The microstructure of the fracture from a porous silver matrix fabricated by silver and carbon black is shown in Fig.3.14. It is evident that the matrix exhibits a more uniformly distributed porous structure with the pore size around 10 μm.

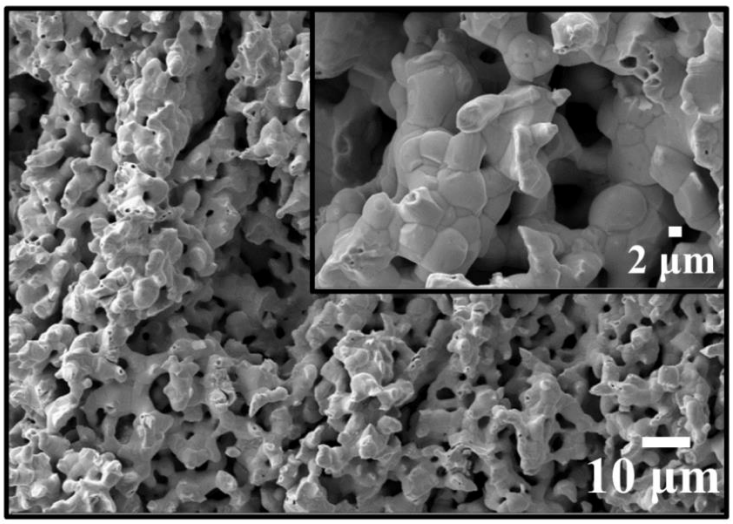

Figure 3.14 The microstructure of the fracture of a porous Ag matrix created by carbon black.

Fig.3.15 (a) shows 5% Al_2O_3 layer coated on the surface of a porous silver matrix. The morphology of the matrix is not affected by the Al_2O_3 coating, but the pore size decreases to ~8 μm. Fig. 3.15 (a) is revealed by EDS mapping in Fig. 3.15 (c)-(d); it suggests that Ag, Al_2O_3 and MC phases are still well distributed across the membrane.The EDS analysis shown in Fig.3.15 (b) further confirms the presence of Al_2O_3 in the matrix.

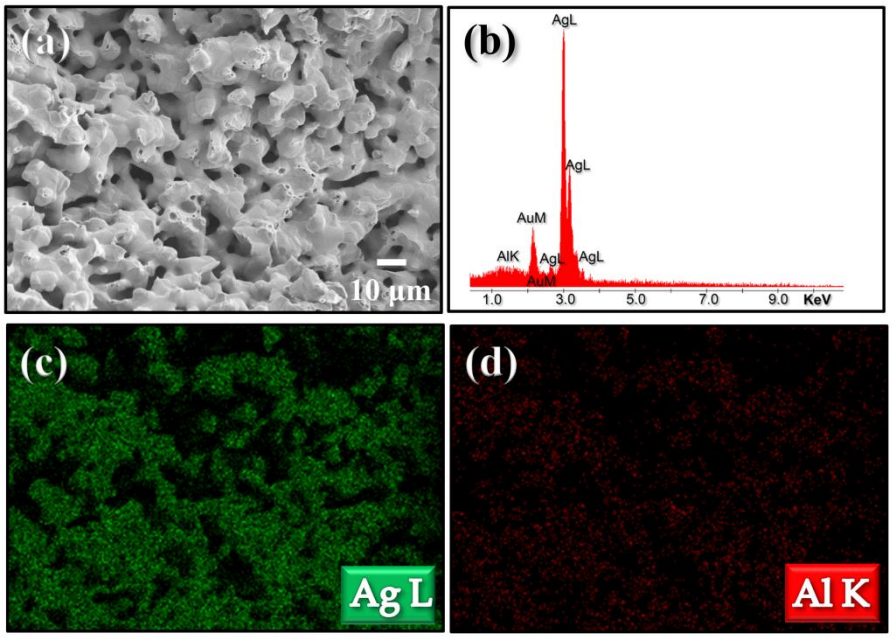

Figure 3.15 (a) Microstructure and (b) EDS compositions of a porous Ag matrix coated with 5% Al_2O_3 colloidal; Elemental distributions of Ag matrix with 5% Al_2O_3 colloidal (c) Ag mapping and(d) Al mapping.

3.3.3 Properties of MOCC and MECC membranes

A representative microstructure of the MOCC fracture, with the starting material synthesized by a modified Pechini method, is shown in Fig. 3.16 (a). The EDS analysis confirms that the darker and glassier areas are the Li-Na carbonate phase (Fig. 3.16 (b) (Li is too light to be detected by EDS) whereas the lighter areas belong to the SDC phase (Fig. 3.16 (c)). Overall, the MOCC exhibits a dense microstructure with the Li-Na carbonate phase filling out pores in the SDC porous matrix.

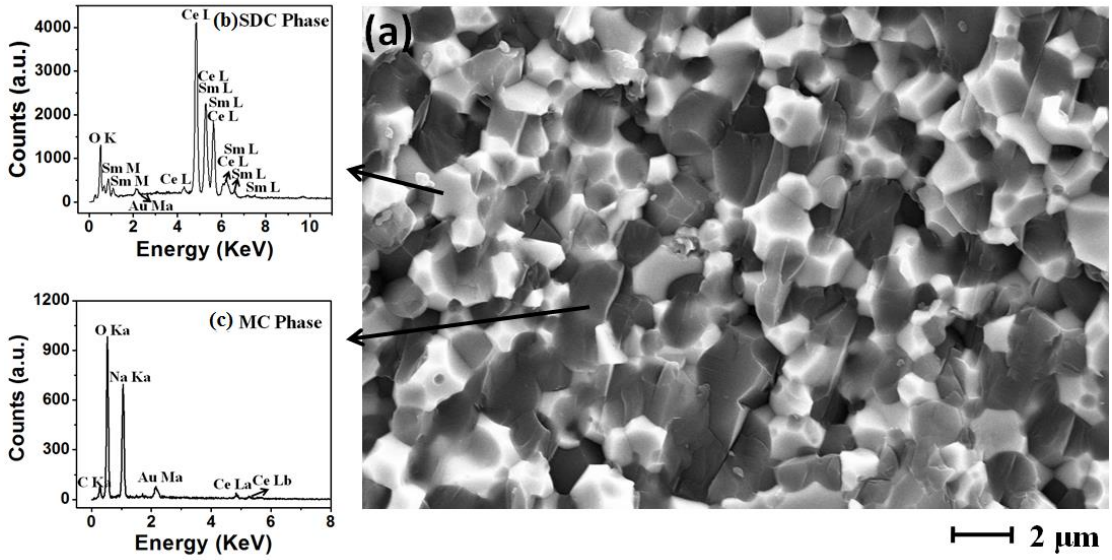

Figure 3.16 (a) Cross sectional view of an SDC65/MC fracture; EDS showing the MC phase (d) and the SDC phase (e) in the SDC65/MC MOCC.

The EIS impedance spectra of a MOCC (SDC65/MC) measured in air at three representative temperatures are shown in Fig. 3.17. The strong dependence on temperature of these spectra resembles closely those reported in our previous work[84]. At 400^{o}C, when the MOCC is in solid state, the observed partial semicircle at the high-frequency end is related to grains and grain-boundaries of the MOCC whereas the arc at the low-frequency end corresponds to the electrode process. At above 470^{o}C, the MC phase in the MOCC starts melting. This change in physical state brings about two effects: diminishes the dielectric response from grain and grain-boundary at high-frequency regime (completely replaced by the inductance impedance caused by the measuring leads) and sharply reduces the ionic resistance. When the MC phase is in a fully melted

state at 600°C, the spectrum is completed dominated by the high-frequency inductance impedance and low-frequency electrode impedance.

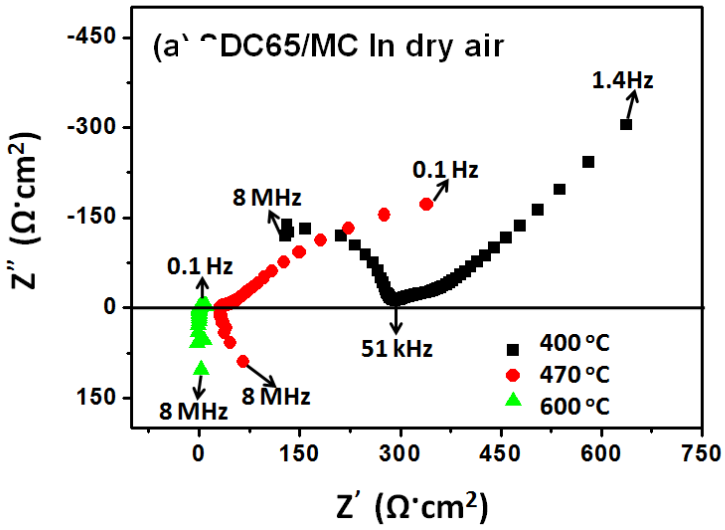

Figure 3.17 AC impedance spectra of SDC65/MC measured in dry air at three representative temperatures

The effect of MOCC compositions (SDC60, SDC65 and SDC70) on the effective ionic conductivity is shown in Figure 3.18 as a function of temperature. The sharp increase in conductivity with temperature from 470 to 490°C is unambiguously the result of the softening and the ultimate melting of the carbonate phase. Above 490°C, the ionic conductivity becomes less dependent on temperature and follows a trend very similar to that of the pure carbonate phase[84]. It is also evident from Figure 3.18 that the ionic conductivity increases with the porosity (NiO content in this case), therefore, the carbonate loading, particularly at above 490°C when the molten carbonate is the

prevailing conducting phase. The effective ionic conductivities at 650°C in air are 0.55, 0.43 and 0.35 S/cm, respectively, for SDC60, SDC65 and SDC70 compositions.

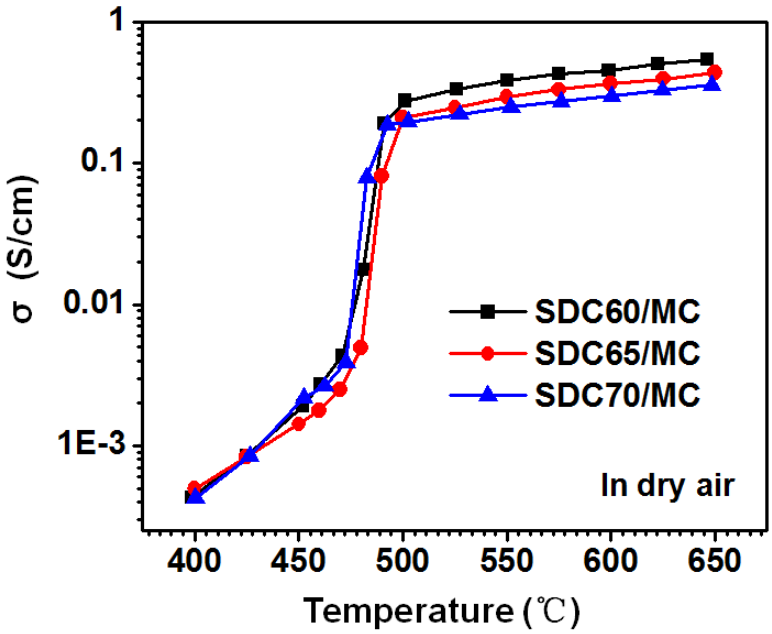

Figure 3.18 Plots of the effective ionic conductivity of SDC60/MC, SDC65/MC and SDC70/MC as a function of temperature in dry air.

Compared with conventional mixing-pressing method, the conductivity of the MOCC fabricated in this study is the highest because of the effective retaining of the carbonate phase by the well-structured micro-pores within the solid-oxide matrix. For example, the conductivity of a MOCC with SDC60 fabricated in this study is 0.46 S/cm at 600°C and 0.28 S/cm at 500°C, respectively. It was only 0.2 S/cm at 600°C for a

carbonate-ceria composite[94], 0.2 S/cm at 500°C for a SDC-carbonate[95] and 0.18 S/cm at 500°C for a $Ce_{0.8}Gd_{0.05}Y_{0.15}O_{1.9}$-carbonate[96].

The effect of atmospheres on the effective ionic conductivity of MOCC was also studied and the results are shown in Figure 3.19 as a function of temperature. The three atmospheres include dry air, CO_2/O_2 (1:1), 3%H_2O-H_2. In general, the MOCC shows comparable conductivities in dry air and CO_2/O_2, but a slightly higher conductivity in wet H_2 at T≥490°C. If the ionic conductivity at T≥490°C is mainly dominated by the molten carbonate as predicted by the EMPT theory[84], the slightly higher conductivity could be an indicative of proton conduction in the carbonate phase[97, 94]. On the other hand, the redox couple Ce^{4+}/Ce^{3+} associated electronic conduction could also contribute to the higher conductivity[26].

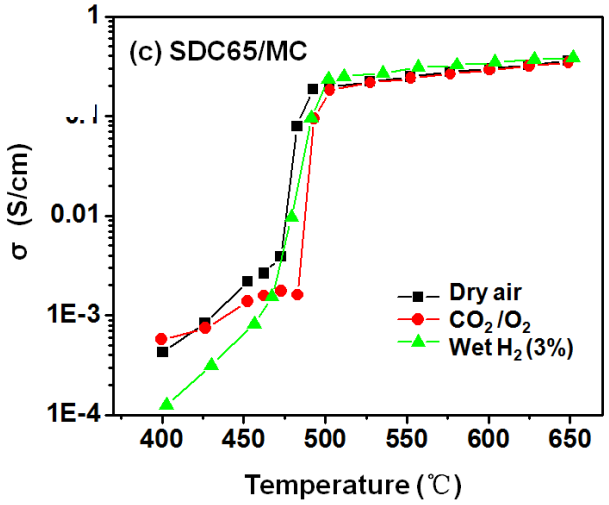

Figure 3.19 SDC65/MC as a function of temperature and atmospheres.

At below 450^{o}C, however, the conductivity appears to be less dependent on the atmosphere and ionic conduction of MOCC is dominated by the solid oxide phase. The differences observed at low Ts in different gas atmospheres is suspected the result of possible interaction between Ag electrode and carbonate in reducing atmospheres since a blackened Ag electrode was observed after the experiment.

The microstructure and chemical elemental distributions of the prepared MOCC membrane, with the starting material synthesized by co-precipitation method, are illustrated in Fig. 3.20. The glassy phase has shown in Fig. 3.20 (a) represents the MC whereas the grain-like lighter phase is the SDC phase. Evidently, the MOCC possesses a dense microstructure with the MC phase completely filling into the porous SDC matrix. Thus formed dense microstructure ensures that the permeated CO_2 is directly resulted from the concomitant transport of CO_3^{2-} and O^{2-}, not from CO_2 molecules. The chemical homogeneity indicated by EDX mapping of constituent elements in Fig. 3.20 (b)-(d) also supports that the SDC and MC phases are well distributed and homogeneously mixed across the membrane.

The microstructures of an Ag-MC MECC membrane based on Ag matrix using microcrystalline methylcellulose as fore former are shown in Fig.3.21 (a)-(d). It is evident that the microstructure is completely dense with the MC phase completely filling

in the pores of silver network, regardless of the Al_2O_3 coating. Both as-synthesized MECC membranes exhibit very similar microstructure before testing. Thus formed dense microstructure ensures that the permeated CO_2 is directly resulted from the ionic transport of CO_3^{2-}, not from CO_2 molecules.

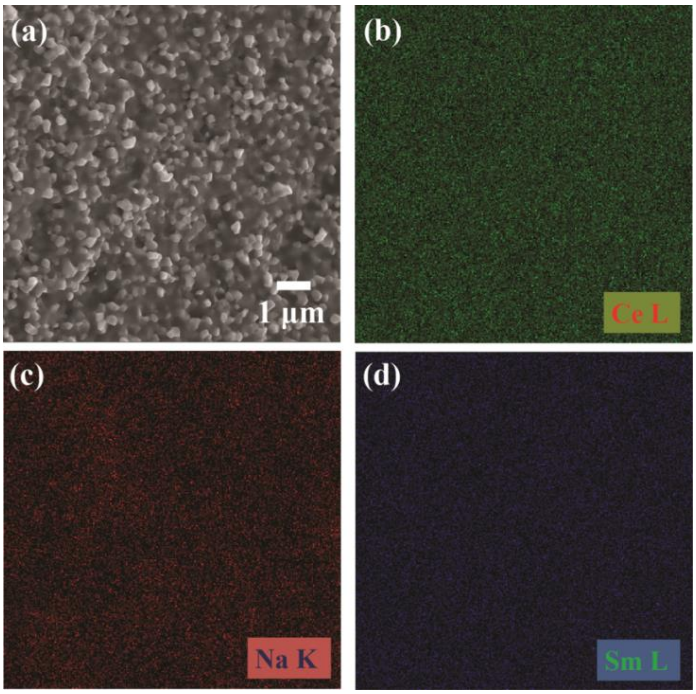

Figure 3.20 Microstructure and elemental distributions of a MOCC based on a SDC60 (60vol% SDC) porous matrix. (a) FESEM image; (b) Ce mapping; (c) Na mapping; (d) Sm mapping. Note: Li is too light to be detected by EDX.

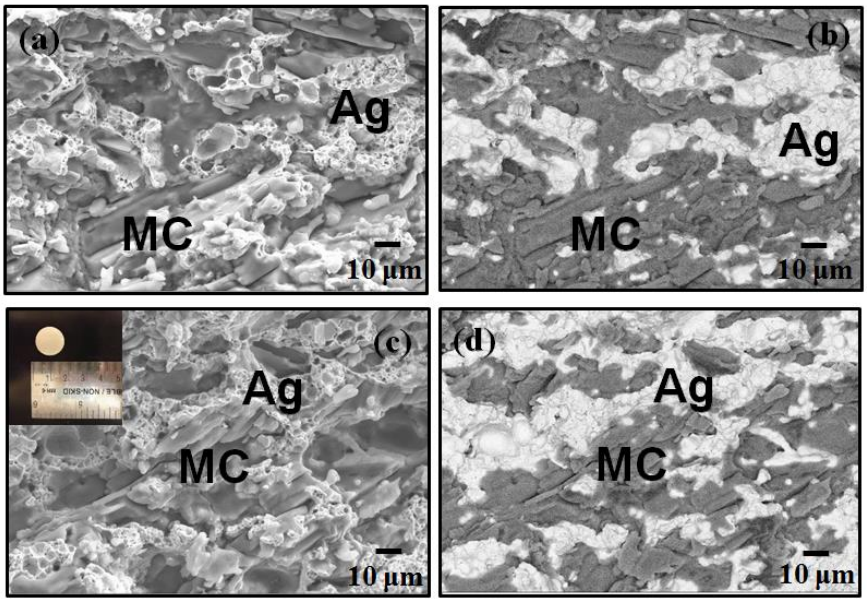

Figure 3.21 SEM, SEM-BSE images of (e) the pristine Ag-MC MECC and (f) the MECC coated with 5% Al_2O_3 colloidal

The microstructures of an Ag-MC MECC membrane based on Ag matrix using carbon black as the pore former and coated with 5% Al_2O_3 colloidal is shown in Fig.3.22 (a). The chemical homogeneity of this as-synthesized membrane is revealed by EDS mapping in Fig.3.22 (b)-(d). Clearly, Ag, Al_2O_3 and MC phases are well distributed across the membrane.

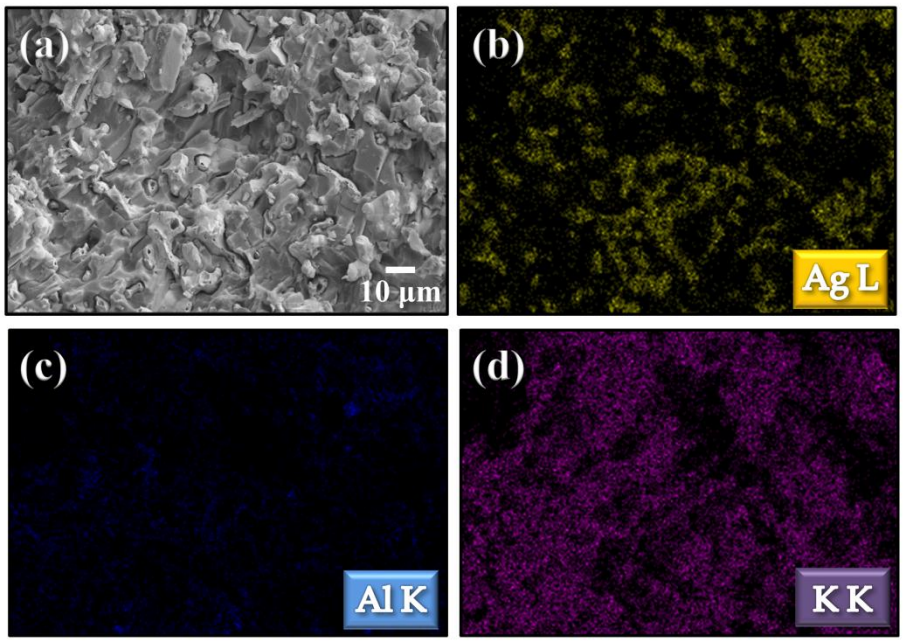

Figure 3.22 Microstructure and elemental distributions of Ag-MC MECC membrane decorated with Al_2O_3 coating (5% colloidal) before testing (a) SEM image; (b) Ag mapping; (c) Al mapping; and (d) K mapping. Note: Li is not detectable by EDS.

3.4 CONCLUSIONS

A strong porous SDC matrix for the first time has been fabricated by a "sacrificial template" technique. The porous SDC matrix presents a uniform distribution of homogeneous micro-pores as evidenced by both 2-D SEM imaging and 3-D X-ray computed tomography. The micro- and nano-sized SDC-NiO composite powders have been synthesized by the method of Pechini and co-precipitation. Thus synthesized intimately mixed powders were then used as the precursor for making homogeneously porous SDC matrix by high-temperature sintering, chemical reduction of NiO to Ni and chemical leaching of Ni. It has been explicitly demonstrated that the porosity can be

controlled by the volume fraction of the sacrificial phase NiO while the pore size can be affected by both the sintering temperature and volumetric fraction of NiO. The formed porous network is mechanically strong, homogeneous, interconnected and uniformly distributed across the entire sample. The MOCC supported by a more porous SDC matrix contains more MC phase, thus yielding higher ionic conductivity at above 490^{o}C. A MOCC (SDC60/MC) consisting of such prefabricated SDC matrix and melt-infiltrated Li-Na carbonate eutectic exhibits the highest effective ionic conductivity reported so far among the similar systems, reaching 0.55 and 0.46 S/cm at 650^{o}C and 600^{o}C, respectively. This superior electrical property strongly suggests MOCC as a promising ionic conductor for IT-SOFCs and CO_2-separation membranes.

A porous Ag matrix has been fabricated by solid state reaction method using microcrystalline methylcellulose and carbon black as a pore former. A layer of Al_2O_3 coating on the surface of silver porous network was employed as a wetting agent to enhance the retention ability of the porous matrix for MC phase. It has been shown that the matrix exhibits a porous structure with the pore size around 15-20 μm. The morphology of the matrix is not affected by the Al_2O_3 coating. After infiltration of MC, MECC membrane exhibits dense microstructure and uniform chemical distribution.

CHAPTER 4 CO_2 TRANSPORT PROPERTIES OF MOCC AND MECC MEMBRANES

4.1 BACKGROUND

The dual-phase separation membrane based on electrochemical reaction with CO_2-containing fuel and flue gases has been intensively studied by several groups in recent years. There are several different experimental procedures for testing CO_2 permeation flux. First, the membrane permeation reactor setup of Wade *et al.*[69] is shown in Fig. 4.1. An outer Inconel casing seals the alumina support tube from the outside atmosphere. The mixed feed stream contains CO_2 and He. The mixture was approximately a 1:1 composition with a total flow rate of 15 mL/min, controlled by Aalborg mass flow controllers (MFC). The admixture was used to determine selectivity and to detect any leaks that may arise in the system, for example, from pinholes or cracks in the membrane or ceramic seal. Heating of the reactor and the gases was controlled with a Tempco Power Console, and all heat up and cool down cycles were carried out at a rate of 2K min^{-1}.

Slightly different from the Wade's setup, Chung *et al.*[72] applied compressive seals to achieve gas tightness.. The permeation cell and a data acquisition system are shown in

Fig 4.2. A dual-phase membrane was sealed with gold-ring gaskets into the permeation cell. For high-temperature experiments, the permeation cell was heated in the furnace (Neytech, S-550) up to 450-750 ℃. The feed gas was introduced to the upstream membrane surface at 1 atm. Downstream pressure was reduced by a vacuum pump to <0.06 atm.

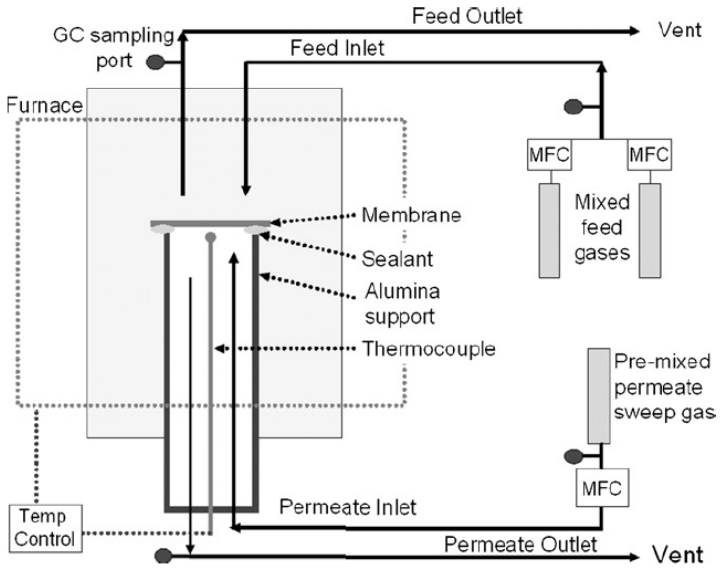

Figure 4.1 Schematic of the membrane permeation reactor by Wade *et al*[69]

After the downstream reservoir (1 L) was isolated from the vacuum pump, the pressure changes in the downstream with time were measured by a pressure sensor and data were collected by a computer data acquisition system. Permeation flux was obtained from the slope of pressure change versus time using a mass balance equation coupled with the equation of state for ideal gas. The third different testing method was used by

Anderson et al, [87] in which the membrane was sealed to an inner alumina tube by creating a paste composed of a mixture of ground, sintered LSCF powder (40 wt%), ground Pyrex beaker glass (50%), sodium aluminum oxide (Al_2O_3·Na_2O; 10%) and water (see Fig. 4.3). The system was completely sealed inside an alumna tube and heated at a rate of 1 ℃ min^{-1} to 900 ℃ to allow for the seal to soften and set. Gases were delivered to the up and downstream sides of the membrane by connecting mass flow controllers to 1 cm OD alumina tubes.

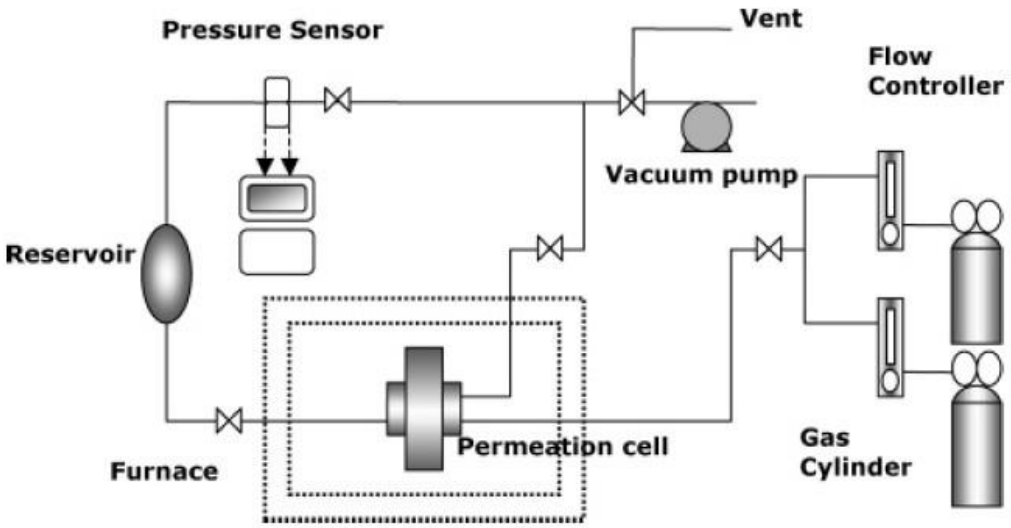

Figure 4.2 Schematic diagram of the permeation setup by Chung *et al*.[72]

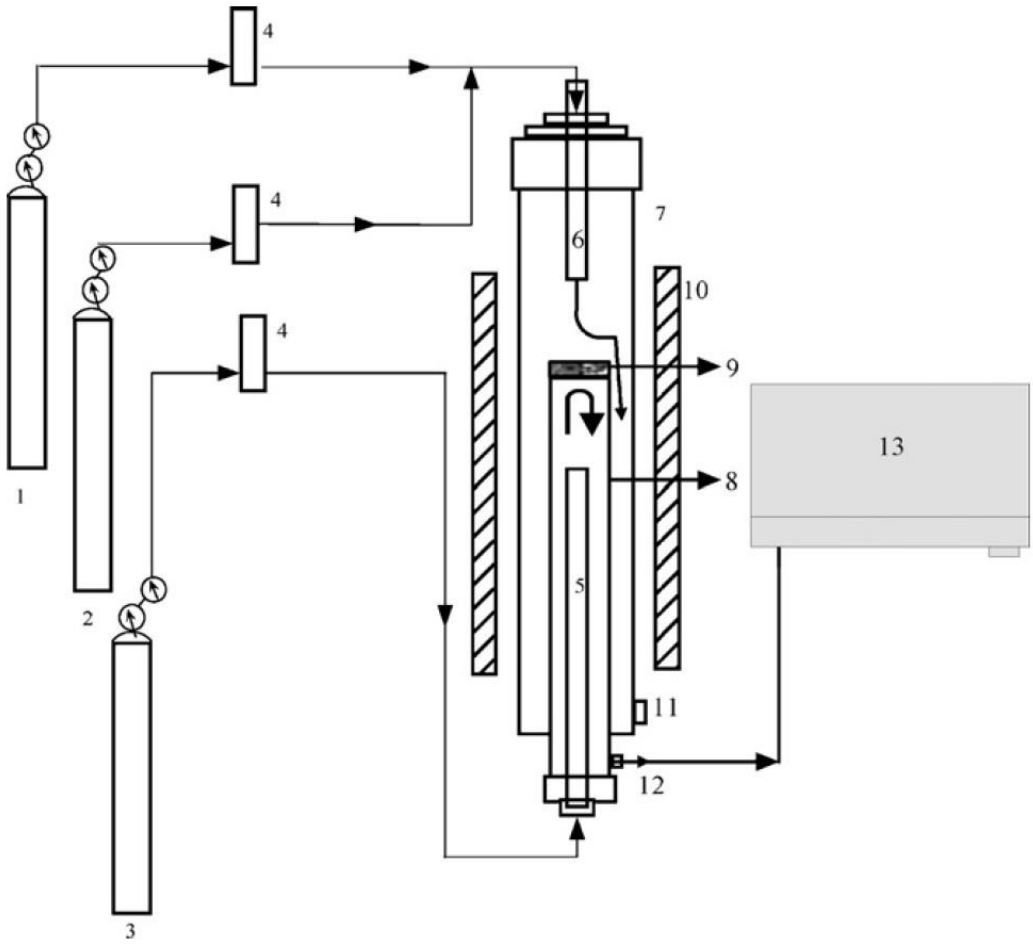

Figure 4.3 Schematic of the high temperature CO_2 permeation set up used by Anderson *et al*. (1) CO_2 cylinder, (2) Argon cylinder, (3) Helium cylinder, (4) Mass flow controllers, (5) Sweep/purge tube, (6) Feed tube, (7) Outer tube, (8) Inner tube, (9) Dual-phase membrane, (10) Furnace, (11) Permeate, (12) Retentate, and (13) GC.[87]

Each tube was placed about 3 cm away from the membrane on both sides. During heating and permeation, the feed side consisted of 50 mL min^{-1} each of CO_2 and Ar, while the sweep side was 100 mL min^{-1} of He. The flow rates were controlled by MKS Instruments mass flow controllers. All gases used were of industrial grade quality. Argon

was used to check for leaks in place of nitrogen in the event that experiments with O_2 were ever conducted in the future. This was done because N_2 and O_2 peaks can overlap in the GC. Argon was viewed as an acceptable substitute because it is inert and is similar in kinetic diameter to N_2, thus making it possible to use CO_2/Ar selectivities in the place of CO_2/N_2.

4.2 CHARACTERIZATIONS AND PROPERTIES OF THE MOCC DUAL-PHASE MEMBRANE

4.2.1 CO_2 flux measurement of MOCC

The CO_2 permeation characteristics of the synthesized MOCC were studied using a homemade permeation cell, the configuration of which is schematically shown in Fig. 4.4. The MOCC pellet membrane was first sealed to a supporting alumina tube using a modified sealant containing a mixture of ceramic cement (Ceramabond 552-VFG, Aremco Products) and a commercial glass powder (Schott glass GM31107). A second short alumina tube was then bonded to the top of the sample for the purpose of shielding the feed gas. The assembly was cured at room temperature for 1-4 hours and 93^{o}C for a minimum of 4 hours before further raising the temperature. The feed gas was typically a mixture of 5 ml min^{-1} H_2, 50 ml min^{-1} CO_2 and 50 ml min^{-1} N_2; N_2 was used as a tracer

gas for leak correction if any. A small amount of H_2 (4.8%) was added to the feed gas to lower the partial pressure of oxygen (Po_2) so as to promote O^{2-}-transport. For the study of H_2-effect on CO_2 flux density, a small incremental flow rate of H_2 was simply added without changing the flow rates of CO_2 and N_2. At the permeate side, high-purity helium (99.999%) at a flow rate of 50 mL min^{-1} was used as the sweeping gas, the composition of which was analyzed by an on-line micro-GC (Varian 490-GC, Varian). To ensure the data accuracy, the GC was calibrated with three standard gas compositions for each gas of interest (CO_2, O_2, and N_2). The final CO_2 flux density was calculated out from an averaged gas composition of a total of ten successive readings from the GC. For all gas flows, commercial mass flow controllers (Smart-Trak, 50 Series) specifically calibrated for the gas under use were employed to control the mass flow rates. The temperature of permeation cells was varied from 550 to 700^{o}C in an interval of 25^{o}C. At each temperature, 30 minutes were given to allow the cell to reach steady state before sampling. The concentration of N_2 in the sweeping gas was low (<0.05%) for all measurements, indicating that gas seals were not a concern for this study. This level of leakage was also estimated, introducing roughly 2% uncertainty in the final CO_2 flux density determination.

The flux densities of CO_2 and N_2 (leakage), were calculated using the following equations:

$$J_{N_2,leak} = \frac{c_{N_2}}{(1 - c_{CO_2} - c_{N_2})} \times \frac{Q}{S} \quad (4\text{-}1)$$

$$J_{CO_2,total} = \frac{c_{CO_2}}{(1 - c_{CO_2} - c_{N_2})} \times \frac{Q}{S} \quad (4\text{-}2)$$

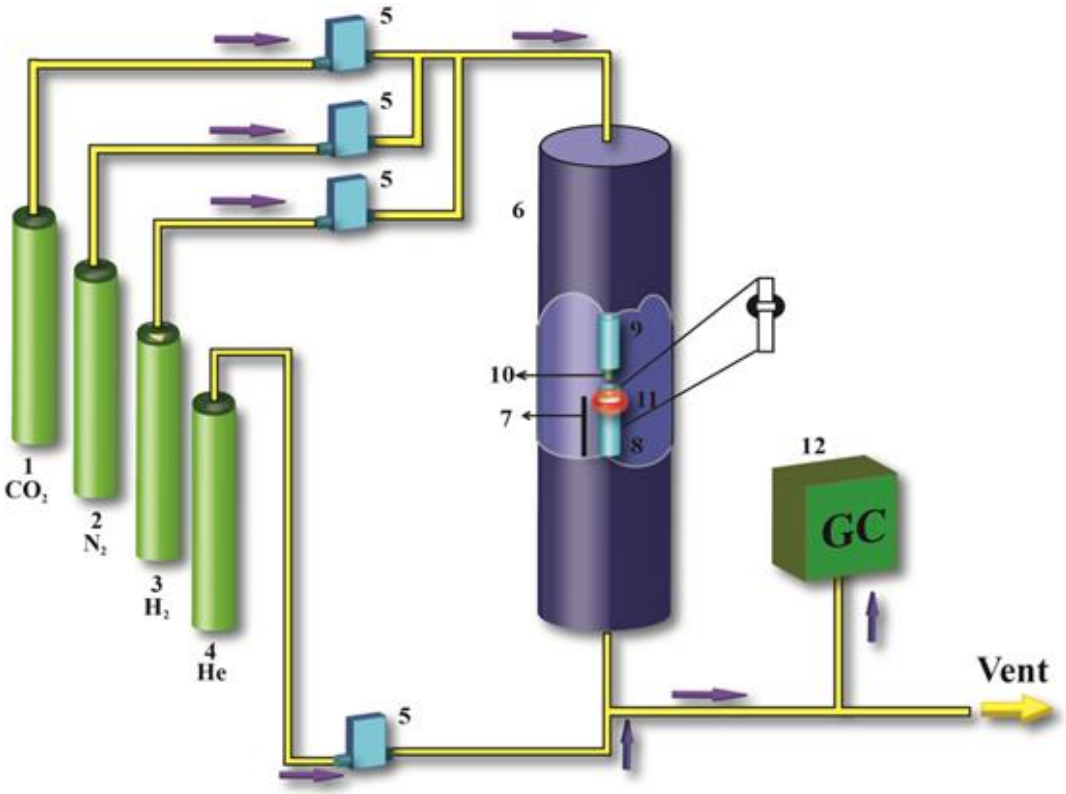

Figure 4.4 Schematic of the CO_2 permeation cell configurations. (1) CO_2 cylinder; (2) Nitrogen cylinder; (3) Hydrogen cylinder; (4) Helium cylinder; (5) Mass flow controllers; (6) Furnace; (7) Thermocouple; (8) Al_2O_3 support tube; (9) Outer feed tube; (10) Inner feed tube; (11) MOCC membrane; (12) Gas chromatography (GC).

where, c_{N_2} and c_{CO_2} are the measured concentrations of N_2 (leakage) and CO_2, respectively. Q (ml/min) is the flow rate of the helium sweeping gas, and *S* is the

effective reaction area of the sample, =0.921 cm^2 for this study. The final leakage-corrected CO_2 flux density were calculated by

$$J_{CO_2} = J_{CO_2,total} - 1.0 \times J_{N_{2,leak}} \quad (4\text{-}3)$$

where the correction factor of 1.0 is the ratio between CO_2 flow rate (50 mL min^{-1}) and N_2 flow rate (50 mL min^{-1}) in the feed gas.

4.2.2 Properties of the MOCC dual-phase membrane

The CO_2 flux densities measured from a series of MOCC compositions are shown in Fig. 4.5 as a function of temperature. As expected, the CO_2 flux densities increase with temperature, confirming that the transport of CO_3^{2-} and O^{2-} is a thermally activated process. For a given temperature, the CO_2 flux densities also increase with the volume fraction of MC phase, which can be ascribed to a combined effect from microstructural factors, volume fractions and conductivity of each phase. This trend is also favorably confirmed by the theoretical analysis of ionic transport to be discussed later. Overall, the level of CO_2 flux density achieved is remarkable: at 700°C it increases from 0.26, 0.45, 0.64 and 1.84 ml $min^{-1}cm^{-2}$ for MOCC-A (30vol% MC) through D (50vol% MC), respectively. The high flux promises the lowering of operating temperature, particularly

when thinner membranes are employed, to enhance the durability for potential commercial applications.

The CO_2 flux densities are also observed to follow closely with Arrhenius relationship in Fig. 4.5 (b), the slope of which representing the activation energy, E_a, varies from 0.80, 0.83, 0.78 to 0.77 eV for MOCC-A through D, respectively..

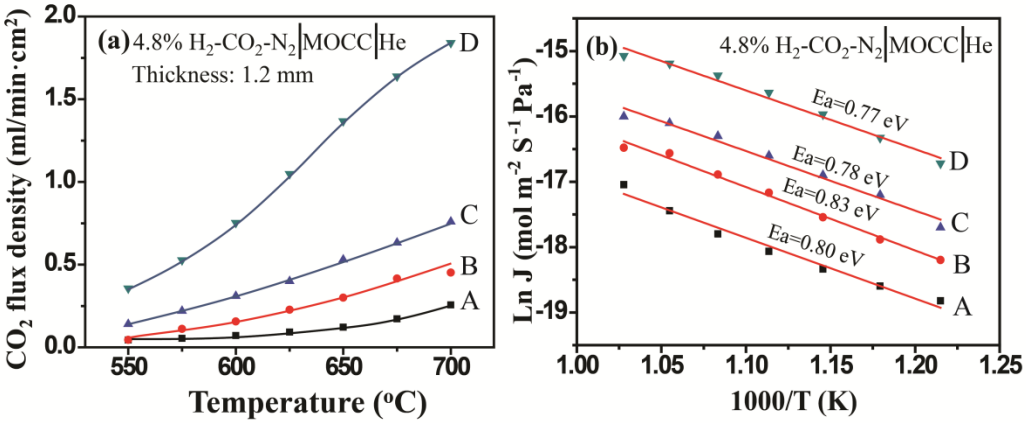

Figure 4.5 (a) CO_2 flux density as a function of temperature and (b) Arrhenius plots of CO_2 flux density. MOCC-A: 70vol%SDC-30vol%MC; B: 65vol%SDC-35vol%MC; C: 60vol%SDC60 -40vol%MC; D: 50vol%SDC-50vol%MC.

These values are sufficiently close to 0.78 eV for oxide-ion conduction in SDC electrolytes reported in the literature[98], suggesting that the ionic transports in these

samples share the same mechanism and are limited by the oxide-ion migration. Such an understanding is reasonable considering the fact that the conductivity of oxide-ions in the SDC phase is more than two orders of magnitude lower than that of the MC phase

The fact that the CO_2 flux density is limited by the oxide-ion transport is further confirmed in Fig. 4.6 where CO_2 flux density of MOCC-A (70vol% SDC-30vol% MC) is shown to linearly increase with partial pressure of hydrogen (P_{H_2}).

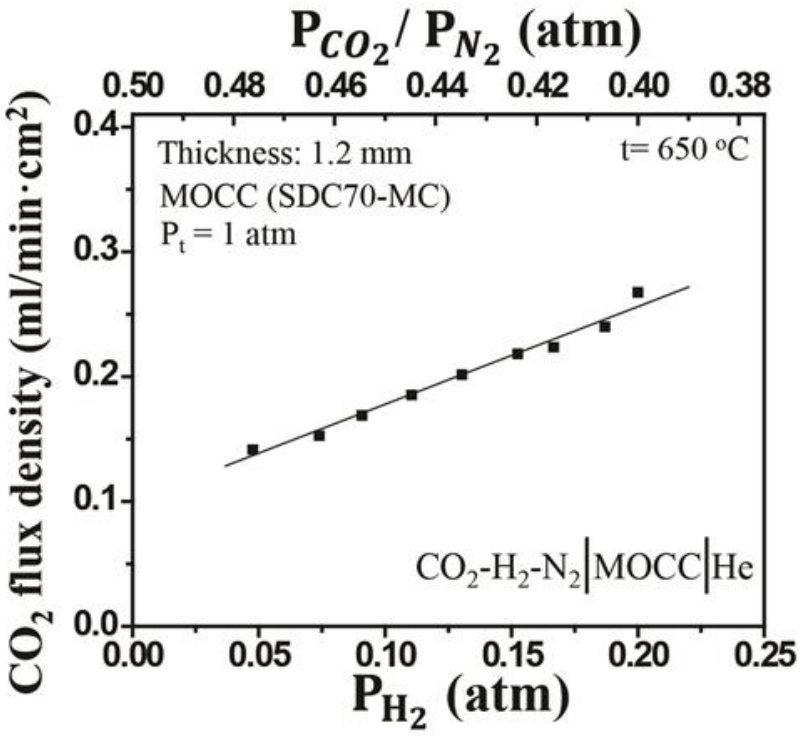

Figure 4.6 Dependence of CO_2 flux density of MOCC-A on H_2-concentration at 650°C

An increased P_{H_2} implies a lowered P_{O_2}, which in turn increases the chemical gradient of oxygen across the membrane, thus raising the flux of oxide-ion. By the charge neutrality requirement, the flux of carbonate-ion will be correspondingly enhanced. The sensitivity of CO_2 flux density to P_{H_2} is an indirect evidence that the bulk oxide-ion transport is a flux-limiting step.

An important side chemical reaction worthy of investigation when dealing with H_2 and CO_2 mixture is coking resulting from reverse water gas shift reaction $CO_2+H_2=CO+H_2O$ and Boudouard reaction $2CO=CO_2+C$. Thermodynamic analysis outlining the boundaries for carbon formation is given in Fig 4.7. Figure 4.7 shows the domain for carbon formation under the experimental conditions employed in this study. Outotec HSC Chemistry 5.0 was used for the thermodynamic analysis. A general trend is that the temperature at which carbon is formed increases with P_{H_2}. To avoid coking, the minimum temperature for flux measurements carried out in this study has been set to 550^oC.

The obtained CO_2 flux densities of the MOCC with various compositions are also compared with the literature in Fig. 4.8. To do so, the measured flux densities shown in Fig. 4.8 (a) need to be converted into CO_2 permeability as defined by $Jco_2/\Delta Pco_2$ along with normalized thickness. The comparison indicates that the permeability of the MOCC developed in this study is at least two orders of magnitude higher than that reported in

YSZ-MC and CGO-MC at 650°C[69] and at least one order of magnitude higher than LSCF-MC membrane at 700°C[87].

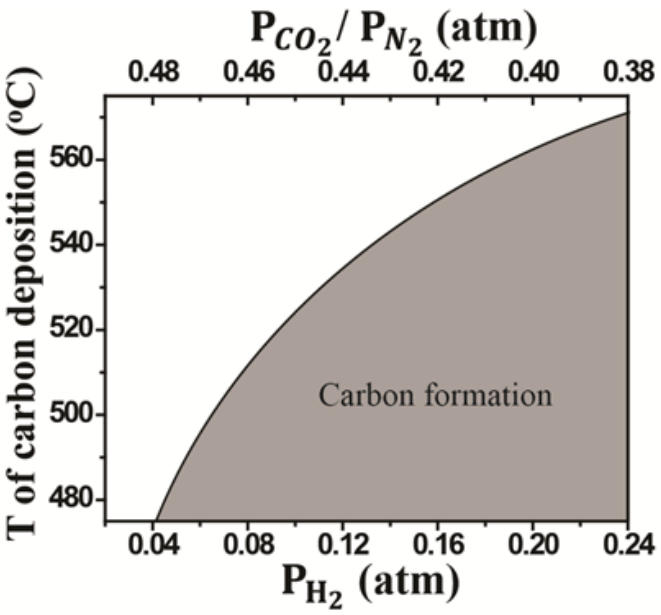

Figure 4.7 Carbon formation domain for a H_2-CO_2-N_2 system determined by thermodynamic analysis

The significant improvements are attributed to the highly efficient microstructure synthesized by combined "co-precipitation" and "sacrificial template" method, which provides a vast number of intra- and interconnected pathways for high-rate ionic transport in dual phase mixed-ion conductors.

The CO_2 flux densities shown in Fig. 4.9(a) are also compared in Fig. 4.8 with theoretical calculations. The parameters used for the calculations are listed in Table 4-1, where the microstructural factors such as ε and τ were obtained directly from mercury porosimetry measurements. The independently calculated values are compared with independently measured data points in Fig. 4.9. An excellent agreement between the two is explicitly displayed, thus convincingly validating the microstructure-modified flux equation (2-19) and confirming that the ionic transport is controlled by bulk-diffusion at the thickness level of this study.

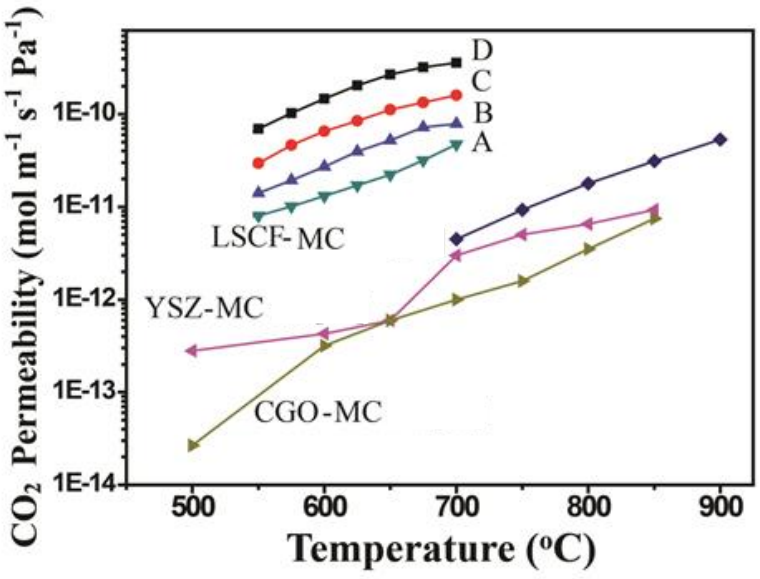

Figure 4.8 Comparison of CO_2 permeability of the MOCC developed in this study with LSCF-MC, YSZ-MC and CGO-MC membranes available in the literature. Letters A through D have the same meanings as those in Fig. 4-5 (a).

$$J_{CO_2} = -\left(\frac{\varepsilon}{\tau}\right)\frac{RT}{4F^2L}\frac{\varphi\sigma_c(1-\varphi)\sigma_o}{\varphi\sigma_c+(1-\varphi)\sigma_o}\ln\frac{P''_{CO_2}}{P'_{CO_2}} \qquad (2\text{-}19)$$

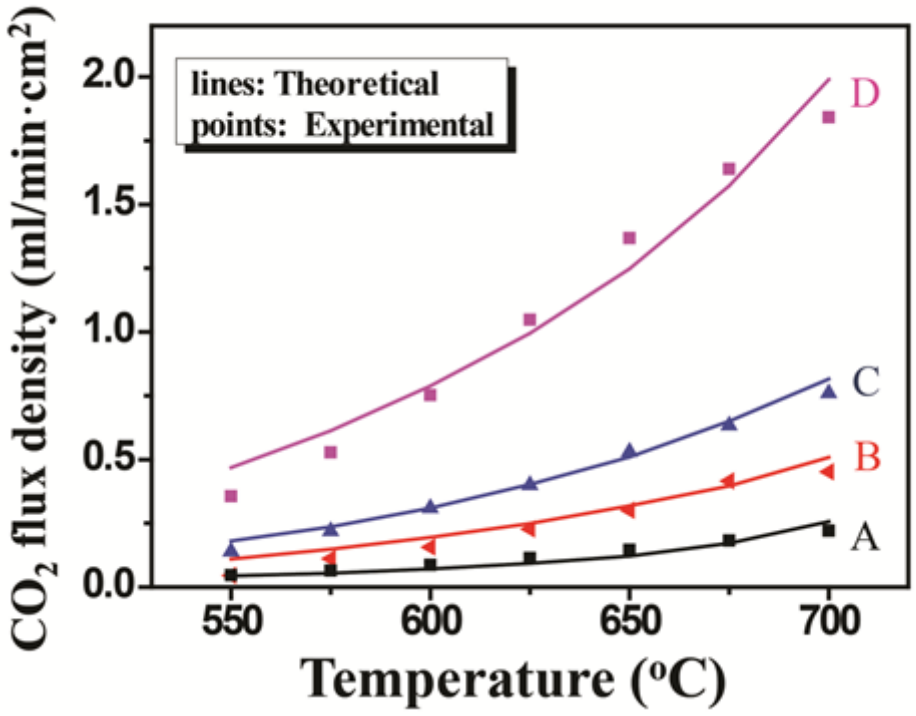

Figure 4.9 Comparison of the measured CO_2 flux density with theoretical calculations using existing flux transport model. Letters A through D have the same meanings as those in Fig. 4-5(a).

The flux density measured in this study is usually stable during the characterizing period (10-15 hours). However, extended testing showed flux degradation accompanied by an increased concentration of N_2, indicating the occurrence of MC loss. Therefore,

retention of MC is critical to the long-term stability of the developed MOCC membrane. The knowledge of immobilizing MC learned from molten carbonate fuel cell technology can be applied to future research to enhance the long-term stability.

Table 4.1Parameters used in the calculations of theoretical CO_2 flux density

σ_o=224.6 exp(-9051.5/T) T=400-700^{o}C (S/cm)[98]				
σ_c=83.8 exp (-3716.7/T) T=450-650^{o}C (S/cm)[72]				
Thickness (mm)	1.2			
P'_{CO2} (Pa)	48250			
P''_{CO2} (Pa)	varied			
	φ	ε	τ	ε/τ
Sample A	0.30	0.321	26.1	0.0123
Sample B	0.40	0.366	11.3	0.0324
Sample C	0.45	0.436	5.71	0.0765
Sample D	0.50	0.531	2.27	0.234

4.3 CHARACTERIZATIONS AND PROPERTIES OF THE MECC DUAL-PHASE MEMBRANE

4.3.1 CO_2 flux measurement of MECC

The CO_2 permeation cell configurations of MECC membrane is with the same as that of MOCC membrane shown in Figure 4.10. The button-type membrane was first sealed to a supporting alumina tube with a commercial silver paste as a sealant. A second short alumina tube was then bonded to the top of the sample for the purpose of shielding the feed gas. The feed gas was a mixture of 50 ml min^{-1} O_2, 50 ml·min^{-1} CO_2 and 20 ml·min^{-1} N_2; N_2 was used as a tracer gas for leak correction if any. For the study of CO_2-effect on CO_2 flux density, small incremental flow rates of CO_2 and O_2 were added with 1:1 ratio. The flow rate of N_2 was change accordingly without changing the total gas flow rate of 120 ml min^{-1}. For the study of CO_2 driving force effect on CO_2 flux density, the ratio of CO_2/O_2 was gradually varied in the range of 10 ml min^{-1} to 84 ml min^{-1}. The flow rate of N_2 was change accordingly without changing the total gas flow rate of 120 ml min^{-1}.

A high-purity helium (99.999%) at a flow rate of 50 ml·min^{-1} was used as the sweeping gas, the composition of which was analyzed by an on-line micro-GC (Varian 490-GC, Varian). To ensure the accuracy, the GC was calibrated with four standard gas compositions for each gas of interest (CO_2, O_2, and N_2). The final CO_2 flux density was

calculated out from an average gas composition of a total of ten successive readings from the GC. For all gas flows, commercial mass flow controllers (Smart-Trak, 50 Series) specifically calibrated for the gas under use were employed to control the mass flow rates. The temperature of permeation cells was varied from 500 to 650^{o}C in an interval of 25^{o}C. At each temperature, 30 minutes were given to allow the cell to reach steady state before sampling. The flux densities of the CO_2 (total), O_2 (total) and N_2 (leakage), were calculated using the following equations:

$$J_{N_{2,leak}} = \frac{c_{N_2}}{(1 - c_{CO_2} - c_{O_2} - c_{N_2})} \times \frac{Q}{S} \tag{4-4}$$

$$J_{CO_2,total} = \frac{c_{CO_2}}{(1 - c_{CO_2} - c_{O_2} - c_{N_2})} \times \frac{Q}{S} \tag{4-5}$$

$$J_{O_2,total} = \frac{c_{O_2}}{(1 - c_{CO_2} - c_{O_2} - c_{N_2})} \times \frac{Q}{S} \tag{4-6}$$

where, cN$_2$, cCO$_2$ and cO$_2$are the measured concentrations of N_2 (leakage), CO_2 (total) and O_2 (total), respectively. Q is the flow rate of the helium sweeping gas, and S is effective reaction area of the sample. The N_2 concentration leaked through membrane was very low, averaging <0.01% (sometimes not even detectable), proving silver sealing is an excellent method to achieve gastight cell. The final fluxes of the permeated CO_2 and O_2 were corrected by where the correction coefficient of 2.5.

$$J_{CO_2} = J_{CO_2,total} - 2.5 \times J_{N_{2,leak}} \tag{4-7}$$

$$J_{O_2} = J_{O_2,total} - 2.5 \times J_{N_{2,leak}} \tag{4-8}$$

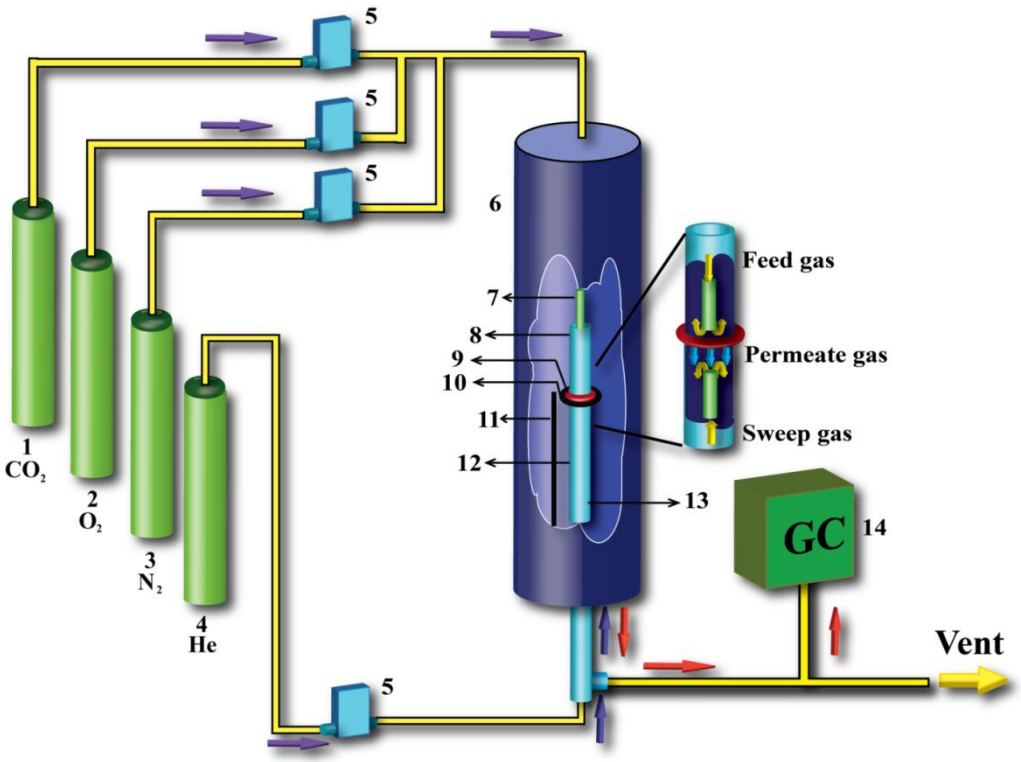

Figure 4.10 Schematic of the CO_2 permeation cell configurations. (1) CO_2 cylinder; (2) oxygen cylinder; (3) nitrogen cylinder; (4) helium cylinder; (5) mass flow controllers; (6) furnace; (7) inner feed tube; (8) second short alumina tube; (9) MECC membrane; (10) silver paste; (11) thermocouple; (12) supporting alumina tube; (13) inner sweep tube; and (14) gas chromatography (GC).

4.3.2 Properties of MECC dual-phase membranes

4.3.2.1 MECC membrane using silver porous matrix created by microcrystalline methylcellulose pore former

The CO_2 flux densities measured from Ag-MC membranes (40 vol% MC) uncoated (Sample-A), and coated with 5 wt% (Sample-B) and 10 wt% (Sample-C) Al_2O_3 colloidal are shown in Fig.4.11 (a) as a function of temperature. As expected, the CO_2 flux densities increase with temperature, confirming that the transport of CO_3^{2-} and e^- is a thermally activated process. Compared with the uncoated silver-MC (sample-A) membrane, the CO_2 flux density of Sample-B is slightly lower at $t<600^oC$, above which the CO_2 flux density of sample-B is higher, indicating a higher activation energy for Sample-B. Sample-C exhibits a CO_2 flux density lower than both Sample-A and Sample-B over the entire temperature range tested. These results seem to suggest that 5% is the upper limit for the concentration of Al_2O_3 colloidal, above which excess Al_2O_3 layer begins to hinder the bulk transport of CO_3^{2-} and surface exchange kinetics due to the insulating nature of Al_2O_3 and/or $LiAlO_2$. Therefore, only Sample-B was further studied for other performances.

Arrhenius plots of CO_2 and O_2 flux densities of Sample-A and Sample-B are shown in Fig.4.11 (b). The less important Sample-C was not included in the figure for the sake of clarity. The apparent activation energies E_a for Sample-A are 60.8 and 66.6

KJ/mol for CO_2 and O_2 flux densities, respectively; this is in excellent agreement with our previous results[99]. With 5% Al_2O_3 coating, Sample-B's E_a are increased to 81.0 and 78.2 KJ/mol for CO_2 and O_2, respectively, while it is increased to 74.7 and 82.5 KJ/mol for CO_2 and O_2, respectively, for 10% Al_2O_3 coated Sample-C. The higher E_a for Sample-B and Sample-C can be reasonably related to the blocking effect of Al_2O_3 on the migration of CO_3^{2-} and e^- and surface exchange kinetics. Moreover, the proximity in E_a for the two different active species (CO_2 and O_2) infers that the activation processes for CO_2 and O_2 are likely to involve in the same enabling electrochemical reaction of eq.(2-24). Overall, Fig.4.11 (c) shows a remarkable level of CO_2 and O_2 flux densities for Sample-B, achieving 0.39 $ml \cdot cm^{-2} \cdot min^{-1}$ and 0.20 $ml \cdot cm^{-2} \cdot min^{-1}$ for CO_2 and O_2, respectively, at 650°C. The flux ratio of CO_2 to O_2 is consistent with the theoretical CO_2:O_2=2:1 predicted from eq.(2-24). The CO_2 transport through molecular dissolution in MC is possible, but expected to proceed with a very slow rate. Ionic transport should be the dominant form of CO_2 transport in the silver-carbonate membranes.

To further determine the effect of Al_2O_3 coating on the long-term stability of flux, the fluxes were measured as a function of time at 650°C, the results of which are shown in Fig.4.12 (a) for Sample-A and Sample-B. The CO_2 and O_2 fluxes of the Sample-A are seen to decay quickly with time in approximate 2:1 ratio for the first 20 h. The loss of MC resulted from poor wettability and silver sintering is believed to be the reason for the

flux decline. In fact, some escaped MC from the sample was evident on the permeate side of the sample after the test. On the contrary, Sample-B exhibits CO_2 and O_2 flux densities of 0.39 $ml \cdot cm^{-2} \cdot min^{-1}$ and 0.20 $ml \cdot cm^{-2} \cdot min^{-1}$, respectively, from the beginning. The flux densities increased slightly with the time during the first 10 h and then remained relatively flat for the next 120 h. This small degree of flux increase can be ascribed to the marginal reduction in membrane thickness as a result of the MC loss and silver sintering. At the 130-h marker, the CO_2 and O_2 flux densities were still 0.32 $ml \cdot cm^{-2} \cdot min^{-1}$ and 0.168 $ml \cdot cm^{-2} \cdot min^{-1}$, roughly 90% of the original values.

To understand the flux behavior shown in Fig.4.12 (a), SEM imaging was performed on the post-tested Sample-A and –B, the microstructures of which are shown in Fig.4.12 (b) & (c), respectively. By comparing the morphologies of the two samples, it is evident that the excessive grain growth of Ag and loss of the MC in Sample-A has occurred during the measurement (marked areas represent voids left by MC loss). In contrast, only a small fraction of voids are present in Sample-B.

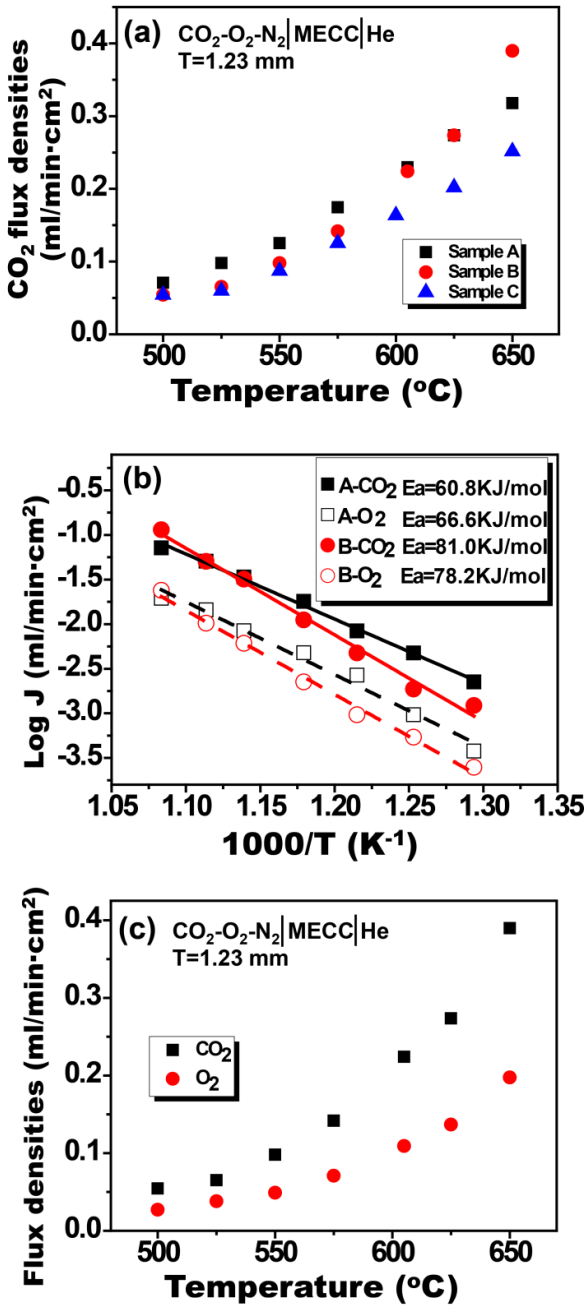

Figure 4.11 (a) CO_2 flux densities of Sample-A, Sample-B, and Sample-C as a functional of temperature; (b) Arrhenius plots of CO_2 and O_2 flux densities of Sample-A and Sample-B; (c) CO_2 and O_2 flux densities of Sample-B as a functional of temperature.

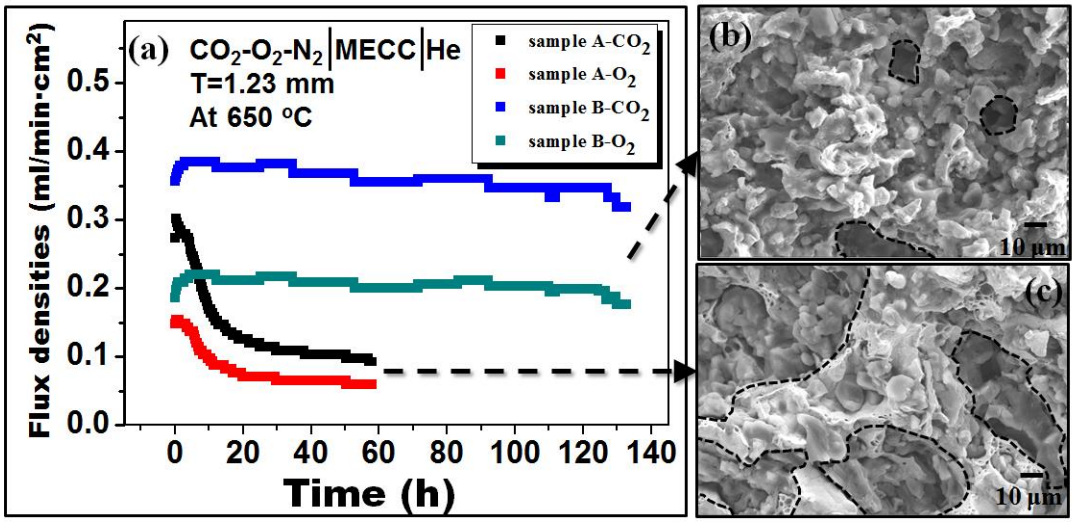

Figure 4.12 (a) Long-term stability of CO_2 and O_2 flux densities of Sample-A and -B measured at 650°C; Microstructures of (b) Sample-B and (c) Sample-A after long-term stability test.

To check the chemical homogeneity of the post-tested Sample-A and –B, SEM/EDS mapping analysis was conducted. The elemental distributions in Sample-A and -B are shown in Fig.4.13 and Fig.4.14, respectively. The elemental distributions of Ag and K shown in Fig.4.13 of Sample-A imply that excessive silver grain growth and loss of MC have occurred during the testing. This observation is consistent with Fig.4.12. In contrast, the elemental distributions of Ag, Al and K in Fig.4.14 of Sample-B indicate much smaller silver grain growth and more MC remained in the post-tested sample. This

drastic difference is simply made by coating a thin layer of Al_2O_3 on the surface of a porous silver matrix. Overall, these comparative results strongly suggest the bi-functionality of Al_2O_3 coating: improving silver's wettability with MC and limiting silver's thermal coarsening during high-temperature operation.

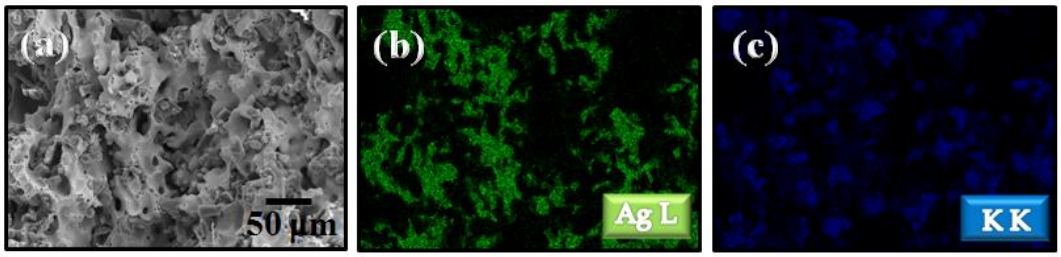

Figure 4.13 Microstructure and elemental distributions of Sample-A after a long-term stability test (a) SEM image; (b) Ag mapping; (c) K mapping. Note: Li is not detectable by EDS.

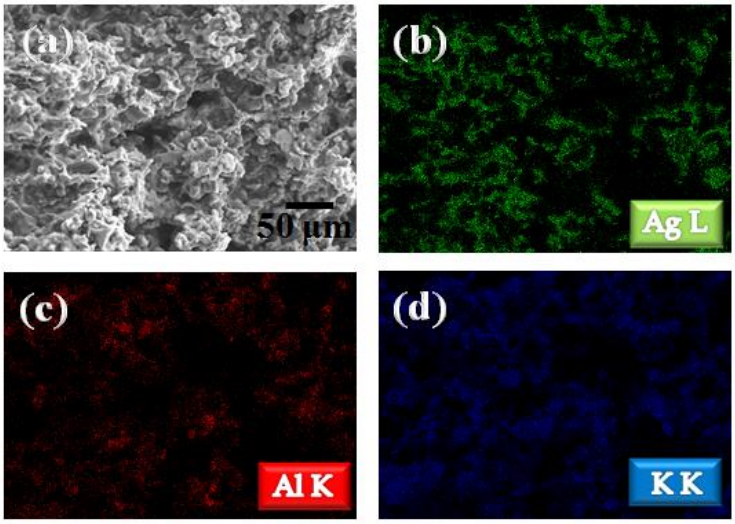

Figure 4.14 Microstructure and elemental distributions of Sample-B after a long-term stability test (a) SEM image; (b) Ag mapping; (c) Al mapping; and (d) K mapping. Note: Li is not detectable by EDS.

4.3.2.2 MECC membrane using silver porous matrix created by carbon black pore former

The CO_2 flux densities measured from Ag-MC membranes coated without (Sample-A) and with 5 wt% (Sample-B) Al_2O_3 colloidal are shown in Fig.4.15 as a function of temperatures. As expected, the CO_2 flux densities increase with temperature, confirming that the transport of CO_3^{2-} and e^- is a thermally activated process. Overall, the flux densities of the two samples are equivalent over the temperature range tested, which suggests that the 5 wt% colloidal coated Al_2O_3 layer does not significantly affect the transport of CO_3^{2-}. Therefore, Ag-MC membrane with 5 wt% Al_2O_3 colloidal coated was used as a standard for other performance characterizations.

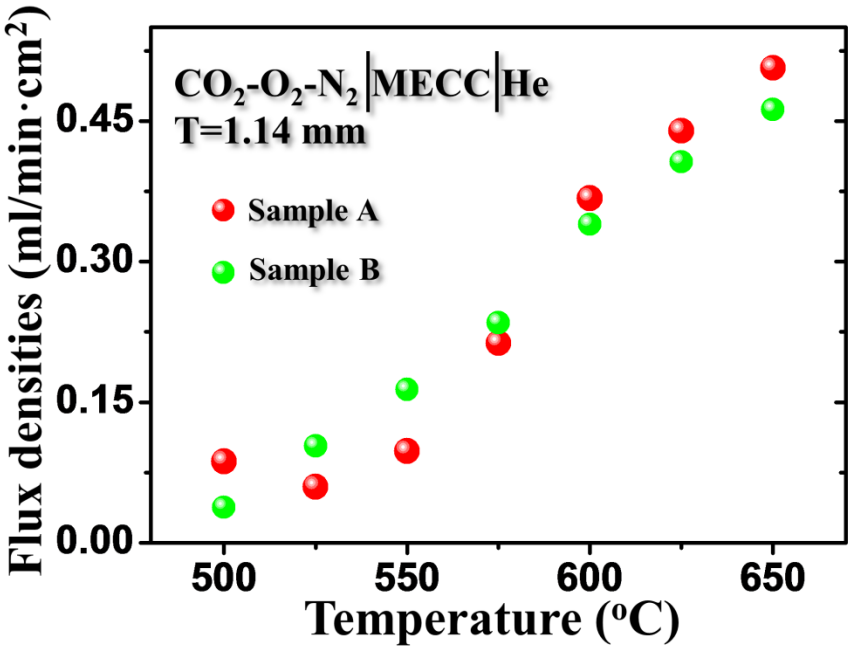

Figure 4.15 (a) CO_2 flux densities of Sample-A and Sample-B as a functional of temperature;

To demonstrate the effect of membrane's thickness on CO_2 and O_2 flux densities, five levels of thickness were prepared: 0.63, 0.84, 1.14, 1.21 and 1.45 mm. The CO_2 and O_2 flux densities as a function of the reciprocal of thickness are shown in Figure 4.16. It is evident that the CO_2 and O_2 flux densities exhibits almost a linear relationship with a reciprocal of thickness of MECC membrane from 1.45-0.84 mm, but a plateau at a thickness less than 0.84 mm

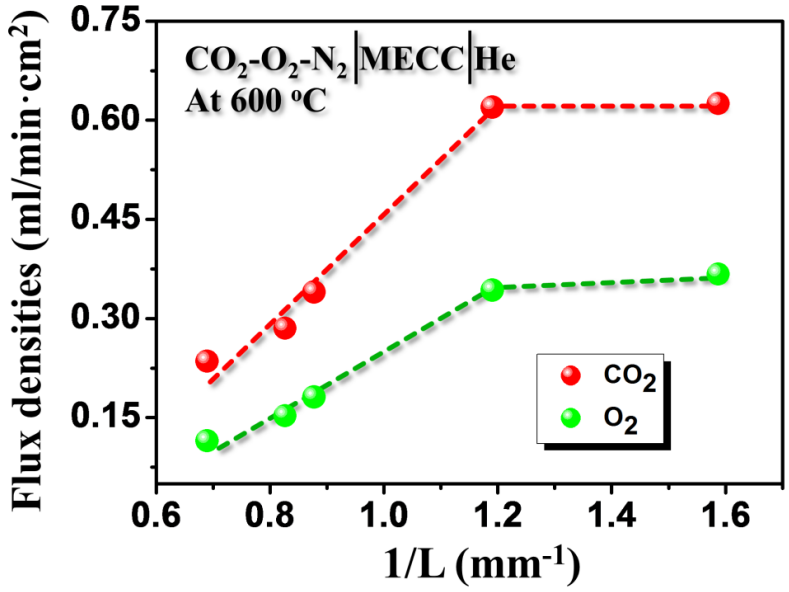

Figure 4.16 CO_2 and O_2 flux densities of MECC membrane as a function of the reciprocal of thickness at 600 °C.

. According to flux equation (2.23), the linearity between J_{CO2} and 1/L suggests a bulk diffusion controlled CO_2 transport mechanism at a thickness greater than 0.84 mm. The insensitivity of J_{CO2} to L signals that surface exchange kinetics of CO_2 and O_2 reduction play a major role in limiting the overall CO_2 transport flux. Therefore, making thinner membrane to achieve higher flux does not have practical implications. The detailed CO_2 and O_2 flux densities of different thickness of MECC membranes are shown in Table 4.2.

In the flux equation (2-23) of bulk diffusion control, the conductivity of carbonate ions is assumed to be independent of partial pressures of CO_2 and O_2. The resultant J_{CO2}

is therefore proportional to the natural logarithm of $P_{CO_2}P_{O_2}^{1/2}$. However, such a relationship is not supported by the experimental data shown in Fig.4.17 (a). According to the basic electrochemical reaction (2-4), it seems to be reasonable to assume that $\sigma_{CO_3^{2-}}$ has the following relationship with P_{CO2} and P_{O2}:

$$\sigma_{CO_3^{2-}} = \sigma^o P_{CO_2} P_{O_2}^{1/2} \tag{2-24}$$

Table 4.2 CO_2 and O_2 flux densities of different thickness of MECC membranes

Thickness (mm^{-1})	CO_2 flux density ($ml/min\ cm^2$)	O_2 flux density ($ml/min\ cm^2$)
1.45	0.235	0.115
1.21	0.285	0.153
1.14	0.340	0.181
0.84	0.620	0.343
0.63	0.625	0.367

Substituting eq. (2-24) into eq. (2-11) and integrating over the range of chemical gradient and thickness with the assumption of $\sigma_{e-} >> \sigma_{CO32-}$ yield the following flux equation:

$$J_{CO_2} = -\left(\frac{\varepsilon}{\tau}\right)\frac{3RT}{8F^2L}\varphi\sigma^o\left(P''_{CO_2}P''^{1/2}_{O_2} - P'_{CO_2}P'^{1/2}_{O_2}\right) \tag{2-25}$$

It is evident from this equation that J_{CO2} is proportional to the difference of $P_{CO_2} P_{O_2}^{1/2}$ at the two reacting surfaces. Following this new flux equation, we replot the J_{CO2} measured in Fig.4-17(b) and find a nearly perfect linear relationship. This finding suggests that eq (2-24) is an adequate assumption for the dependence of the conductivity of CO_3^{2-} on P_{CO2} and P_{O2}.

The long-term stability of CO_2 and O_2 flux densities is show in figure 4.18. The membrane exhibits CO_2 and O_2 flux densities of 0.28 ml·cm^{-2}·min^{-1} and 0.145 ml·cm^{-2} ·min^{-1}, respectively, from the beginning. The flux densities increase with the time during the first 160 h, reaching 0.6 ml·cm^{-2}·min^{-1} and 0.32 ml·cm^{-2}·min^{-1} in approximate 2:1 ratio and then slightly decreasing for the next 90 h. At the 250-h marker, the CO_2 and O_2 flux densities are still 0.44 ml·cm^{-2}·min^{-1} and 0.22 ml·cm^{-2}·min^{-1}, roughly 160% of the original values.

To further check the chemical homogeneity of MECC membrane, SEM and EDS mapping analysis were conducted. The chemical elemental distributions of the MECC membrane are shown in Fig. 4.19. It suggests that Ag, Al_2O_3 and MC phases are still well distributed across the membrane even after the long-term test. There is no obvious change in phase compositions and microstructure from the original sample. By comparing the morphologies of before (Figure 3.21) and after the long term test, it is evident that the loss of the MC in MOCC has taken place during the test. This finding may be related to

the increase in flux shown in Fig.4-18 as a result of reduced effective thickness of the membrane.

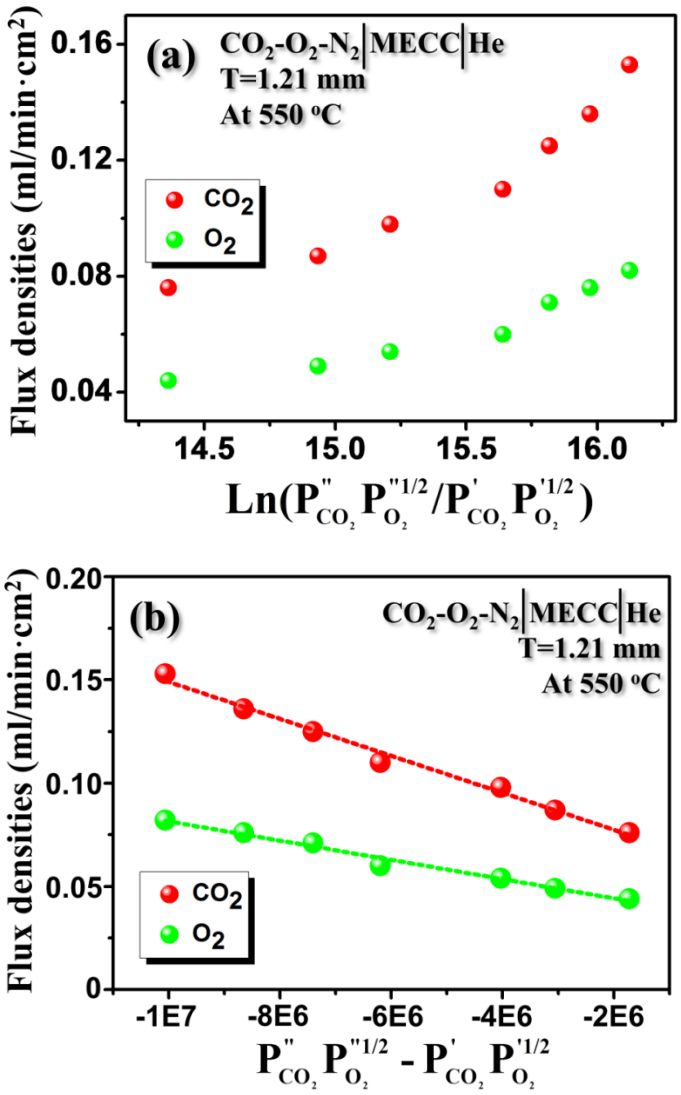

Figure 4.17 CO_2 and O_2 flux densities of MECC membrane with the thickness of 1.21 mm as a function of CO_2 and O_2 chemical gradient at 550 ^oC. (a) with natural logarithm relationship; (b) with a linear relationship

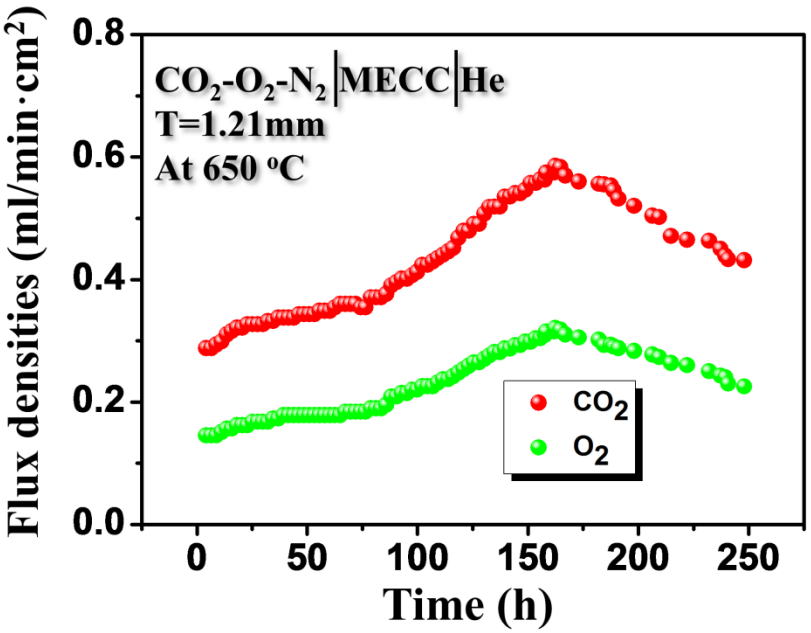

Figure 4.18 Long-term stability of CO_2 and O_2 flux densities of a MECC membrane measured at 650°C.

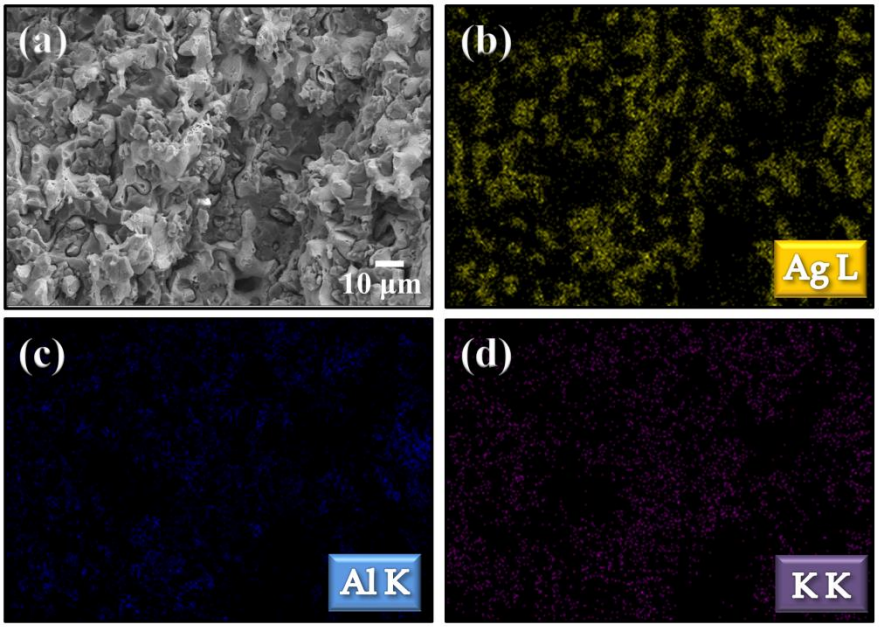

Figure 4.19 Microstructure and elemental distributions of Sample-B after a long-term stability test (a) SEM image; (b) Ag mapping; (c) Al mapping; and (d) K mapping. Note: Li is not detectable by EDS.

As the loss of MC continues, the integrity of the membrane could be compromised as suggested by the increase in the concentration of tracer gas N_2 in the sweeping stream. This becomes the reason why the flux decreases after 160 hours.

4.4 CONCLUSIONS

A dual-phase ceramic-carbonate mixed-ion conducting membrane for electrochemical CO_2 separation from a reducing stream has been synthesized by filling a highly interconnected, porous solid oxide-ion conducting ceramic matrix with a carbonate-ion conducting molten carbonate. A combined "co-precipitation" and "sacrificial template" technique was demonstrated to produce a highly efficient porous ceramic matrix containing a vast number of intra- and interconnected pathways for fast-ion transport. The performance of thus synthesized MOCC membrane is remarkable, showing a CO_2 flux density two orders of magnitude higher than ceramic-carbonate systems fabricated with other methods. Moreover, the measured CO_2 flux densities are in excellent agreement with theoretical predictions using a microstructure-modified flux equation. Overall, the developed MOCCs show promise to be a new class of high-performance and cost-competitive membranes for electrochemical separation of CO_2 from a pre-combustion process stream.

A surface-modified dense silver-MC dual-phase MECC membrane for CO_2 separation from flue gas has been also demonstrated with improved stability in this study. Two pore formers were investigated to make the porous silver matrix: microcrystalline methylcellulose and carbon black. The surface modifier is Al_2O_3, which was prepared by coating Al_2O_3 colloidal onto the exposed surfaces of a porous silver matrix. The results show that the use of 5% Al_2O_3 colloidal gives MECC the best flux density and stability compared to the unmodified sample. Approximately 90% of the original flux values can still be maintained after 130-hour testing for the modified membrane with microcrystalline methylcellulose pore former, whereas only one-third of the original flux values can be retained even after 60 hours for the unmodified membrane. For the surface modified MECC membrane with carbon black pore former, the CO_2 flux was found to increase with time for the first 160 hours by 200%, following by decreasing for the next 90 hours. At the 250-hour marker, the flux is still 160% of the original value. Overall, surface modification with Al_2O_3 is a viable approach to stabilizing silver-carbonate membranes for efficient and stable CO_2 capture from flue gas.

With the stabilized MECC membranes, we also demonstrate that the CO_2 flux follow a linear relationship with 1/L in a thickness greater than 0.84 mm, suggesting a bulk diffusion controlling mechanism. Below 0.84 mm, the flux remains flat, suggesting that the rate-limiting step has shifted to the surface exchange kinetics of CO_2 and O_2. We

also find that the CO_2 flux is proportional to the linear chemical gradient of CO_2 and O_2, implying that the conductivity of CO_3^{2-} is dependent of P_{CO2} and P_{O2} with a unity reaction order.

CHAPTER 5 IN-SITU RAMAN SPECTROSCOPIC STUDY OF MOCC MEMBRANE

5.1 INTRODUCTION

To understand the fundamentals of high-flux CO_2 transport through the MOCC membranes, we propose for the first time a multi-pathway bi-ionic transport model schematically in Chapter 2. A strong support to the new bi-ionic transport model is the experimental proof of $C_2O_5^{2-}$ existed on the surface of a MC exposed to CO_2 atmosphere. The likelihood of absorbing CO_2 on the surface of a MC to form $C_2O_5^{2-}$ has been suggested by Claes et al[100-102] who studied the solubility and solvation of CO_2 in a molten eutectic mixture of Li_2CO_3-Na_2CO_3-K_2CO_3 at 973K. They found CO_2 to be extremely soluble in MC. The solubility of 0.1 mol/liter/atm measured is well beyond what is expected from Henry's law. The authors concluded that chemical absorption was taking place, most probably by the reaction of CO_3^{2-}(MC) + CO_2(g) = $C_2O_5^{2-}$(MC). DFT calculations were carried out by the authors to gain insight into the reaction energetics. The calculated values for ΔH^o and ΔG^o are -223 kJ/mol and -119 kJ/mol at 973K, respectively, indicating favorable gas-phase energetics, and solvation should not hinder the formation of the postulated $C_2O_5^{2-}$ in the MC. Furthermore, another study reported

crossover ^{13}C NMR experiments between [^{13}C] and [^{18}O] carbonates in aqueous solutions of Na_2CO_3.[103] The complex kinetic problem was interpreted as giving evidence for the existence of the CO_3^{2-}(MC) + CO_2(g) = $C_2O_5^{2-}$(MC) equilibrium under these experimental conditions. Based on these early studies, it is, therefore, conceivable that the formation of $C_2O_5^{2-}$ species in MC by chemical absorption of CO_2 could well be a facile process. However, so far no direct experimental observation on the $C_2O_5^{2-}$ species in MC has been reported.

In this Chapter, we report the first spectroscopic observation of the $C_2O_5^{2-}$ species in a Li_2CO_3-Na_2CO_3 melt surrounded by CO_2 atmosphere as a key experimental evidence for the model proposed. A standard procedure to identify newly synthesized compounds or species in the chemical world is to record IR and Raman vibrational spectra. This procedure is relevant as long as the vibrational spectrum is not too congested (which usually happens below 900 cm^{-1} because of the superposition of bending, rocking, and torsional modes). In-situ Raman spectroscopy is, therefore, chosen as the method of study to probe $C_2O_5^{2-}$ species.

5.2 IN-SITU RAMAN SPECTROSCOPIC STUDY

5.2.1 Operation of in-situ Raman spectroscopy on MC

The MC under investigation consisted of Li_2CO_3 and Na_2CO_3 eutectic mixture (52:48 in mol%), which was first synthesized in air at 650^oC. After a 2-h hold, the melt was then

quenched to room temperature, followed by breaking into fine particles by ball milling. Thus prepared powders were then packed into a gold crucible that was subsequently loaded into a high temperature stage (Linkam TS1500, $0^{o}C$~$1500^{o}C$). The temperature and gas were controlled by a system controller (Linkam PE95). The Raman spectra were recorded with a LabRam/HR confocal Raman system (LabRam Invers, Horiba Jobin-Yvon) with a He-Ne laser operated at 632.8 nm. The LabRAM HR Evolution systems are ideally suited to both micro and macro measurements, and offer advanced confocal imaging capabilities in 2D and 3D. The true confocal microscope enables the most detailed images and analyses to be obtained with speed and confidence. The Features of LabRAM HR Evolution systems are: high spatial and spectral resolutions, UV to NIR, ease of use, ultra-fast confocal imaging, Raman-AFM and TERS compatible and ultra-low frequency.

Since the position of the thermal couples in the high temperature stage is located outside the crucible, the actual and the controlled temperatures of the MC are different. The melting point of the of $(Li/Na)_2CO_3$ at $490^{o}C$ was used to calibrate the actual temperature. The scattering Raman spectra were collected *in-situ* from the carbonate as a function of temperature (in the range of RT- $600^{o}C$) and atmosphere (in N_2, air, CO_2).

5.2.2 DFT modeling

DFT modeling was performed to confirm the experimental findings. The calculations used the B3LYP/6-31G(d)[40-44] level in Gaussian09 [45] suite of quantum programs. The geometry of $Li_2C_2O_5$ and $Na_2C_2O_5$ were optimized first, and the vibrational frequencies were then obtained from analytic second derivatives using a harmonic oscillator model. In addition, Raman intensities were computed by numerical differentiation of dipole derivatives with respect to the electric field.[46]

5.3 RAMAN SPECTRUM

Fig. 5.1 (a) shows the Raman spectra collected from a eutectic Li_2CO_3-Na_2CO_3 (52 mol% Li_2CO_3-Na_2CO_3) MC over a band range of 650-1,850 cm^{-1} as a function of temperatures in a pure CO_2 atmosphere. For the carbonate in solid state, the Raman spectra are seen to contain four basic vibrational modes relevant to CO_3^{2-}. The two bands at 1,078 and 1,094 cm^{-1} are assigned to ν_1 of symmetric stretching vibrations in Li_2CO_3 and Na_2CO_3, whereas the bands at 792 cm^{-1} and 870 cm^{-1} are assigned to ν_2 of out-of-plane bending vibrations. For the insolated CO_3^{2-} that has a D_{3h} symmetry, ν_2 is Raman inactive. However, it is likely that ν_2 becomes Raman active for $(Li/Na)_2CO_3$ due to the distortion of the CO_3^{2-} structure imposed by the cations.[104] The observed bands at 704 and 728 cm^{-1} are assigned to ν_4 of in-plane bending vibrations. This mode is a double degeneration for the distorted CO_3^{2-} induced by Li^+ and Na^+. As the CO_3^{2-} group becomes

distorted from its regular planer symmetry, this mode splits into two components.[105] The bands at 1,375 cm^{-1}, 1,404 cm^{-1}, 1,531 cm^{-1} and 1,563 cm^{-1} are attributed to a split ν_3 of the asymmetric stretching vibrations caused by the existence of Li^+ and Na^+ around the CO_3^{2-} ions.[104]

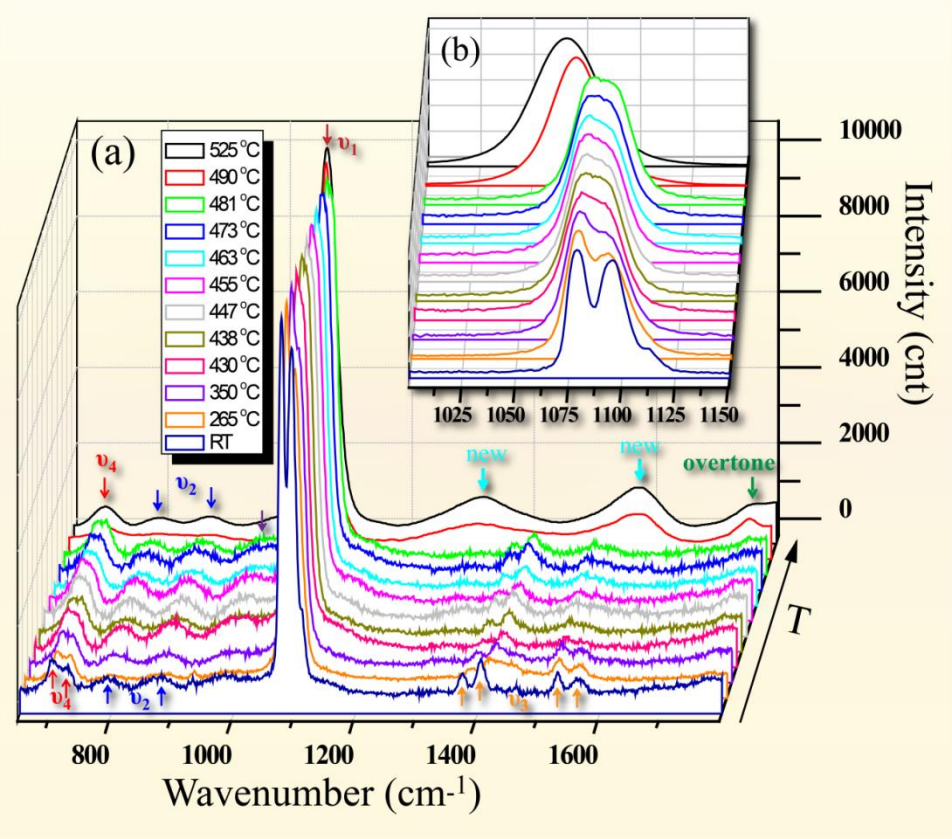

Figure 5.1 (a) The Raman spectra of $(Li/Na)_2CO_3$ in the region of 650-1850 cm^{-1} as a function of temperature in CO_2 atmosphere; (b) Magnified view in the region of 1,000-1,150 cm^{-1}

The shift in Raman band with temperature is better viewed in Fig. 5.1 (b), a magnified spectrum showing the region of the major ν_1 -bands at 1,078 cm^{-1} and 1,094

cm^{-1}. As the temperature increases, the ν_1 -bands for Li_2CO_3 and Na_2CO_3 shift toward lower wavenumber and eventually merge into one broad peak at the melting temperature of 490°C. This shift is a direct result of lowered force constant, elongated C-O bond length and weakened Li(Na)-C-O bond strength by increasing temperature.[106] When the temperature reaches the melting point, the overtone of the out-of-plane bending mode ($2*\nu_2$) appears at 1,762 cm^{-1}.[107] It should be noted that a broad but small peak near 970 cm^{-1} only observed in solid-state carbonates appears not directly related to CO_3^{2-}, identification of which is not possible for this study. We speculate impurities in the sample as a possible origin. A detailed assignment of the measured Raman bands at different temperatures and in atmospheres is summarized in Table 5-1.

The most distinguishable features of Raman spectra in Fig. 5.2 are observed when the carbonate is melted. The four bands corresponding to the ν_3 mode disappear from the spectrum and two new broad bands at 1,317 cm^{-1} and 1,582 cm^{-1} emerge. A natural question to ask is: are these newly emerged Raman bands associated with the $C_2O_5^{2-}$ species we are looking for?

To answer this question, we first measured Raman spectra in different atmospheres. According to the enabling electrochemical reaction shown in reaction (3), the formation of $C_2O_5^{2-}$ requires a source of CO_2. Fig.5.2 compares the Raman spectra measured in N_2, Air and pure CO_2 atmospheres at 490°C where the carbonate is in a molten state. The bands at 1,072 cm^{-1}, 790 cm^{-1} and 885 cm^{-1}, 707 cm^{-1}, 1,391 cm^{-1} and

1,421 cm^{-1}, 1,762 cm^{-1} shown in Fig. 5.2 (a) recorded in N_2 atmosphere correspond to the symmetric stretching (ν_1)， out-of-plane bending (ν_2), in-plane bending (ν_4), asymmetric stretching (ν_3), and the overtone of the out-of-plane bending mode ($2*\nu_2$) vibrations, respectively. The Raman spectrum in air is almost identical to that collected in N_2. However, the peaks at 1,317 cm^{-1} and 1,582 cm^{-1} shown in Fig.5.2 (c) are only observable in the CO_2 atmosphere. The CO_2-dependence of the bands at 1,317 cm^{-1} and 1,582 cm^{-1} provides a crucial hint to the formation of $C_2O_5^{2-}$ via CO_2 chemisorption reaction via reaction (3).

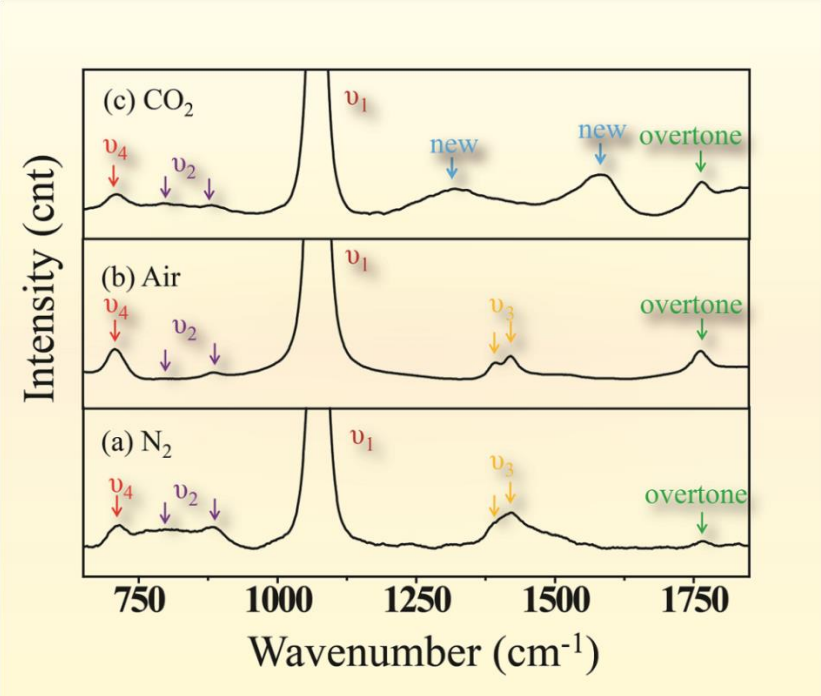

Figure 5.2 Raman spectra of molten $(Li/Na)_2CO_3$ measured as a function of atmosphere at 525°C

The theoretical support to the formation of $C_2O_5^{2-}$ is provided by DFT calculations. A description of DFT calculation can be found in the Electronic Supplementary Information. The calculations indicate that high Raman activities of $C_2O_5^{2-}$ are within a band width of 1,200-1,600 cm^{-1}. Specifically, the active Raman bands are predicted at 1,366 cm^{-1}, 1,531 cm^{-1} and 1,566 cm^{-1} for $Li_2C_2O_5$ and 1,345 cm^{-1}, 1,547 cm^{-1} and 1,579 cm^{-1} for $Na_2C_2O_5$, respectively. The recorded spectrum in the band width of 1,200-1,650 cm^{-1} from the MC at 490-525^oC in CO_2 atmosphere could, therefore, be an overlap of these characteristic Raman peaks of $Li_2C_2O_5$ and $Na_2C_2O_5$ in this band region. To deconvolute the two unique broad peaks around 1,317 cm^{-1} and 1,582 cm^{-1}, we used Guassian-Lorentizian function with the guidance from the six theoretical Raman frequencies suggested by the DFT calculations. The results are shown in Fig. 5.3, where the black and red lines represent the measured and modeled spectra, respectively. Also shown are the individual spectrum resulted from pure $Li_2C_2O_5$ and $Na_2C_2O_5$, represented by pink and blue lines, respectively. It appears that the modeled spectrum is dominated by the Na_2CO_3; only one peak at 1,566 cm^{-1} is visible for the Li_2CO_3 while the other two are too weak to be seen. This is primarily due to the size and polarizability effects of the cations. Overall, the measured Raman spectrum is in excellent agreement with the DFT calculations if the temperature effect is factored in.

Table 5.1 The Raman frequencies measured and assigned for eutectic $(Li/Na)_2CO_3$ at selected temperatures and atmospheres.

Atmospheres	**CO_2**				**Air**	**N_2**
Temperatures (^oC)	RT	350	455	490 (melted)	490 (melted)	490 (melted)
Frequencies (cm^{-1}) υ_4 (weak)	704	706	706	707	707	707
	728	720	715	-	-	-
υ_2 (weak)	792	790	789	790	790	790
	879	879	881	882	885	885
υ_1 (strong)	1,078	1,077	1,077	1,070	1,072	1,072
	1,094	1,090	1,087	-	-	-
υ_3 (weak)	1,375	1,385	1,386	-	1,391	1,392
	1,404	1,415	1,416	-	1,421	1,421
	1,531	1,520	1,520	-	-	-
	1,563	1,555	1,545	-	-	-
New peaks (broad)	-	-	-	1,317 1,582	-	-
Overtone ($2*\upsilon_2$)	-	-	-	1,762	1,762	1,762
Unknown	-	-	972	-	-	-

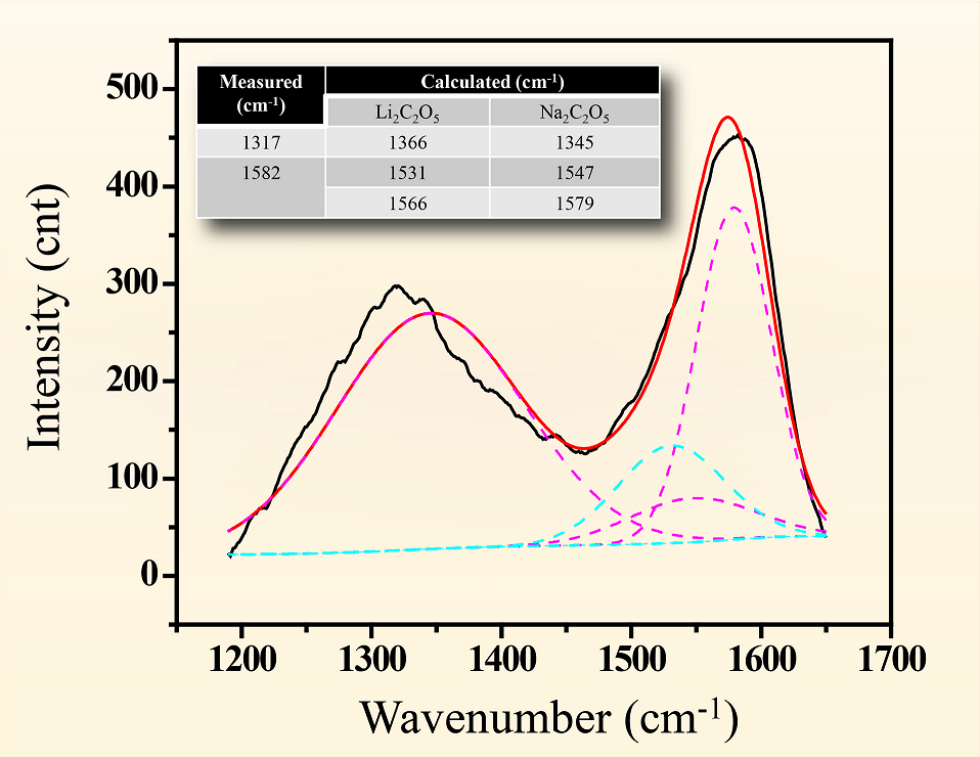

Figure 5.3 Deconvolution of the two broad bands observed at 1,317 cm^{-1} and 1,582 cm^{-1}; Inset: the measured and DFT-modeled Raman spectra in a band width of 1,200 - 1,650 cm^{-1}

5.4 CONCLUSIONS

In summary, we demonstrate for the first time evidence for the existence of pyrocarbonate $C_2O_5^{2-}$ species in a eutectic Li_2CO_3 and Na_2CO_3 melt subject to CO_2 atmosphere through a combined "DFT" and "Raman Spectroscopy" methodology. The existence of $C_2O_5^{2-}$ species is a key support to a new bi-ionic transport model proposed to understand the fundamentals of the high-flux CO_2 transport phenomenon observed in the mixed oxide-ion and carbonate-ion conducting membranes for superior electrochemical

CO_2 separation.The Raman bands observed at 1,317 cm^{-1} and 1,582 cm^{-1} are unique to the molten carbonates and dependent on the concentration of CO_2; these characteristics are the strong evidences for the formation of $C_2O_5^{2-}$ species. Furthermore, the measured Raman spectrum is in an excellent agreement with the DFT-modeled one.

CHAPTER 6 CONCLUDING REMARKS

The central objective of this dissertation research work is to develop a new class of dual-phase mixed oxide-ion and carbonate-ion conducting and mixed electron and carbonate-ion conducting membranes for pre-combustion and post-combustion CO_2 capture, respectively. The main strategy adopted to make a high flux, dense and robust membrane is to pre-fabricate a strong porous matrix, into which the molten carbonate can be impregnated.

A new "sacrificial template" method was successfully developed to fabricate a homogeneously porous SDC matrix. The microstructural characterization including 2D FESEM and 3D Micro-XCT and Nano-XCT evidently revealed a highly interconnected 3D ionic channel network. By varying the volume fraction of the sacrificial phase (NiO) and sintering temperature, the pore size, distribution and porosity has been shown with controllability. The effective ionic conductivity and CO_2 permeation flux of such a MOCC membrane are the highest among the published results.

The porous silver matrix for MECC membrane was fabricated with conventional solid state sintering with pore former. It was found that carbon black is a better pore

former of choice than microcrystalline methylcellulose, yielding a more uniform porous matrix and higher CO_2 permeation flux. To ensure a good retention of MC phase by the porous silver network, a wetting agent of Al_2O_3 was coated on the silver surfaces. The results explicitly show that the 5 wt% Al_2O_3 coating is very effective in extending the lifetime of MECC membranes. The level of CO_2 permeation flux is also the highest among the published results.

Theoretical analysis has been consistently applied in this research to guide the understanding of permeation flux behavior. From the classical flux theory, a new flux equation taking into account of microstructural factors has been developed for both MOCC and MECC membranes. The experimental results are in excellent agreement with the new flux equation. The effects of temperature, chemical gradient, and thickness on CO_2 permeation flux have also been studied and agreed with the new flux equation.

To understand the mechanism behind the high CO_2 flux observed in MOCC and MECC membranes, two new mechanistic transport models were proposed. The center of these two models is the two parallel ionic pathways occurring at three-phase and two-phase boundaries. The enabling species for the extended reaction zones include $C_2O_5^{2-}$ for MOCC, and CO_4^{2-} and CO_5^{2-} for MECC. To verify the existence of $C_2O_5^{2-}$, in-situ Raman spectroscopy was employed to probe the surface of a MOCC exposed to CO_2 at 600^{o}C. Two new Raman peaks at 1,317 cm^{-1} and 1,582 cm^{-1} were exclusively identified as the characteristic Raman shifts for the $C_2O_5^{2-}$. The DFT modeling favorably confirmed

that these two Raman shifts are attributed to the overlap of characteristic peaks of $Li_2C_2O_5$ and $Na_2C_2O_5$.

REFERENCES

1. U. S. Energy Information Administration, Annual Energy Outlook 2011, April 26, 2011.
2. U. S. Energy Information Administration, Energy Perspective 1949-2010, October 19, 2011.
3. Advanced carbon dioxide capture R&D program: technology update, DOE/NETL Technical Report, September 2010.
4. Carbon dioxide capture and storage RD&D roadmap, DOE/NETL Technical Report, December, 2010.
5. U. S. Energy Information Administration, Annual Energy Outlook 2012, June, 2012.
6. R. Bredesen, K. Jordal and O. Bolland, *Chemical Engineering and Processing: Process Intensification*, 2004, **43**, 1129-1158.
7. B. J. P. Buhre, L. K. Elliott, C. D. Sheng, R. P. Gupta and T. F. Wall, *Progress in Energy and Combustion Science*, 2005, **31**, 283-307.
8. J. F. M. Orr, *Energy & Environmental Science*, 2009, **2**, 449-458.

9. J. D. Figueroa, T. Fout, S. Plasynski, H. McIlvried and R. D. Srivastava, *International Journal of Greenhouse Gas Control*, 2008, **2**, 9-20.

10. R. S. Haszeldine, *Science*, 2009, **Science**, 1647-1652

11. L. I. Eide and D. W. Bailey, *Oil & Gas Science and Technology*, 2005, **60**, 475 - 484.

12. D. M. D'Alessandro, B. Smit and J. R. Long, *Angewandte Chemie International Edition*, 2010, **49**, 6058-6082.

13. A. Brunetti, F. Scura, G. Barbieri and E. Drioli, *Journal of Membrane Science*, 2010, **359**, 115-125.

14. A. B. Rao and E. S. Rubin, *Environmental Science & Technology*, 2002, **36**, 4467-4475.

15. B. P. America, 2005.

16. E. D. Bates, R. D. Mayton, I. Ntai and J. H. Davis, *Journal of the American Chemical Society*, 2002, **124**, 926-927.

17. C. Cadena, J. L. Anthony, J. K. Shah, T. I. Morrow, J. F. Brennecke and E. J. Maginn, *Journal of the American Chemical Society*, 2004, **126**, 5300-5308.

18. A. L. Kohl and F. C. Reisenfeld, 1985.

19. S. Wong and R. Bioletti.

20. M. M. Maroto-Valer, Z. Tang and Y. Zhang, *Fuel Processing Technology*, 2005, **86**, 1487-1502.

21. Z. Tang, M. M. Maroto-Valer and Y. Zhang, *Prepr. Pap.-Am. Chem. Soc., Div. Fuel Chem.*, 2004, **49**, 298-299.

22. http://www.mehtachemicals.com/.

23. C. Stewart and M.-A. Hessami, *Energy Conversion and Management*, 2005, **46**, 403-420.

24. H. Yang, Z. Xu, M. Fan, R. Gupta, R. B. Slimane, A. E. Bland and I. Wright, *Journal of Environmental Sciences*, 2008, **20**, 14-27.

25. X. Xu, C. Song, J. M. Andresen, B. G. Miller and A. W. Scaroni, *Energy & Fuels*, 2002, **16**, 1463-1469.

26. C. Song, *Catalysis Today*, 2006, **115**, 2-32.

27. K. T. Chue, J. N. Kim, Y. J. Yoo, S. H. Cho and R. T. Yang, *Industrial & Engineering Chemistry Research*, 1995, **34**, 591-598.

28. P. J. E. Harlick and A. Sayari, *Industrial & Engineering Chemistry Research*, 2006, **45**, 3248-3255.

29. http://www.co2crc.com.au/imagelibrary3/capture.php?screen=4.

30. G. S. Grasa and J. C. Abanades, *Industrial & Engineering Chemistry Research*, 2006, **45**, 8846-8851.

31. J. C. Abanades, E. S. Rubin and E. J. Anthony, *Industrial & Engineering Chemistry Research*, 2004, **43**, 3462-3466.

32. T. Shimizu, T. Hirama, H. Hosoda, K. Kitano, M. Inagaki and K. Tejima, *Chemical Engineering Research and Design*, 1999, **77**, 62-68.

33. J. C. Abanades, *Chemical Engineering Journal*, 2002, **90**, 303-306.

34. H. J. Ziock, E. J. Anthony, E. L. Brosha, F. H. Garzon, G. D. Guthrie, A. A. Johnson, A. Kramer, K. S. Lackner, F. Lau, R. Mukundan, T. W. Robison, B. J. Roop, J. D. Ruby, B. F. Smith and J. Wang, *Technical progress in the development of zero emission coal technologies*, 2002.

35. R. Banerjee, A. Phan, B. Wang, C. Knobler, H. Furukawa, M. O'Keeffe and O. M. Yaghi, *Science*, 2008, **319**, 939-943.

36. A. R. Millward and O. M. Yaghi, *Journal of the American Chemical Society*, 2005, **127**, 17998-17999.

37. D. Britt, H. Furukawa, B. Wang, T. G. Glover and O. M. Yaghi, *Proceeding of the National Academy of Sciences of the United States of America*, 2009, **106**, 20637-20640.

38. S. Couck, J. F. M. Denayer, G. V. Baron, T. Rémy, J. Gascon and F. Kapteijn, *Journal of the American Chemical Society*, 2009, **131**, 6326-6327.

39. G. Pannocchia, M. Puccini, M. Seggiani and S. Vitolo, *Industrial & Engineering Chemistry Research*, 2007, **46**, 6696-6706.

40. J.-i. Ida and Y. S. Lin, *Environmental Science & Technology*, 2003, **37**, 1999-2004.

41. C. Gauer and W. Heschel, *Journal of Materials Science*, 2006, **41**, 2405-2409.

42. J. C. Hicks, J. H. Drese, D. J. Fauth, M. L. Gray, G. Qi and C. W. Jones, *Journal of the American Chemical Society*, 2008, **130**, 2902-2903.

43. S. Alexander Stern, *Journal of Membrane Science*, 1994, **94**, 1-65.

44. J. Caro, M. Noack, P. Kölsch and R. Schäfer, *Microporous and Mesoporous Materials*, 2000, **38**, 3-24.

45. D. Shekhawat, D. R. Luebke and H. W. Pennline, 2003, **DOE/NETL-2003/1200**.

46. M. Anderson, *Dissertation for the Degree Doctor of Philosophy*, 2011.

47. M. A. Carreon, S. Li, J. L. Falconer and R. D. Noble, *Journal of the American Chemical Society*, 2008, **130**, 5412-5413.

48. M. E. Rivera-Ramos, *Ph. D Thesis*, 2009.

49. S. Himeno, T. Tomita, K. Suzuki, K. Nakayama, K. Yajima and S. Yoshida, *Industrial & Engineering Chemistry Research*, 2007, **46**, 6989-6997.

50. M. Hong, *Ph. D Thesis*, 2007.

51. H. Kita, K. Fuchida, T. Horita, H. Asamura and K. Okamoto, *Separation and Purification Technology*, 2001, **25**, 261-268.

52. N. Nishiyama, K. Ueyama and M. Matsukata, *Microporous Materials*, 1996, **7**, 299-308.

53. N. Nishiyama, K. Ueyama and M. Matsukata, in *Studies in Surface Science and Catalysis*, eds. S.-K. I. Hakze Chon and U. Young Sun, Elsevier, 1997, vol. Volume 105, pp. 2195-2202.

54. S. E. Veyo, L. A. Shockling, J. T. Dederer, J. E. Gillett and W. L. Lundberg, *ASME Journal of Engineering for Gas Turbines and Power*, 2002, **124**, 845-849.

55. K. Aoki, K. Kusakabe and S. Morooka, *Industrial & Engineering Chemistry Research*, 2000, **39**, 2245-2251.

56. T. Tomita, K. Nakayama and H. Sakai, *Microporous and Mesoporous Materials*, 2004, **68**, 71-75.

57. P. A. Barretta, T. Boixb, M. Puchec, D. H. Olsond, E. Jordane, H. Kollere and M. A. Camblor, *Chemical Communication*, 2003, **9**, 2114-2115.

58. K. Kusakabe, K. Ichiki, J.-i. Hayashi, H. Maeda and S. Morooka, *Journal of Membrane Science*, 1996, **115**, 65-75.

59. J. Shen, J. M. Kobe, Y. Chen and J. A. Dumesic, *Langmuir*, 1994, **10**, 3902-3908.

60. A. Corma, V. Fornés, R. M. Martín-Aranda and F. Rey, *Journal of Catalysis*, 1992, **134**, 58-65.

61. A. Vaccari, *Catalysis Today*, 1998, **41**, 53-71.

62. R. Quinn, J. B. Appleby and G. P. Pez, *Journal of Membrane Science*, 1995, **104**, 139-146.

63. C. E. Powell and G. G. Qiao, *Journal of Membrane Science*, 2006, **279**, 1-49.

64. J. G. Crespo and K. W. Boddekar, *Kluwer Academic Publishers, Dordrecht*, 1994, 316–342.

65. M. Teramoto, S. Kitada, N. Ohnishi, H. Matsuyama and N. Matsumiya, *Journal of Membrane Science*, 2004, **234**, 83-94.

66. M. Nakabayashi, K. Okabe, E. Fujisawa, Y. Hirayama, S. Kazama, N. Matsumiya, K. Takagi, H. Mano, K. Haraya and C. Kamizawa, *Energy Conversion and Management*, 1995, **36**, 419-422.

67. M. C. Trachtenberg, C. K. Tu, R. A. Landers, R. C. Wilson, M. L. McGregor, P. J. Laipis, D. N. Silverman, D. Thomas, R. L. Smith and F. B. Rudolph, *Life Support Biosph Sci.*, 1999, **6**, 293-302.

68. W. C. Yang and J. Ciferno, *DOE/NETL 401/072606*, 2006.

69. J. L. Wade, C. Lee, A. C. West and K. S. Lackner, *Journal of Membrane Science*, 2011, **369**, 20-29.

70. Z. Rui, M. Anderson, Y. S. Lin and Y. Li, *Journal of Membrane Science*, 2009, **345**, 110-118.

71. W. Zhu, C. Xia, D. Ding, X. Shi and G. Meng, *Materials Research Bulletin*, 2006, **41**, 2057-2064.

72. S. J. Chung, J. H. Park, D. Li, J. I. Ida, I. Kumakiri and J. Y. S. Lin, *Industrial & Engineering Chemistry Research*, 2005, **44**, 7999-8006.

73. K. Ishizaki, S. Komarneni and M. Nauko, *London, U. K.*, 1998.

74. M. Rajamathi, S. Thimmaiah, P. E. D. Morgan and R. Seshadri, *Journal of Materials Chemistry*, 2001, **11**, 2489-2492.

75. K. S. W. Sing, D. H. Everett, R. A. W. Haul, L. Moscou, R. A. Pierotti, J. Rouquerol and T. Siemieniewska, *Pure Appl. Chem.*, 1985, **57**, 603-619.

76. A. R. Studart, U. T. Gonzenbach, E. Tervoort and L. J. Gauckler, *Journal of the American Ceramic Society*, 2006, **89**, 1771-1789.

77. L. Zhang, X. Li, S. Wang, K. G. Romito and K. Huang, *Electrochemistry Communications*, 2011, **13**, 554-557.

78. M. D. M. Innocentini, P. Sepulveda, V. R. Salvini, V. C. Pandolfelli and J. R. Coury, *Journal of the American Ceramic Society*, 1998, **81**, 3349-3352.

79. P. Sepulveda, *American Ceramic Society Bulletin*, 1997, **76**, 61-65.

80. A. Imhof and D. J. Pine, *Advanced Materials*, 1999, **11**, 311-314.

81. C. Jiang, J. Ma, X. Liu and G. Meng, *Journal of Power Sources*, 2007, **165**, 134-137.

82. M.-Y. Cheng, D.-H. Hwang, H.-S. Sheu and B.-J. Hwang, *Journal of Power Sources*, 2008, **175**, 137-144.

83. X. Fang, G. Zhu, C. Xia, X. Liu and G. Meng, *Solid State Ionics*, 2004, **168**, 31-36.

84. X. Li, G. L. Xiao and K. Huang, *Journal of the Electrochemical Society*, 2011, **158**, B225-B232.

85. B. Zhu, *Journal of Power Sources*, 2001, **93**, 82-86.

86. B. Zhu, X. Liu, P. Zhou, X. Yang, Z. Zhu and W. Zhu, *Fuel Cells Bulletin*, 2002, **2002**, 8-12.

87. M. Anderson and Y. S. Lin, *Journal of Membrane Science*, 2010, **357**, 122-129.

88. J. J. Lombardo, R. Ristau, W. H. Harris and W. K. S. Chiu, *Journal of Synchrotron Radiation*, *submitted*, 2011.

89. K. N. Grew, Y. S. Chu, J. Yi, A. A. Peracchio, J. R. Izzo, F. Y. Hwu, F. D. Carlo and W. K. S. Chiu, *The Electrochemical Society*, 2010, **157**, B783-B792.

90. T. Fukui, K. Murata, S. Ohara, H. Abe, M. Naito and K. Nogi, *Journal of Power Sources*, 2004, **125**, 17-21.

91. H. Mori, C.-J. Wen, J. Otomo, K. Eguchi and H. Takahashi, *Applied Catalysis A: General*, 2003, **245**, 79-85.

92. Y. Wu, Y. He, T. Wu, T. Chen, W. Weng and H. Wan, *Materials Letters*, 2007, **61**, 3174-3178.

93. C. Xia and M. Liu, *Solid State Ionics*, 2002, **152–153**, 423-430.

94. B. Zhu, X. R. Liu, P. Zhou, X. T. Yang, Z. G. Zhu and W. Zhu, *Electrochemistry Communications*, 2011, **3**.

95. C. M. Lapa, F. M. L. Figueiredo, D. P. F. de Souza, L. Song, B. Zhu and F. M. B. Marques, *International Journal of Hydrogen Energy*, 2010, **35**, 2953-2957.

96. L. Zhang, R. Lan, X. Xu, S. Tao, Y. Jiang and A. Kraft, *Journal of Power Sources*, 2009, **194**, 967-971.

97. J. Di, M. Chen, C. Wang, J. Zheng, L. Fan and B. Zhu, *Journal of Power Sources*, 2010, **195**, 4695-4699.

98. T. Mori, Y. Wang, J. Drennan, G. Auchterlonie, J.-G. Li and T. Ikegami, *Solid State Ionics*, 2004, **175**, 641-649.

99. N. Xu, X. Li, M. A. Franks, H. Zhao and K. Huang, *Journal of Membrane Science*, 2012, **401–402**, 190-194.

100. P. Claes, B. Thirion and J. Glibert, *Electrochim Acta*, 1996, **41**, 141-146.

101. P. M. Claes, D.; Peeters, D. , *Eur. J. Inorg. Chem.*, 1999, **4**, 583-588.

102. P. M. Claes, D.; Peeters, D. , *Eur. J. Inorg. Chem.*, 1999, **4**, 589-592.

103. K. P. S. Zeller, P.; Haiss, P. , 2005, **2005**, 168-172.

104. S. Kohara, N. Koura, Y. Idemoto, S. Takahashi, M. L. Saboungi and L. A. Curtiss, *J Phys Chem Solids*, 1998, **59**, 1477-1485.

105. R. L. Frost, A. Soisnard, N. Voyer, S. J. Palmer and W. N. Martens, *J Raman Spectrosc*, 2009, **40**, 645-649.

106. N. P. Wen and M. H. Brooker, *J Phys Chem-Us*, 1995, **99**, 359-368.

107. M. E. Bottcher, P. L. Gehlken, H. Skogby and C. Reutel, *Mineral Mag*, 1997, **61**, 249-256.